

AD-A244 905



2

DTIC  
ELECTE  
JAN 08 1992  
S D D

NON-EQUILIBRIUM RADIATION FROM SHOCK-HEATED AIR

FINAL REPORT

W. H. Wurster, C. E. Treanor and M. J. Williams

July 1991

U.S. Army Research Office

Contract No. DAAL03-88-K-0174

CALSPAN-UB RESEARCH CENTER  
BUFFALO, NEW YORK

Approved for Public Release;  
Distribution Unlimited

92 1 7 059



92-00426

PERSONNEL SUPPORTED:

W. H. Wurster  
C. E. Treanor  
M. J. Williams  
J. R. Ambrusko  
J. Johnson

THE VIEW, OPINIONS, AND/OR FINDINGS CONTAINED IN THIS REPORT  
ARE THOSE OF THE AUTHOR(S) AND SHOULD NOT BE CONSTRUED AS  
AN OFFICIAL DEPARTMENT OF THE ARMY POSITION, POLICY, OR  
DECISION, UNLESS SO DESIGNATED BY OTHER DOCUMENTATION.

## TABLE OF CONTENTS

<u>Description</u>	<u>Page</u>
<b>PROGRAM SUMMARY</b>	<b>1</b>
<b>1.0 INTRODUCTION</b>	<b>3</b>
<b>2.0 EXPERIMENTAL CONSIDERATIONS</b>	<b>4</b>
2.1 Search for Additional Observables	4
2.2 Infrared Measurements	5
<b>3.0 ANALYTICAL AND MODELLING CONSIDERATIONS</b>	<b>6</b>
3.1 Equilibrium Radiation of NO and O <sub>2</sub>	6
3.2 Separation of Nonequilibrium O <sub>2</sub> and NO Radiation	9
3.3 Analysis of Nonequilibrium IR Measurements	10
3.4 Excitation Equations for the A <sup>3</sup> Σ State of NO	14
3.5 Rate Constants for Electronic Excitation	20
<b>REFERENCES</b>	
<b>FIGURES</b>	
<b>APPENDICES</b>	
A AIAA-89-1918, Nonequilibrium UV Radiation and Kinetics Behind Shock Waves in Air	A-1
B AIAA-90-1666, Kinetics of UV Production Behind Shock Waves in Air	B-1
C Full-scale Records of Data in Figure 7	C-1
D IR Spectral Analysis	D-1
E Full-scale Records of Data in Figure 4	E-1

## LIST OF FIGURES

<u>Figure</u>	<u>Page</u>
1 Major Elements of the IR Radiometer - Shock Tube System	25
2 Data Trace of IR Radiometer	26
3 Measured Wavelength Response of the Radiometer	27
4 Intensity Calibration of the Radiometer	28
5 Radiation Measurements, $2\overset{6}{3}0$ nm	29
6 Radiation Measurements, $2\overset{3}{6}0$ nm	30
7 Infrared Radiation Matrix, Experiment and Calculation	31
8 Three Temporal Parameters Characterizing Non-equilibrium Infrared Radiation	32
9 Infrared Incubation Time, Experiment and Calculation	33
10 Infrared Time-To-Half-Peak, Experiment and Calculation	34
11 Infrared Time-To-Peak, Experiment and Calculation	35
12 Infrared Ratio of Peak to Equilibrium Radiation, Experiment and Calculation	36
13 Infrared Radiation Matrix, Experiment and Adjusted Calculation	37
14 Ultraviolet Run Matrix, Experiment and Calculation	38

REPORT DOCUMENTATION PAGE			Form Approved OMB No 0704-0188	
<small>Public reporting burden for this collection of information is estimated to average 1 hour per response, including the time for reviewing instructions, searching existing data sources, gathering and maintaining the data needed, and completing and reviewing the collection of information. Send comments regarding this burden estimate or any other aspect of this collection of information, including suggestions for reducing this burden, to Washington Headquarters Services, Directorate for Information Operations and Reports, 1215 Jefferson Davis Highway, Suite 1204 Arlington, VA 22202-4302, and to the Office of Management and Budget, Paperwork Reduction Project (0704-0188), Washington, DC 20503.</small>				
1. AGENCY USE ONLY (Leave blank)	2. REPORT DATE July 1991	3. REPORT TYPE AND DATES COVERED Final, Jul 88-30 Jun 91		
4. TITLE AND SUBTITLE Non-equilibrium Radiation From Shock-Heated Air		5. FUNDING NUMBERS DAAC 03-88-K-0174		
6. AUTHOR(S) W.H. Wurster, C.E. Treanor and M.J. Williams				
7. PERFORMING ORGANIZATION NAME(S) AND ADDRESS(ES) Calspan-UB Research Center 4455 Genesee Street Buffalo, NY 14225		8. PERFORMING ORGANIZATION REPORT NUMBER		
9. SPONSORING MONITORING AGENCY NAME(S) AND ADDRESS(ES) U. S. Army Research Office P. O. Box 12211 Research Triangle Park, NC 27709-2211		10. SPONSORING MONITORING AGENCY REPORT NUMBER ARO 26244.3-E6-SDI		
11. SUPPLEMENTARY NOTES The view, opinions and/or findings contained in this report are those of the author(s) and should not be construed as an official Department of the Army position, policy, or decision, unless so designated by other documentation.				
12a. DISTRIBUTION AVAILABILITY STATEMENT  Approved for public release; distribution unlimited.		12b. DISTRIBUTION CODE		
13. ABSTRACT (Maximum 200 words)  A research program is described whose objectives include the quantitative measurement of the ultraviolet radiation behind strong shock waves in air, the identification of the radiating species and the determination of the mechanisms and rates that govern the emission. A shock tube was used to generate 3-4 km/s shock waves through air and O <sub>2</sub> -N <sub>2</sub> mixtures at initial pressures between 0.36-2.25 torr. The temporal gas-radiance profiles recorded radiometrically exhibited strong non-equilibrium overshoots, followed by decay to steady-state equilibrium. The dependence of the peak overshoot values on wave speed and pressure was measured and shown to scale with density. Emission spectra of the gas both in the overshoot region and the equilibrium region showed the NO gamma band system between 210 and 340 nm to be the dominant radiation source. The role of O <sub>2</sub> Schumann-Runge radiation in this region was also studied; in pure O <sub>2</sub> no overshoot was recorded. Infrared vibronic emission profiles were also measured and shown to be a description of the NO concentration growth. It was found that currently accepted rates for air ground-state chemistry do not predict the NO generation correctly. Finally, a simplified				
14. SUBJECT TERMS excitation model is suggested to describe the ultraviolet radiation behind the shock wave.  Air Radiation Ultraviolet Air Kinetics Nonequilibrium Radiation		15. NUMBER OF PAGES 38		
17. SECURITY CLASSIFICATION OF REPORT UNCLASSIFIED		18. SECURITY CLASSIFICATION OF THIS PAGE UNCLASSIFIED		16. PRICE CODE
19. SECURITY CLASSIFICATION OF ABSTRACT UNCLASSIFIED		20. LIMITATION OF ABSTRACT UL		

## PROGRAM SUMMARY

This report presents the results of a research program designed to investigate the generation of ultraviolet radiation arising from the non-equilibrium thermodynamic conditions behind strong shock waves in air. Such conditions can arise behind the bow shock of vehicles in rapid ascent through the atmosphere. The overall objective of this experimental and analytical program was to support the development of a capability to predict reliably the non-equilibrium ultraviolet radiation from such flowfields.

Specifically, the program objectives included:

- an early assessment of the radiation to identify the radiating species and to establish its dependence on velocity and altitude. These data were to support instrument design issues for a proposed sounding rocket flight to study these boost-phase signatures.
- the development of a comprehensive base of quantitative spectral radiance data to support the development of predictive capabilities by the boost-phase signature community.
- the development of a model to describe the electronic state excitation kinetics that govern the nonequilibrium ultraviolet radiation from shock-heated air.

The experiments made use of a shock tube facility and spectro-radiometric instrumentation available at Calspan. The system was capable of producing shocked air conditions over the actual range of velocity and altitude of interest to the flight program. Both spectrometric and radiometric data were obtained as the shock waves swept past the viewing station in the shock tube. Species radiating in the ultraviolet as well as in the infrared were investigated in terms of spectral intensity and temporal behavior. Additionally, shocks in various nitrogen/oxygen mixtures were used to provide a broad matrix of data to support the chemical and electronic state kinetics developments.

Following is a listing of the principal results that have accrued.

1. Highly resolved spectra of the nonequilibrium UV radiation between 200 - 400 nm have shown the NO Gamma-band radiation to dominate over a smaller contribution from the O<sub>2</sub> Schumann-Runge system.

Dist	
A-1	

2. The dependence of this nonequilibrium UV radiation on flight vehicle velocity and altitude was established by direct measurements in the laboratory. These data were successfully applied to subsequent flight instrument settings.
3. Spectra obtained from tests using pure O<sub>2</sub> permitted the contribution of O<sub>2</sub> to the air spectrum to be quantitatively determined.
4. Similarly, the temporal profiles in pure O<sub>2</sub> recorded by the radiometers were used to obtain, by subtraction, the kinetic behavior of the dominant NO-Gamma band radiation behind the shock waves.
5. An extensive data base of UV nonequilibrium spectral radiance profiles has been generated for use by the signature modelling community in this area. Parameters in this data base include shock velocity, pre-shock pressure (altitude) and test gas composition: air, pure O<sub>2</sub> and various O<sub>2</sub>-N<sub>2</sub> mixtures.
6. A supporting infrared data set has been obtained, which provides temporal profiles of the global NO formation kinetics behind shock waves in air and O<sub>2</sub>-N<sub>2</sub> mixtures.
7. It is concluded that the currently accepted rates for air ground-state chemistry do not predict the NO generation correctly.
8. A simplified excitation model is suggested to describe the ultraviolet radiation behind the shock wave.

## 1.0 INTRODUCTION

The motivation for this program centered on the development of capability for predicting the ultraviolet radiation from the bow shock of a vehicle ascending between 40-60 km at velocities between 3-4 km/s. The objectives of the program included providing quantitative measurements in support of a sounding rocket flight experiment: the identification of the radiating species, and the dependence of the radiation on altitude and velocity. In addition, basic spectral radiance data were acquired in support of modelling this nonequilibrium radiation.

The non-equilibrium aspect of the radiative signature arises from the fact that at higher altitudes the decreased density and collision frequency of molecules behind the shock front slows both the chemical reactions that establish species concentrations and those that govern equipartition among internal energy states: electronic, vibrational and rotational. Thus, under some conditions there exist strong gradients behind the shock front, consisting of species concentrations and excited state populations far from equilibrium with the local (and changing) translational temperature. To describe this nonequilibrium and to predict its dependence on velocity and altitude requires that the relevant kinetic rates and mechanisms be known. Thus, a major goal was to provide a model to describe the electronic state kinetics that govern the nonequilibrium ultraviolet radiation from shock-heated air.

The experimental aspects of the program centered upon the use of a shock tube and associated spectrometric and radiometric instrumentation, whereby radiative signatures from shock heated air,  $O_2$  and  $N_2-O_2$  mixtures were recorded. The flight conditions of interest, namely, shock velocities of 3-4 km/s at altitudes above 40 km (2.25 torr) can be exactly duplicated in a shock tube. Thus, the measurement of the radiation profile as the shock-heated air passes a given station can be readily and simultaneously achieved for a number of wavelengths and with different instruments. This procedure was the basis for the measurements conducted under this program.

The results of the first two years' work are embodied in two AIAA papers, Refs. 1 and 2, which, for completeness, are included in their entirety as Appendices A and B. The shock tube facility, instrumentation, calibration, typical data and their description and analyses are all presented in these papers.

The body of this report addresses principally the efforts of the subsequent work. These included the search for additional diagnostic observables and the resultant infrared measurements



of the 5.3  $\mu\text{m}$  NO fundamental vibronic radiance profiles. Finally, an extensive discussion of the gasdynamic and electronic state kinetic modelling and analyses is presented.

## 2.0 EXPERIMENTAL CONSIDERATIONS

### 2.1 Search for Additional Observables

As will be addressed further in later sections, a major effort was undertaken to formulate a model to describe the kinetics of the population of the electronically excited NO(A) state. This state gives rise to the Gamma band system which dominates the nonequilibrium UV radiation from shock-heated air. Because the model contains a number of coupled reactions and interacting species, a search was undertaken to determine whether any other relevant species gave rise to observables that could be used for additional kinetic diagnostics. Two were identified: atomic oxygen and the electronically excited  $\text{N}_2(\text{A})$  state. Each of these plays a key role in the nonequilibrium radiation overshoot kinetics; serious effort was expended to evaluate their potential as experimental observables.

The technique of atomic oxygen absorption near 130 nm in the vacuum ultraviolet is actively being used in shock tube kinetic studies, as reported in the 1989 Shock Tube Symposium. Details of this technique, especially those of the absorption lamp source were obtained and found to be tractable. However, final calculations showed that the concentration of O-atoms in the present experiments was much too high for these absorption measurements. Atomic O absorption would correspond to an optically thick gas, which precluded its use as a kinetic diagnostic, and resulted in abandoning this effort.

The use of laser-induced fluorescence techniques to obtain instantaneous concentrations of the excited  $\text{N}_2(\text{A})$  state behind shock waves was also considered. The experimental plan would be to absorb the laser beam by transitions from the A to B state and to observe subsequent fluorescent emission to other vibrational A states. These bands are in the  $\text{N}_2$  First-Positive  $\text{B}^3\pi - \text{A}^3\Sigma$  system, between 600 - 800 nm.

This design effort involved a detailed study of the available energy levels of these states, the transitions in various wavelength regions and the resultant line densities per wavelength interval. Overlap integrals were taken into account to optimize fluorescent signals while

minimizing laser power requirements. The use of excimer and YAG-pumped dye lasers was evaluated, as either could be procured for the term of the experiments.

The results of these analyses showed that this measurement was both high risk and costly, and that its implementation could adversely affect the balance of this program. Several factors ruled against this measurement. A major one was that the temperature of the gas during the region of interest was high ( $> 4000$  °K), resulting in a significant thermal Boltzmann population of both B- and A-state levels. Further, because they are separated by only 1.2 eV ( $B = 7.4$  eV,  $A = 6.2$  eV), their populations are not much different, typically  $10^7$  vs  $10^9$  per cc. Thus, when attempting to measure the fluorescent component over a manifold of transitions, the inability to differentiate against spontaneous, thermal transitions becomes prohibitive. Efforts on this task were terminated, and further diagnostic efforts were directed toward the improved infrared measurements described below.

## 2.2 Infrared Measurements of NO

From concurrent analyses it became apparent that the kinetics of the formation of NO behind the shock played a critical role in the overall scheme for the excitation of the electronic NO(A) state. Earlier in the program,<sup>2</sup> preliminary measurements of the vibronic bands of NO at  $5.3$   $\mu\text{m}$  had shown that this system could be used to monitor global (ground state) NO kinetics. These early profiles were measured with a standard IR radiometer comprising a HgCdTe detector, bandpass filter and slits for FOV definition. Figure 11, page B-9 depicts several such profiles, and illustrates the complication of a "foot" of signal preceding the arrival of the shock wave at the observation port FOV.

This foot generally arises from scattered light from the highly luminous shock front, as it approaches the measurement station. Scattering can occur from any defect (scratch, chip, film) on either of the shock tube windows, or from any slits, baffles or radiometer tube walls that are illuminated by the shocked gas front and which are "seen" by the detector. Even second reflections can give rise to the scattered component. It should also be noted that after the shock passes through the FOV, any candidate scattering site or surface is doubly illuminated, giving rise to a larger scattered signal component, but which is now buried in the true signal. The correction would be at least equal to twice that of the foot seen when the shocked gas is not in the FOV.

A new radiometer was designed to surmount these difficulties. A schematic diagram of the optics is shown in Figure 1. A major feature is that the entire radiometer is separated from the shock tube. The physical apertures that define the very precise FOV are each imaged onto the shock tube windows by a  $\text{CaF}_2$  lens. One stop is the detector chip itself, and the second is a slit made of razor blades, well removed from illumination by the advancing shock wave. It is sized and positioned so that its image on the lower window is appropriate for the desired FOV. In this way there are no physical sites from which scattering can occur. The windows were removed after each test to preclude scratching while the tube was being scrubbed. Implementing these features resulted in a dramatic reduction in scattered radiation, as evidenced by the lack of the pre-shock "foot" in the temporal radiance profiles. Figure 2 illustrates the improvement.

An InSb detector was used in the new radiometer. It was found that even though the long wave roll-off of the detector response clips one wing of the NO band, the higher detectivity results in a net gain in SNR. The combined filter-detector bandpass function, between 5 - 5.5  $\mu\text{m}$  was determined by separate bench experiments. A standard blackbody source through a scanning monochromator was calibrated and then used to establish the wavelength dependence of the radiometer, as shown in Figure 3.

System calibration was achieved by means of a chopped, standard blackbody which completely filled the FOV and whose intensity spanned the range of those for the test gases. Figure 4 presents a plot of the blackbody radiance convolved with the filter function and the detector response function ( $\int I_{\text{BB}} F_{\lambda} D_{\lambda} d\lambda$ ,  $\text{wcm}^{-2}\text{sr}$ ) against the recorded signal levels in millivolts. System linearity is evident, and these data were used to obtain an overall calibration constant that was applied to all subsequent profile measurements. By these means the in-band radiance from the NO (formed and heated behind the shock wave) can be directly related to that from a blackbody of known temperature. The analysis of these data and their application to the kinetic modelling are discussed in a later section.

### 3.0 ANALYTICAL AND MODELLING CONSIDERATIONS

#### 3.1 Equilibrium Radiation of NO and O<sub>2</sub>

The time-dependent measurements of the ultraviolet radiation, as described in Appendix A page 3, can be used to obtain an equilibrium radiation value at long times. These can then be compared with previous equilibrium experiments and calculations by reducing the results to an

evaluation of the electronic transition moments for the NO Gamma and O<sub>2</sub> Schumann-Runge systems.

To accomplish this, the radiation from a single spectral vibrational band of an electronic band system is written as

$$R_{v'v''} = n P_u \frac{16\pi^3 c e^2 a_0^2 10^{-7}}{3} \omega^4 \frac{\sum |R_e|^2}{d_u} \frac{e^{-E_{v'}/kT}}{Q_{v'}} g_{v'v''} \left( \frac{W}{\text{cm}^3 \text{sr}} \right) \quad (1)$$

where  $\frac{16\pi^3 c e^2 a_0^2 10^{-7}}{3} = 3.20 \times 10^{-30} \text{ W cm}^4/\text{sr}$

- $n$  = number density of molecules ( $\text{cm}^{-3}$ )
- $P_u$  = fraction of molecules in upper electronic state
- $\omega$  = wavenumber of radiation ( $\text{cm}^{-1}$ )
- $\sum |R_e|^2$  = sum of squared dipole moments for transitions from degenerate upper states, atomic units
- $d_u$  = degeneracy of upper state
- $E_{v'}$  = vibrational energy of upper state
- $Q_{v'}$  = vibrational partition function of upper state

By representing each vibrational transition ( $v' \rightarrow v''$ ) as a simple Q branch, and assuming that  $|R_e|^2$  can be taken as a constant, the spectral radiance can be approximated as

$$I_{v'v''}(\omega) = R_{v'v''} \left| \frac{B_e''}{B_e'' - B_e'} \right| \frac{1}{kT} e^{-\left( \frac{B_e''}{B_e'' - B_e'} \right) \left( \frac{\omega - \omega_{v'v''}}{kT} \right)} \frac{W}{\text{cm}^3 \text{sr cm}^{-1}} \quad (2)$$

for  $\omega > \omega_{v'v''}$

$= 0 \text{ for } \omega < \omega_{v'v''}$

where

- $B_e', B_e''$  = rotational constants for upper and lower states
- $\omega_{v'v''}$  = bandhead wavenumber for  $v', v''$  transition

If  $B_e' > B_e''$ , the equation applies for  $\omega < \omega_{v'v''}$ , and  $I_{v'v''} = 0$  for  $\omega > \omega_{v'v''}$ . The dependence of B on v is not included in the approximation. The total spectral radiance is then

$$I(\omega) = \sum_{v'v''} I_{v'v''}(\omega) \quad (3)$$

The spectral radiance calculated with this approximation is shown in Appendix A, Figures 12 and 13 for the NO Gamma and O<sub>2</sub> Schumann-Runge systems.

The in-band radiation that should be measured by the calibrated detector for a single band system is then

$$S = \ell \int_0^{\infty} I(\omega) F(\omega) D(\omega) d\omega \quad \frac{W}{cm^2 sr} \quad (4)$$

where  $\ell$  is the diameter of the shock tube,  $F(\omega)$  is the filter transmission function and  $D(\omega)$  is the detector response function.  $F(\omega)$  for the 230 and 260 nm filters is shown in Figure 5 of Appendix B. The detector that was used for the broad 230 nm filter has maximum sensitivity at 205 nm. The sensitivity decreases by 20% at 185 nm and at 250 nm. At longer wavelengths the sensitivity drops exponentially, decreasing by a factor of 10 at 300 nm. The sensitivity of the detector that was used for the narrow-band 260 nm measurements was taken as constant over the band-pass.

The integrals in Equation (4) were calculated as functions of temperature for the NO Gamma and O<sub>2</sub> Schumann-Runge systems. The absolute calibration was obtained by calculating similar integrals for a black-body source of radiation and following the calibration procedure described in Section 2.2.

This results in calculated functions of temperature,  $M_{NO}$  and  $M_{O_2}$ , where these are related to  $S_{NO}$  and  $S_{O_2}$  by

$$S_{NO} = M_{NO} \ell n_{NO} |Re|_{NO}^2, \quad S_{O_2} = M_{O_2} \ell n_{O_2} |Re|_{O_2}^2 \quad (5)$$

From Equations (4) and (5) it follows that the in-band radiation to be expected from the gas mixture would be

$$S_{MIX} = S_{NO} + S_{O_2} = n_{NO} |R_e|_{NO}^2 \ell M_{NO} + n_{O_2} |R_e|_{O_2}^2 \ell M_{O_2} \quad (6)$$

or

$$\frac{S_{MIX}}{n_{O_2} M_{O_2} \ell} = |R_e|_{O_2}^2 + |R_e|_{NO}^2 \left( \frac{M_{NO}}{M_{O_2}} \cdot \frac{n_{NO}}{n_{O_2}} \right) \quad (7)$$

Since  $M_{NO}$  and  $M_{O_2}$  are known from the calculation, and  $n_{NO}$  and  $n_{O_2}$  are known from the equilibrium shock calculation, the experimental value of  $S_{MIX}$  divided by  $n_{O_2} M_{O_2} \ell$  can be plotted vs  $(M_{NO} n_{NO} / M_{O_2} n_{O_2})$ . The intercept and slope of the straight line yield the  $|R_e|^2$  for  $O_2$  and  $NO$ . These plots are shown in Figures 5 and 6 for the 230 nm and 260 nm results for  $O_2$  and  $NO$ . Measured vs calculated values of the equilibrium in-band radiance for 230 and 260 nm are plotted in Figures 7 and 8 of Appendix B, using the derived values of  $|R_e|^2$ . (The notation of Appendix B is slightly different from that used here.)

### 3.2 Separation of Nonequilibrium $O_2$ and $NO$ radiation

The equilibrium ultraviolet radiation from the shock tube is a well understood mixture of  $O_2$  Schumann-Runge radiation and  $NO$  Gamma radiation, as discussed in Section 3.1. The 5%  $O_2$  experiments produce practically no  $O_2$  radiation, the 22%  $O_2$  tests provide about equal amounts of  $NO$  and  $O_2$  contributions, and the 40%  $O_2$  tests provide appreciably more Schumann-Runge than Gamma contributions. In the nonequilibrium region, the  $NO$  radiation is the dominant contributor in almost all cases. However, it is necessary to make some correction to the total radiation measurements for the  $O_2$  content in order to obtain the  $NO$  overshoot history.

Experiments with 100% oxygen show that the  $O_2$  radiation does not overshoot its equilibrium value, but rises smoothly to a final plateau (see Figure 5 Appendix A). This feature was observed in work at AVCO<sup>3</sup> in the late 1950's, and attributed to the rapid predissociation of the

oxygen excited B state. Thus the B state remains in local thermodynamic equilibrium with the oxygen atom population, so that the number of O<sub>2</sub> molecules/cm<sup>3</sup> in the B state is given by

$$n_{O_2(B)} = \frac{1}{K} \left( \frac{n_{O_2(B)}}{n_{O_2}} \right)_{LTE} n_o^2$$

$$= \frac{n_o^2}{K} \left\{ 1.765 e^{-11,019/T} \left( \frac{1 - e^{-2293/T}}{1 - e^{-990/T}} \right) \left( 1.465 - 1.4 \times 10^{-4} T \right) \right\} \quad (8)$$

where K is the equilibrium constant for the reaction and the last factor in the equation is an approximate representation (appropriate over the range 3000 to 7000 K) of the required correction<sup>4</sup> to the rigid-rotator simple-harmonic-oscillator model. The O<sub>2</sub> radiation is taken to be proportional to n<sub>O<sub>2</sub>(B)</sub>, as determined from the equilibrium measurements.

We have assumed that the O<sub>2</sub> S-R system follows the same behavior in the radiation from N<sub>2</sub>/O<sub>2</sub> mixtures, with the O<sub>2</sub>(B) state staying in local equilibrium with the oxygen atom concentration at the translational temperature. The oxygen atom concentration behind the shock was calculated from a normal-shock nonequilibrium code<sup>5</sup>, and this population was used to determine the B state participation in the observed radiation. This amount of radiation was subtracted from the total observed, and the remainder was attributed to the NO Gamma system.

The results of this subtraction are shown in Figure 6 of Appendix B for a matrix of nine runs. The total radiation and the portion attributed to NO Gamma are shown. In the 5% O<sub>2</sub> experiments the corrections are negligible, and for the 22.3% O<sub>2</sub> tests the corrections are very small in the nonequilibrium region, except at the slowest shock velocities. For the 40% cases at low velocities there is an appreciable correction.

### 3.3 Analysis of Nonequilibrium Infrared Measurements

The nitric oxide 5.3 um radiation intensity is expected to be proportional to the NO concentration and a relatively weak function of the temperature\*. Thus the measurement of this radiation can be used to determine the time-history of the NO concentration behind the shock wave. This time-history of the ground-state chemistry behind the shock wave is a critical input to any calculation of the anticipated time history of the ultra-violet radiation. The infra-red measurements obtained during the first phase of this program demonstrated the ability to determine NO

\* The NO is optically thin, and it is shown in Reference 3 that NO vibrational relaxation does not appreciably affect the interpretation of the measured NO-IR radiation. The temperature dependence is given in Appendix D.

concentration, but did not contain enough resolution to resolve this time history. In the second phase of the program the sensitivity of the infrared detection system was improved to give a better measure of this ground-state NO chemistry, to use as a guide in interpretation of the ultraviolet data.

A very general picture of the observed infra-red radiation is given in Figure 7 showing plots of observed intensity vs lab time behind the shock. (Full-page copies of these graphs are given in Appendix C). The three columns correspond to the three O<sub>2</sub>/N<sub>2</sub> mixture ratios that were investigated, and the results are arranged vertically according to velocity. The time histories show a rise to maximum, an approach to equilibrium, and the disturbance caused by arrival of the hydrogen/oxygen interface, resulting in OH and H<sub>2</sub>O radiation.

The radiation level attained at equilibrium is proportional to the NO concentration and a weak function of the equilibrium temperature. Both the NO concentration and the temperature can be calculated if the ground-state chemical rates are known. It is shown in Appendix D that the temperature dependence that is expected for NO radiation measured with the filter-detector system that was used is:

$$f(T) = 3.51 \times 10^{12} [1 + 3.21 \times 10^{-4} (T - 3000)] \quad (9)$$

This temperature dependence can be confirmed by dividing the measured equilibrium intensities by  $f$  and plotting the results vs the NO concentrations. As shown in Figure 1 of Appendix D, this demonstrates the proper linear dependence on NO concentration, and provides a relation that can be used to interpret the nonequilibrium data.

Also shown in Figure 7 are calculations of the expected NO IR radiation. These calculated results were obtained by utilizing a 7-species, 10-reaction model in a normal-shock kinetics code<sup>4</sup> to determine the time history of the NO concentration and temperature behind the shock. These values were then used with Equation (12) of Appendix D to determine the radiation. The rates that were used in these calculations are those suggested by Wray<sup>6</sup>, as corrected by Camac et al<sup>7</sup>. The Camac corrections are the deletion of the reaction  $N_2 + O_2 \rightleftharpoons 2NO$ , and a decrease of a factor of 2.5 in the rate for  $N_2 + O \rightleftharpoons NO + N$ . The Camac rates are expressed as

$$k_i = A_i T^{B_i} e^{-C_i/T} \quad (10)$$



and are given in Table 1. These rates were considered to be the most relevant ones available for the density and shock-velocity range of interest in the present experiments.\*

$$k_f = AT^B e^{-C/T} \text{ cm}^3/\text{molecule-sec or cm}^6/\text{molecule-sec}$$

		A	B	C (°K)
1.	$O_2 + O \rightarrow 2O + O$	$1.5 \times 10^{-4}$	-1.0	59,380
2.	$O_2 + O_2 \rightarrow 2O + O_2$	$5.4 \times 10^{-5}$	-1.0	"
3.	$O_2 + M \rightarrow 2O + M$	$1.2 \times 10^{-5}$	-1.0	"
4.	$N_2 + N \rightarrow 2N + N$	$6.8 \times 10^{-2}$	-1.5	113,200
5.	$N_2 + N_2 \rightarrow 2N + N_2$	$8.0 \times 10^{-7}$	-0.5	"
6.	$N_2 + M \rightarrow 2N + M$	$3.2 \times 10^{-7}$	-0.5	"
7.	$NO + M \rightarrow N + O + M$	$1.7 \times 10^{-3}$	-1.5	75,490
8.	$N + O_2 \rightarrow NO + O$	$2.2 \times 10^{-14}$	+1.0	3,565
9.	$O + N_2 \rightarrow NO + N$	$5 \times 10^{-11}$	0	38,016
10.	$NO^+ + e^- \rightarrow N + O$	$9.0 \times 10^{-3}$	-1.5	0

**TABLE 1. CAMAC RATES USED FOR GROUND-STATE CALCULATIONS**

\* A recent publication<sup>8</sup> gives an experimental result for  $k_3$  (with  $M=N_2$ ) of  $3.4 \times 10^{18} (\pm 25\%) T^{-1} \exp(-59,380/T)$ , measured from 2400 to 4100K. This is about half the Camac value. The most recent experiments with NO formation<sup>9</sup> suggest that  $k_9 = 1.8 \times 10^{14} \exp(-38,370)/T$ , about 6 times larger than Camac's value.

The general conclusion that can be drawn from comparison of calculations and experiments in Figure 7 is that although the calculated results show profiles similar to the experiments, they do not predict the magnitude or position of the overshoot correctly. The calculations fail most noticeably for low velocities and for the 40%/60%  $O_2/N_2$  mixture. Camac's results<sup>3</sup> showed similar problems, but those could not be resolved because of possible boundary-layer effects in his shock tube, which had a 1.5-inch diameter. In the present experiments, with a 3-inch diameter tube, boundary-layer effects do not contribute to determining the time scale behind the shock at the times involved. In addition, many of the calculations do not demonstrate a radiation maximum, whereas an experimental overshoot is clearly shown.

Because of the importance of the ground-state chemistry in explaining the measured ultraviolet radiation, some effort was made to adjust rates to provide better agreement with the infra-red experiments.

As pointed out by Camac et al<sup>7</sup>, the general features of the time history of the IR radiation can be characterized by the three temporal parameters shown in Figure 8. These are an incubation time, a time to half maximum, and a time to maximum. The experimental values for these parameters are plotted in Figures 9, 10, and 11. The ratio of peak-to-equilibrium radiation is shown in Figure 12. Each figure shows experimental curves for the three mixtures, as well as the values obtained from normal-shock calculations using the Camac rates. Calculated profiles for the 40%  $O_2/60\%$   $N_2$  mixture did not show maxima.

## INCUBATION TIME

The early formation of NO behind the shock is governed by reaction 9, which depends on oxygen atoms to produce the NO. (Reaction 9 also produces a nitrogen atom, which is immediately converted to another NO molecule leaving a replacement for the O atom, all through reaction 8.) Thus there is a delay in the NO production until O atoms are formed by reactions 2 and 3. These dissociation reactions are delayed<sup>10</sup> by vibration-dissociation coupling, an effect that is not included in the present calculations. Thus a complete description of the incubation time of NO formation requires an accurate description of the early process of oxygen-atom dissociation. The need for a longer incubation time led Camac to discount the  $N_2+O_2 \rightleftharpoons 2NO$  reaction, which would supply NO at very early times (he also had other experimental reasons for removing this reaction). However, it is clear that the Camac rates do not provide long enough incubation times at low velocities.

### TIME TO HALF-MAXIMUM

Apart from the relatively short incubation time, the time to half-maximum is governed by the rate of production of NO by reaction 9. It was on the basis of this measurement that Camac et al suggested a reduction of a factor of 2.5 in this rate\*. In their examples, they reduced the coefficient from Wray's value of  $7 \times 10^{13}$  to  $2.8 \times 10^{12}$ , as indicated in Table 1. This correction provides reasonable agreement, except for the low-speed shock waves; for these cases the Camac rates predict a longer time to half maximum than shown in the experiments, and do not predict an overshoot.

### TIME-TO-PEAK

Figures 11 and 12 describe the time-to-peak and the ratio of peak-to-equilibrium radiation. The Camac rates do not provide results consistent with the experiments for either parameter. In many cases the calculated intensities do not show a maximum, as is evident in Figure 7.

By changing the reaction rates we have obtained calculations in reasonable agreement with the experimental results, but only by changes that are inconsistent with known values of these rates. For example, by changing rates of  $k_1$ ,  $k_2$ ,  $k_3$ , and  $k_9$ , the results shown in Figure 13 can be obtained. These calculations still do not provide an accurate fit to all of the data, and require use of rates that are in complete disagreement with accepted rates. However, we have used these calculations in Section 3.5 to make comparisons with ultraviolet radiation because of their close match to the infrared results.

The possible changes in rates that would provide results consistent with all of the data have not been pursued further in the present work. Instead, the infrared data have been used as a guideline in interpreting agreement of theory and experiment in the ultraviolet measurements.

### 3.4 Excitation Equations for the $A^3\Sigma^+$ State of NO

The mechanism by which the NO(A) state is excited behind the shock wave is not known, but it is certain to involve a complex set of competing reactions. In particular, energy transfer from

---

\* Camac et al arrived at the conclusion, based on a first-order analysis, that the same effect could also be accomplished by decreasing the rate of reactions 2&3 by a factor of 2.5, which would decrease the supply of oxygen atoms. This, they argued, would decrease the NO production rate. Although this is true at the very earliest times, we have found that decreasing the O<sub>2</sub> dissociation rate increases the temperature at any given position behind the shock, and the net effect is an increase in the NO formation rate, which is very temperature sensitive.

the metastable  $N_2(A)$  state is usually considered as a parallel path for  $NO(A)$  excitation. A listing of the energies involved in relevant chemical states is shown in Table 2.

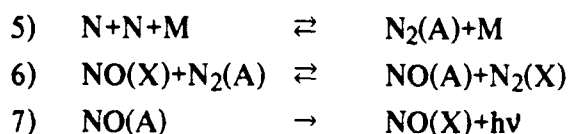
$N + N$	113,243 °K
$N + O$	86,321
$NO(A) + NO(X)$	74,375
$N_2(A)$	72,234
$NO(A)$	63,259
$O + O$	59,400
$N$	56,621
$O$	29,700
$NO + NO$	22,232
$NO$	11,116
$N_2$	0
$O_2$	0

TABLE 2. ENERGIES ASSOCIATED WITH CHEMICAL SPECIES

Mechanisms for the high-temperature excitation of the  $NO(A)$  state have been examined in References 11 and 12. The simplest mechanisms suggested are direct excitation by electron collision or atom collision, recombination of  $N$  and  $O$  to form  $NO(A)$ , and recombination of two  $N$  atoms to form  $N_2(A)$ . The near-resonant exchange between  $NO(A)$  and  $N_2(A)$  is usually assumed to occur very rapidly compared with other reactions.

A representative set of reactions is:

- 1)  $NO + e \rightleftharpoons NO(A) + e$
- 2)  $N + O + M \rightleftharpoons NO(A) + M$
- 3)  $N_2 + e \rightleftharpoons N_2(A) + e$
- 4)  $N_2 + N \rightleftharpoons N_2(A) + N$



Reaction 7, the spontaneous emission of radiation from the NO(A) state is the signal that is observed. The radiative lifetime of this state is known to be 0.2  $\mu\text{s}$ , so that  $k_{7f} = 5 \times 10^6 \text{sec}^{-1}$ . The reaction is written in a single direction because the radiating gas is optically thin. Reactions 2 and 5 are written as three-body reactions, but two-body reactions could also contribute. In the nonequilibrium region these reactions proceed in the reverse direction, as quenching reactions. It should be emphasized that a great many other paths of excitation are possible, many including intermediate states.

The rate of increase of the number density of NO(A) and N<sub>2</sub>(A) molecules can be written for this set of reactions as

$$\begin{aligned}
\frac{dn_{\text{NOA}}}{dt} = & k_{1f} n_{\text{NO}} n_e - k_{1r} n_{\text{NOA}} n_e + k_{2f} n_{\text{N}} n_o n_{\text{M}} - k_{2r} n_{\text{NOA}} n_{\text{M}} \\
& + k_{6f} n_{\text{NO}} n_{\text{N2A}} - k_{6r} n_{\text{NOA}} n_{\text{N2}} - k_{7f} n_{\text{NOA}}
\end{aligned} \quad (11)$$

$$\begin{aligned}
\frac{dn_{\text{N2A}}}{dt} = & k_{3f} n_{\text{N2}} n_e - k_{3r} n_{\text{N2A}} n_e + k_{4f} n_{\text{N2}} n_{\text{N}} - k_{4r} n_{\text{N2A}} n_{\text{N}} \\
& + k_{5f} n_{\text{N}}^2 n_{\text{M}} - k_{5r} n_{\text{N2A}} n_{\text{M}} - k_{6f} n_{\text{NO}} n_{\text{N2A}} + k_{6r} n_{\text{NOA}} n_{\text{N2}}
\end{aligned} \quad (12)$$

A great simplification in the investigation of these equations comes from the fact that Reactions 1 through 7 do not appreciably affect the number densities of the unexcited species  $n_{\text{N2}}$ ,  $n_{\text{O2}}$ ,  $n_{\text{NO}}$ ,  $n_{\text{N}}$ ,  $n_{\text{O}}$ ,  $n_{\text{NO}}^{\dagger}$ , and  $n_e$ . This follows from the fact that the excited species number densities  $n_{\text{NOA}}$  and  $n_{\text{N2A}}$  are about  $e^{-70000/T} \approx 5 \times 10^{-6}$  to  $5 \times 10^{-10}$  of the corresponding ground state species number densities. To produce ground state species at an appreciable rate from these excited states would require rate constants that were proportionately greater than the rates used for ground-state chemistry. Likewise, the chemistry represented by these reactions does not affect the enthalpy or temperature history of the gas behind the shock wave.

With this simplification Equations (11) and (12) can be rewritten as

$$\frac{dn_{NOA}}{dt} = [k_{1f} n_{N_0} n_e + k_{2f} n_N n_M n_0] - [k_{1r} n_e + k_{2r} n_M + k_{7f}] n_{NOA} + [k_{6f} n_{N_0}] n_{N_2A} - [k_{6r} n_{N_2}] n_{NOA} \quad (13)$$

$$\begin{aligned} \frac{dn_{N_2A}}{dt} = & [k_{3f} n_{N_2} n_e + k_{4f} n_{N_2} n_N + k_{5f} n_N^2 n_M] \\ & - [k_{3r} n_e + k_{4r} n_N + k_{5r} n_M] n_{N_2A} \\ & - [k_{6f} n_{N_0}] n_{N_2A} + [k_{6r} n_{N_2}] n_{NOA} \end{aligned} \quad (14)$$

The rate constants are specified as functions of the temperature, and the species number densities inside the brackets are known functions of the distance behind the shock wave. It follows that if the ground-state chemistry behind the shock is known, then for a given choice of rate constants, the bracketed terms can be considered as known functions of the time, and the two equations can be integrated numerically to determine  $n_{NOA}$  and  $n_{N_2A}$ .

The relation between the forward and reverse rates can be written explicitly as

$$\begin{aligned} \frac{k_{1r}}{k_{1f}} &= \left( \frac{n_{N_0}}{n_{NOA}} \right)_{EQ} = \left( \frac{d_{NOX}}{d_{NOA}} \right) e^{\frac{E_{NOA}}{KT}}; \quad \frac{k_{3r}}{k_{3f}} = \left( \frac{n_{N_2}}{n_{N_2A}} \right)_{EQ} = \left( \frac{d_{N_2X}}{d_{N_2A}} \right) e^{\frac{E_{N_2A}}{KT}} = \frac{k_{4r}}{k_{4f}} \\ \frac{k_{2r}}{k_{2f}} &= \left( \frac{n_N n_0}{n_{NOA}} \right)_{EQ} = \left( \frac{n_N n_0}{n_{NOX}} \right)_{EQ} \cdot \left( \frac{n_{NOX}}{n_{NOA}} \right)_{EQ} = \left( \frac{n_N n_0}{n_{NOX}} \right)_{EQ} \cdot \left( \frac{d_{NOX}}{d_{NOA}} \right) e^{\frac{E_{NOA}}{KT}} \\ \frac{k_{5r}}{k_{5f}} &= \left( \frac{n_N^2}{n_{N_2A}} \right)_{EQ} = \left( \frac{n_N^2}{n_{N_2}} \right)_{EQ} \cdot \left( \frac{n_{N_2}}{n_{N_2A}} \right)_{EQ} = \left( \frac{n_N^2}{n_{N_2}} \right)_{EQ} \cdot \left( \frac{d_{N_2X}}{d_{N_2A}} \right) e^{\frac{E_{N_2A}}{KT}} \end{aligned} \quad (15)$$

where the terms  $d_i$  are the degeneracy of the  $i^{\text{th}}$  state:

$$d_{N_2X}=1; \quad d_{N_2A}=3; \quad d_{NOX}=4; \quad d_{NOA}=2$$

Since very little is known about the values of the rate constants, there is some merit in simplifying the equations further. It is first observed that the sum of Equations (13) and (14) provides an equation that does not involve the exchange reactions:

$$\begin{aligned}
\frac{dn_{NOA}}{dt} + \frac{dn_{N2A}}{dt} = & [k_{1f} n_{NO} n_e + k_{2f} n_N n_O n_M + k_{3f} n_{N2} n_e + k_{4f} n_{N2} n_N \\
& + k_{5f} n_N^2 n_M] - [k_{1r} n_e + k_{2r} n_M + k_{7f}] n_{NOA} \\
& - [k_{3r} n_e + k_{4r} n_N + k_{5r} n_M] n_{N2A}
\end{aligned} \quad (16)$$

If it is next assumed that the exchange reactions are very fast compared with the other excitation reactions,  $n_{NOA}$  and  $n_{N2A}$  will remain in a local thermal equilibrium with each other, so that

$$\frac{n_{NOA}}{n_{N2A}} \equiv Q = \frac{dn_{N2A}}{dn_{N2A}} \cdot \frac{dn_{NOA}}{dn_{NOA}} \cdot \frac{n_{NO}}{n_{N2}} e^{\frac{E_{N2A} - E_{NOA}}{KT}} = \frac{1}{6} \frac{n_{NO}}{n_{N2}} e^{\frac{8076}{T}} \quad (17)$$

$Q$  is then a known function of time behind the shock wave, with a value between 0 and about 0.1.

Substituting Equations (15) and (17) in Equation (16) results in

$$\frac{dZ}{dt} = F - \frac{Q}{(1+Q)} G \cdot Z \quad (18)$$

where  $Z$ ,  $F$ , and  $G$  are defined as

$$Z = n_{NOA} + n_{N2A} ; n_{N2A} = \frac{Z}{(1+Q)} ; n_{NOA} = \frac{QZ}{(1+Q)} \quad (19)$$

$$F = k_{1f} n_{NO} n_e + k_{2f} n_N n_O n_M + k_{3f} n_{N2} n_e + k_{4f} n_{N2} n_N + k_{5f} n_N^2 n_M \quad (20)$$

$$\begin{aligned}
G = & \left[ \frac{k_{1f} n_{NO} n_e + k_{3f} n_{N2} n_e + k_{4f} n_{N2} n_N}{P_1} + \frac{k_{2f} n_N n_O n_M}{P_2} \right. \\
& \left. + \frac{k_{5f} n_N^2 n_M}{P_3} + k_7 \right] \quad (21)
\end{aligned}$$

and  $p_1$ ,  $p_2$ , and  $p_3$  are defined as

$$p_1 = \frac{dn_{NOA}}{dn_{NOX}} e^{-\frac{E_{NOA}}{kT}} \cdot n_{NO} \quad (22)$$

$$p_2 = \frac{dn_{NOA}}{dn_{NOX}} e^{-\frac{E_{NOA}}{kT}} \cdot n_{NO} \left( \frac{n_{NO}}{n_N n_O} \right)_{EQ} \cdot \frac{n_N n_O}{n_{NO}} \quad (23)$$

$$p_3 = \frac{dn_{NOA}}{dn_{NOX}} e^{-\frac{E_{NOA}}{kT}} \cdot n_{NO} \left( \frac{n_{N2}}{n_N^2} \right)_{EQ} \cdot \frac{n_N^2}{n_{N2}} \quad (24)$$

$p_1$  is the value of  $n_{NOA}$  in local thermodynamic equilibrium with  $n_{NOX}$ ,  $p_2$  is the value of  $n_{NOA}$  in LTE with  $n_{NNO}$ , and  $p_3$  is the value of  $n_{NOA}$  in LTE with  $n_{N2}$ , all under the condition that  $n_{NOA}$  and  $n_{N2A}$  are in local thermodynamic equilibrium with each other. In final equilibrium,  $p_1 = p_2 = p_3$ . Equation (18) provides the differential equation for  $n_{NOA}(t)$ .

A final simplification that is appropriate over much of the relaxation zone is the assumption that  $Z$  is near local equilibrium -- i.e.,  $dZ/dt$  is small compared with the terms  $F$  or  $(Q/(1+Q))GZ$  in Equation (18). This is true when changes in the ground-state chemistry are slow compared with the electronic excitation mechanisms. In this case  $Z$  can be taken as

$$Z = Z_{LE} = (F/G) ((1+Q)/Q), \text{ or } (n_{NOA})_{LE} = (F/G). \quad (25)$$

This local equilibrium value is somewhere between the local values of  $p_1$ ,  $p_2$ , and  $p_3$ , depending on the relative values of the numerators of the three terms in Equation (21). If  $k_7$  has an appreciable value compared with the other terms, it serves to lower the local equilibrium value of  $n_{NOA}$ .



When the ground-state chemistry arrives at final equilibrium,  $p_1=p_2=p_3 = (n_{NOA})_{FE}$ . (see Equations 22-24), and

$$(n_{NOA})_{LE} = \frac{F}{G} = \frac{F}{\frac{F}{(n_{NOA})_{FE}} + k_7} \quad (26)$$

If  $k_7 \ll F/(n_{NOA})_{FE}$ , then  $(n_{NOA})_{LE} = (n_{NOA})_{FE}$ , and the equilibrium radiation is not "collision limited."

### 3.5 Rate Constants for Electronic Excitation

As discussed in Section 3.4, References 11 and 12 give assessments of the state of knowledge of excitation mechanisms and rates for excitation of the  $A^3\Sigma$  state of NO. The group of 7 mechanisms discussed here was chosen from those reports, and the initial set of rates that was compared with the present experimental data was taken from Reference 11. These rates are written in the form

$$k_f = AT^B e^{-C/T} \quad (27)$$

where the values of A, B, and C are given in Table 3. The units of the rate constants are ( $\text{cm}^3/\text{molecule sec}$ ) or ( $\text{cm}^6/\text{molecule}^2\text{sec}$ ).

			A	B	C
1.	NO+e	$\rightleftharpoons$ NO(A)+e	$1.2 \times 10^{-10}$	0	63,510
2.	N+O+M	$\rightleftharpoons$ NO(A)+M	$2.47 \times 10^{-31}$	-1.24	0
3.	N <sub>2</sub> +e	$\rightleftharpoons$ N <sub>2</sub> (A)+e	$1.98 \times 10^{-9}$	0	71,586
4.	N <sub>2</sub> +N	$\rightleftharpoons$ N <sub>2</sub> (A)+N	$1.53 \times 10^{-2}$	-2.23	71,586
5.	N+N+M	$\rightleftharpoons$ N <sub>2</sub> (A)+M	$1.27 \times 10^{-27}$	-1.60	0
6.	NO(X)+N <sub>2</sub> (A)	$\rightleftharpoons$ NO(A)+N <sub>2</sub> (X)	inf.	----	---
7.	NO(A)	$\rightarrow$ NO(X)+h $\nu$	$5 \times 10^6$	----	---

TABLE 3. INITIAL RATES USED, REFERENCE 11

The rates for the reverse reactions are taken to be related through the equilibrium constants. Reaction 7 proceeds in only one direction because the gas is optically thin.

An important conclusion of the study of the equilibrium UV radiation was that the radiation was not collision limited. This means that at equilibrium the term  $k_7$  (Equation (21) Section 3.4) is negligible compared with the other terms in that equation. Typical values of these other terms at equilibrium, for various shock conditions, are shown in Table 4. The initial pressure in the shock tube was 2.25 torr for all cases.

Some of the terms, in each case, should be considerably greater than  $5 \times 10^6 \text{sec}^{-1}$  in order to avoid collision limiting. Although this is satisfied for the 5% oxygen experiments (the highest temperatures), it is not satisfied at the lower temperatures associated with the 22.3% and 40% oxygen equilibrium conditions. Thus if the excitation process is to be represented by these relations, appreciably faster rates must be used.

The first two rate columns in Table 4 show that the electron reactions are the slowest of all the rates. This is related, of course, to the small number of electrons that are present at these relatively slow shock speeds. The temperature dependence of the electron concentrations is such that these rates become more important at higher temperatures, but it is unlikely that they are involved in the excitation being discussed here.

The last three rates have comparable magnitudes, but the direct-excitation rate,  $k_{4f}$ , has the strongest temperature dependence. The value of the last two terms, the recombination terms, are very dependent on the degree of equilibrium, since they depend on the square of the atom concentrations. At conditions near the shock, where few atoms are present, they serve to quench the radiation by dissociating the excited state of NO or of  $N_2$ .

Under the assumption that changes in the ground-state chemistry rates are slow compared with the electronic excitation mechanisms, Equation (26) can be used to describe the population of NO in the A state, and thus (with Equation (6)) can be used to compare with the signal received from the Gamma radiation. Then

$$S_{NOA} = (\ell |Re|_{NO}^2 \cdot M_{NO}) \frac{F}{G} \quad \text{watts/cm}^2\text{sr} \quad (28)$$

$V$ mm/ $\mu s$	$O_2/N_2$	$T_{eq}$ $^{\circ}K$	$k_{1f} \cdot nNOn_e/p_1$	$k_{3f} \cdot nN_2n_e/p_1$	$k_{4f} \cdot nN_2nN/p_1$	$k_{2f} \cdot nNnOnM/p_2$	$k_{5f} \cdot nMnN/p_3$
3.86	5/95	4893	$3.96 \times 10^3$	$2.47 \times 10^6$	$1.63 \times 10^8$	$1.86 \times 10^6$	$1.75 \times 10^8$
3.50		4307	$9.83 \times 10^2$	$3.18 \times 10^5$	$2.29 \times 10^7$	$1.49 \times 10^6$	$3.30 \times 10^7$
3.37		4050	$4.76 \times 10^2$	$1.09 \times 10^5$	$8.04 \times 10^6$	$1.34 \times 10^6$	$1.38 \times 10^7$
3.78	22.3/77.7	3740	$3.84 \times 10^2$	$1.18 \times 10^4$	$4.12 \times 10^5$	$1.68 \times 10^6$	$1.29 \times 10^6$
3.65		3617	$2.33 \times 10^2$	$6.37 \times 10^3$	$2.35 \times 10^5$	$1.53 \times 10^6$	$8.09 \times 10^5$
3.36		3365	$7.07 \times 10^1$	$1.62 \times 10^3$	$6.93 \times 10^4$	$1.20 \times 10^6$	$2.90 \times 10^5$
3.84	40/60	3546	$2.12 \times 10^2$	$3.02 \times 10^3$	$8.58 \times 10^4$	$1.72 \times 10^6$	$4.02 \times 10^5$
3.55		3369	$8.73 \times 10^1$	$1.16 \times 10^3$	$3.75 \times 10^4$	$1.39 \times 10^6$	$1.98 \times 10^5$
3.24		3169	$2.78 \times 10^1$	$3.52 \times 10^2$	$1.37 \times 10^4$	$1.06 \times 10^6$	$8.41 \times 10^4$

TABLE 4. TYPICAL TERMS FROM EQUATION (21), AT EQUILIBRIUM (sec<sup>-1</sup>)

$$S_{NOA} = (\ell |Re|_{w_0}^2 M_{NO}) \{ [k_4 m_N^2 n_N + k_2 m_N n_O n_M + k_5 m_M n_N^2] / \\ \{ [k_4 m_N^2 n_N / p_1] + [k_2 m_N n_O n_M / p_2] + k_5 m_M n_N^2 / p_3 \} \} \quad (29)$$

The electron excitation terms,  $k_1$  and  $k_3$ , and the emission term  $k_7$  have been dropped from the relation as being negligibly small. Only the ratios of the remaining rate constants are relevant in determining  $S_{NOA}$ , assuming that they are large enough to make  $k_7$  negligible. Thus there are two variables in fitting the calculation with the experiments. Many calculations of  $S_{NOA}$  were performed, using the Camac ground-state rates given in Table 1 and varying coefficients  $A_i$  for the  $k_2$ ,  $k_4$ , and  $k_5$  electronic excitation rates of Table 3 in an effort to match the experimental profiles. No reasonable match could be obtained.

The calculated ground-state chemistry shown in Figure 13 is reasonably consistent with the infrared radiation data, but employ unrealistic ground-state reaction rates. If this ground-state chemistry is used as the basis for calculation of the electronic state populations, a fair agreement there can also be obtained. A set of calculated nonequilibrium emission profiles for the matrix of 230 nm runs is shown in Figure (14). (The experimental results are shown in larger scale in Appendix E.) These calculations used a simplified table of coefficients for reactions of Table 3, as shown in Table 5.

RATE	A	B	C
1	$1.2 \times 10^{-10}$	0	63,510
2	$4.0 \times 10^{-34}$	0	0
3	$2.0 \times 10^{-9}$	0	71,586
4	$4.6 \times 10^{-8}$	0	71,586
5	$5.2 \times 10^{-32}$	0	0
6	Infinity	----	----
7	$5 \times 10^6$	----	----

TABLE 5. COEFFICIENTS USED IN CALCULATION OF FIGURE 14

The pre-exponential temperature dependence was omitted in all cases. The ratios of the  $A_i$  (e.g.  $A_4/A_2$ ) are determined by the shape of the curves. The magnitudes of the coefficients were chosen so that the rates would be large compared with the radiative emission rate. Rates 1 and 3 do not affect the results.

## ACKNOWLEDGEMENTS

The authors gratefully acknowledge the contributions of Messrs. J.R. Ambrusko, R.J. Hiemenz and J. Johnson to the experimental aspects of this research.

## REFERENCES

1. Wurster, W.H., Treanor, C.E., and Williams, M.J., "Nonequilibrium UV Radiation and Kinetics Behind Shock Waves in Air", AIAA-89-1918, June 1989. (Appendix A).
2. Wurster, W.H., Treanor, C.E., and Williams, M.J., "Kinetics of UV Production Behind Shock Waves in Air", AIAA-90-1666, June 1990. (Appendix B).
3. Keck, J., Camm, J., and Kivel, B., "Absolute Emission Intensity of Schumann-Runge Radiation from Shock-Heated Oxygen", J. Chem. Phys. 28, 723 (1958). Kivel, B., "Radiation from Incident and Reflected Shocks in Air", AMP 39, Avco Research Laboratory, January 1960.
4. Gilmore, F.R., "Basic Energy Levels and Equilibrium Data for Atmospheric Atoms and Molecules", Rand Corporation Memo RM 5201-ARPA, March 1967.
5. Marrone, P.V. et al., "Inviscid, Nonequilibrium Flow Behind Bow and Normal Shock Waves", CAL Report No. QM-1626-A-12 (I-III), May 1963, October 1963.
6. K.L. Wray, Progress in Astronautics and Rocketry, Edited by F.R. Riddell (Academic Press, New York, 1962), Vol. 7, p. 181.
7. Camac, M., Feinberg, R., and Teare, J.D., Avco Research Report 245, December 1966.
8. Jorig, L., Theilen, K., Roth, P., AIAA Journal 29, 1136 (1991).
9. Hanson, R., et al., Combustion Chemistry, W.C. Gardner, Editor, Springer Verlag, 1984.
10. Marrone, P.V. and Treanor, C.E., "Phys. of Fluids", 6, 1215 (1963).
11. Smith, G.P., Crosley, D.R., Eckstrom, D.J., "Mechanisms and Rate Constants for the Chemistry of Radiating, Shock-Heated Air", SRI International Report MP89-037, February 1989.
12. Brown, R.C., Annen, K.D., and Kolb, C.E., "Analysis of UV Nosecap Radiation", Aerodyne Research, Inc., Report ARI-RR-771, May 1989.
13. Feinberg, R.M. and Camac, M., JQSRT 7, 581 (1967).

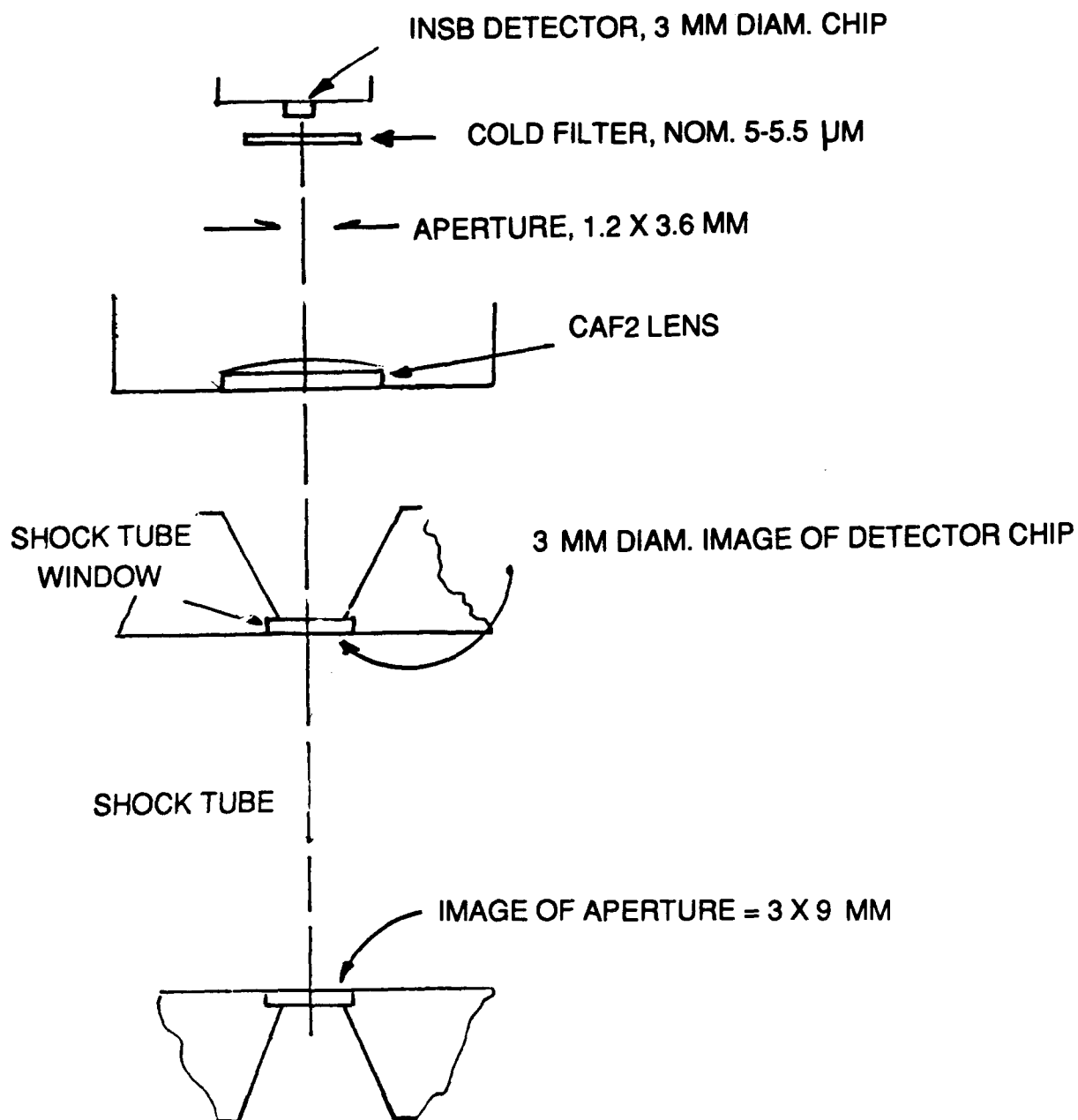


**FIGURE 1: MAJOR ELEMENTS OF THE IR RADIOMETER-SHOCK TUBE SYSTEM. THE BEAM IN THE SHOCK TUBE IS WEDGE-SHAPED, OPTIMIZED FOR AXIAL RESOLUTION AT 3MM, AND FOR THROUGHPUT BY A 9-MM WIDTH ACROSS THE TUBE AT THE LOWER WINDOW. MAGNIFICATION IS UNITY FOR THE DETECTOR CHIP AND 2.5 FOR THE APERTURE.**

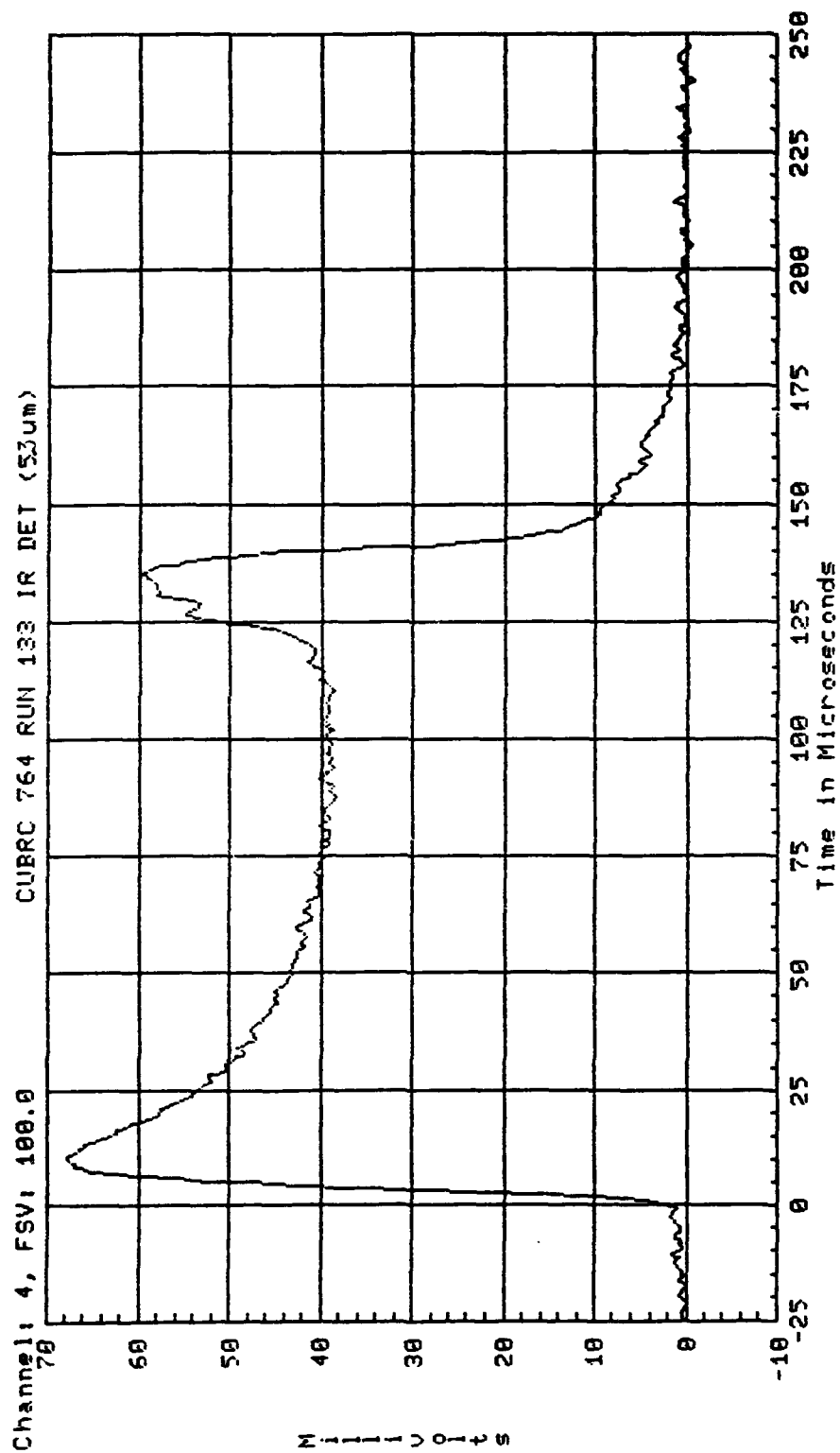


FIGURE 2. TYPICAL RAW DATA TRACE OF THE IR RADIOMETER, ILLUSTRATING IMPROVEMENT IN SCATTERED LIGHT REDUCTION. SEE TEXT FOR DETAILS.

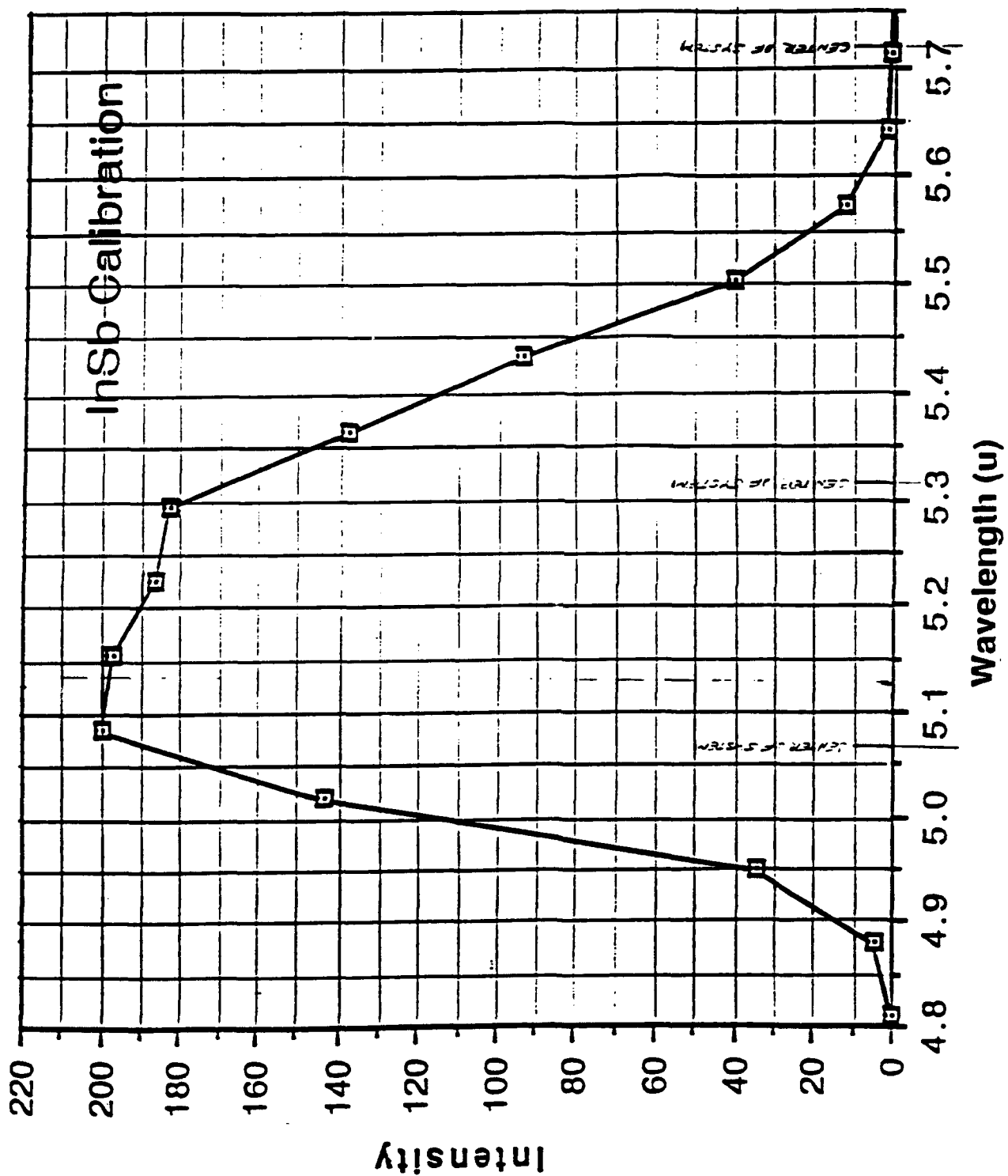


FIGURE 3. MEASURED WAVELENGTH RESPONSE OF THE RADIOMETER



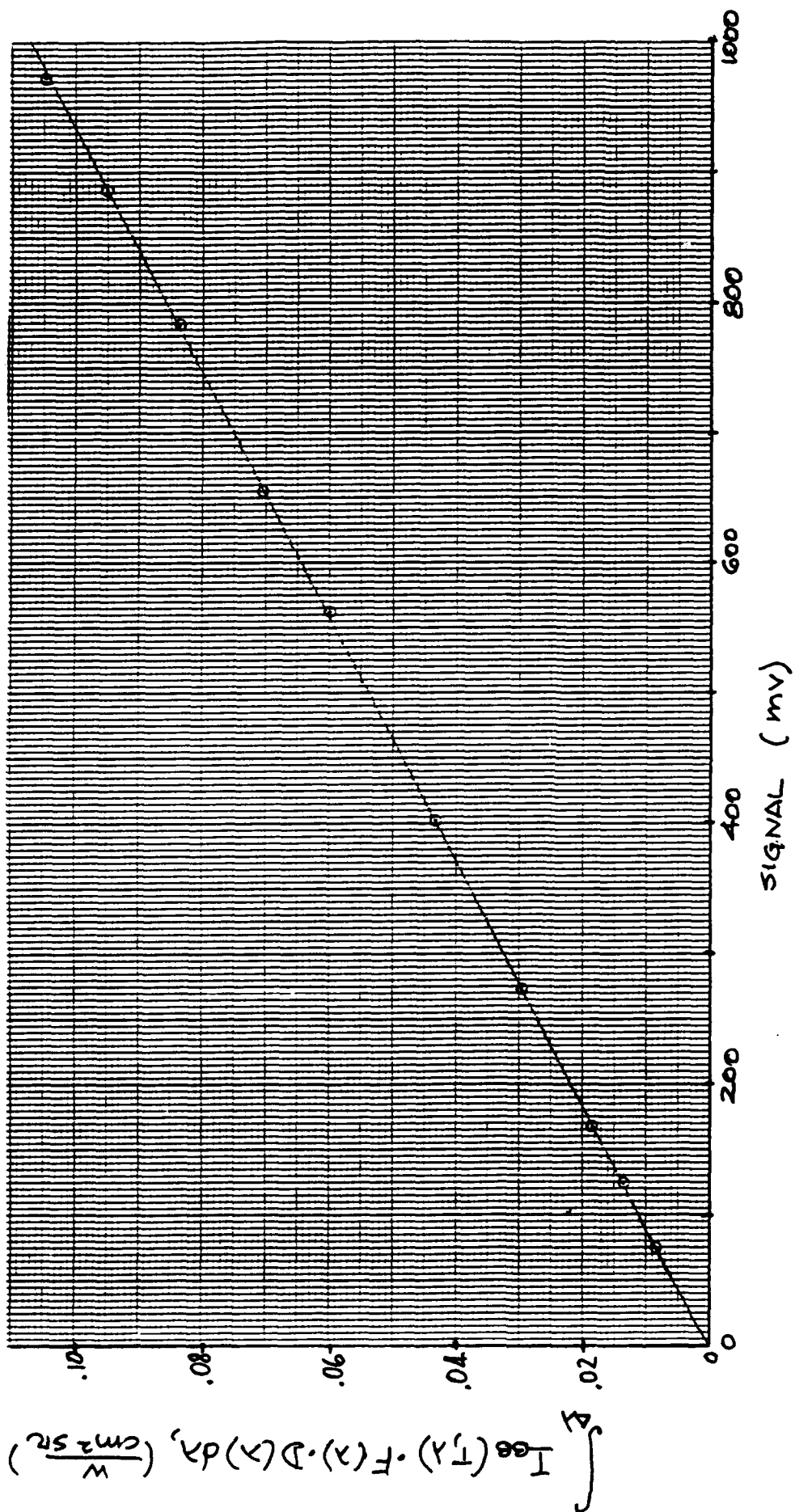


FIGURE 4. INTENSITY CALIBRATION OF THE RADIOMETER

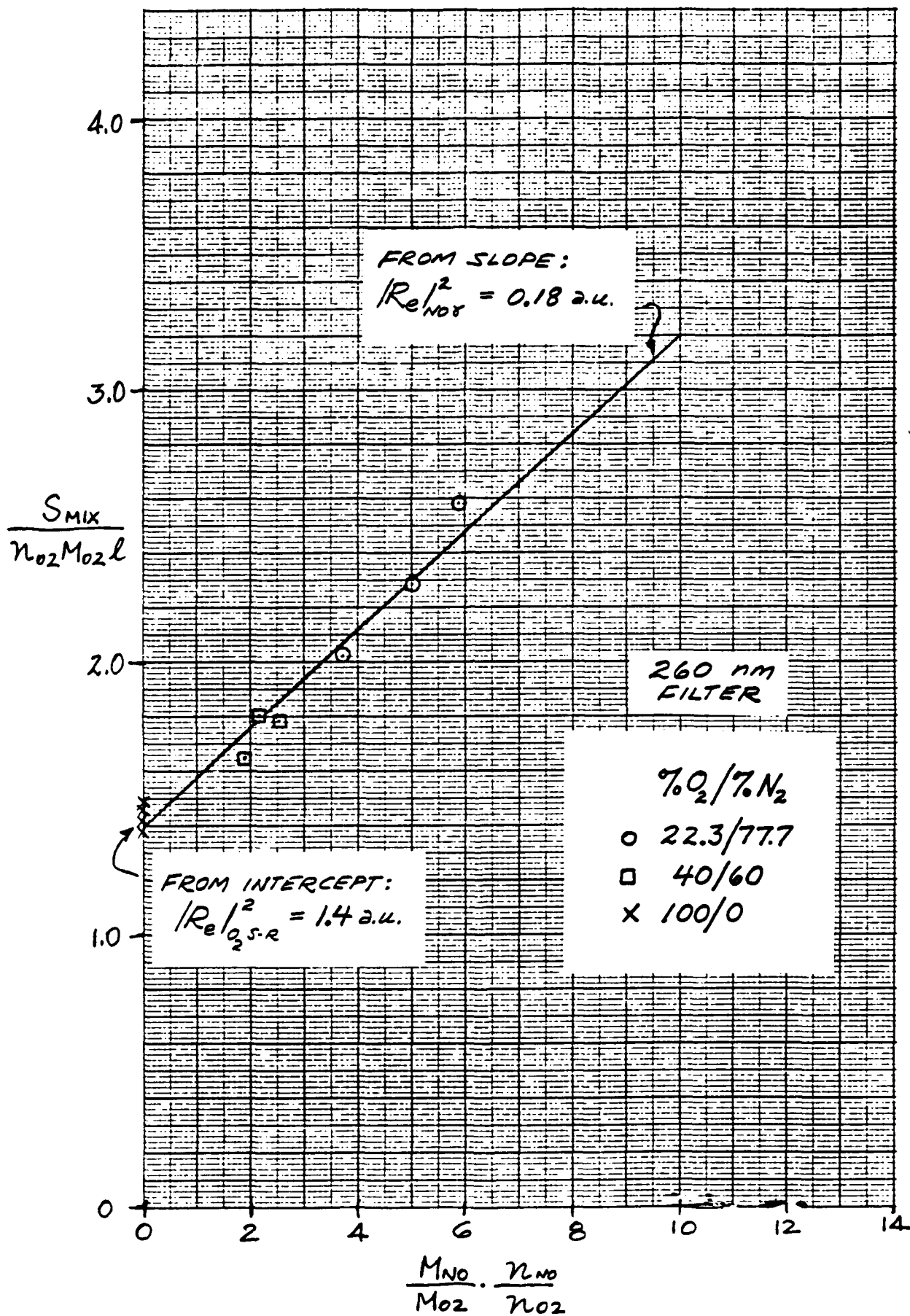


FIGURE 5. RADIATION MEASUREMENTS, 260 NM

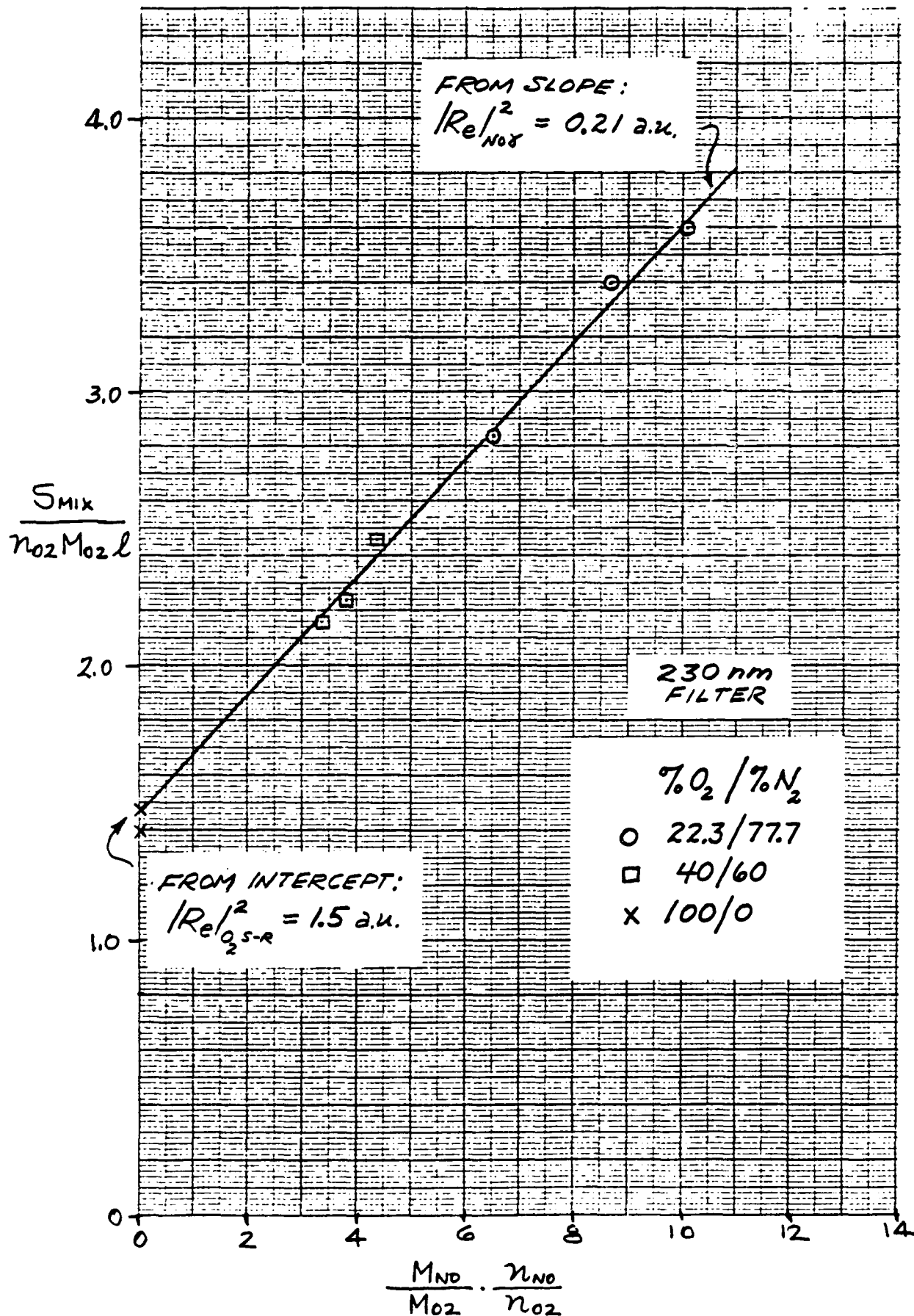
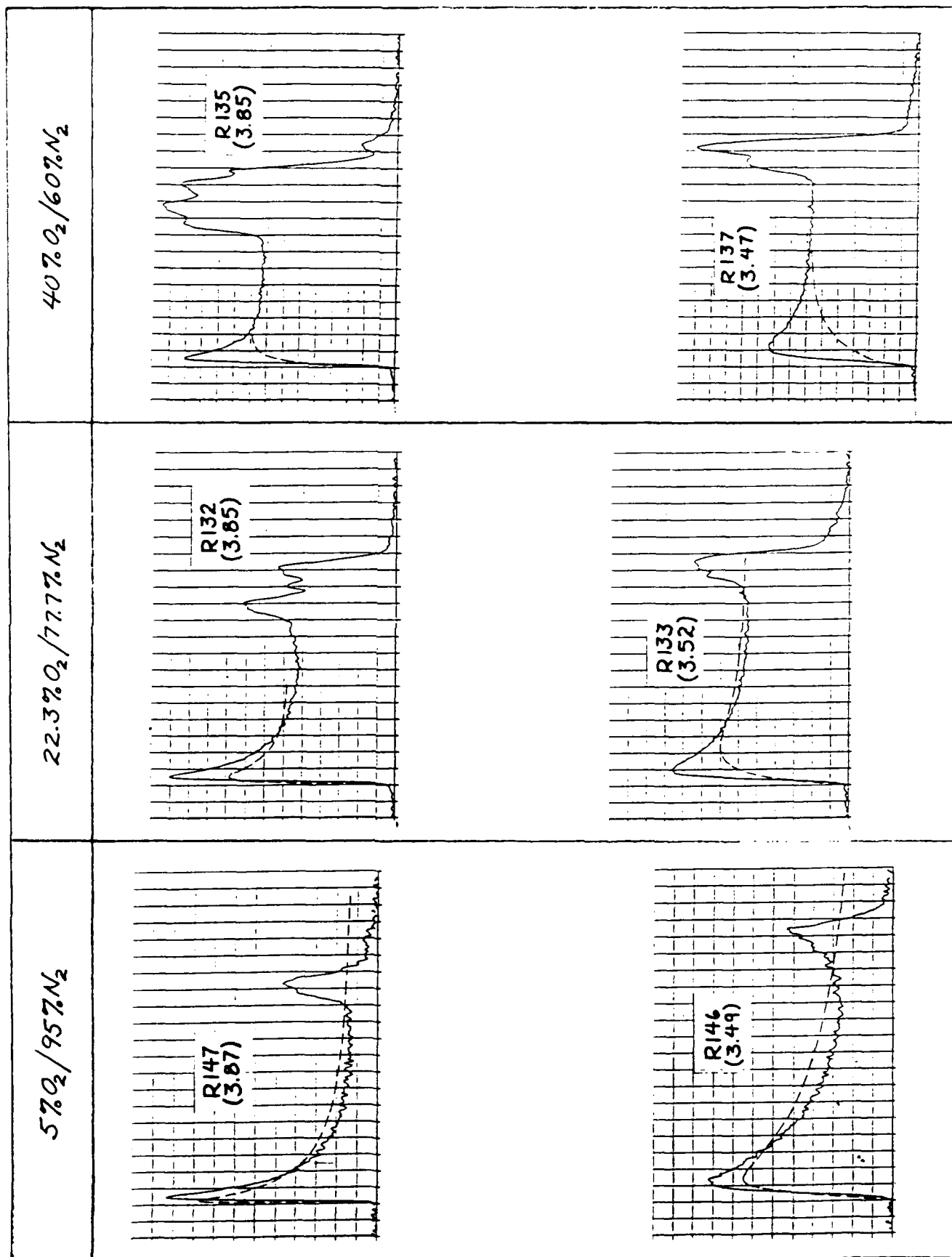


FIGURE 6. RADIATION MEASUREMENTS, 230 NM



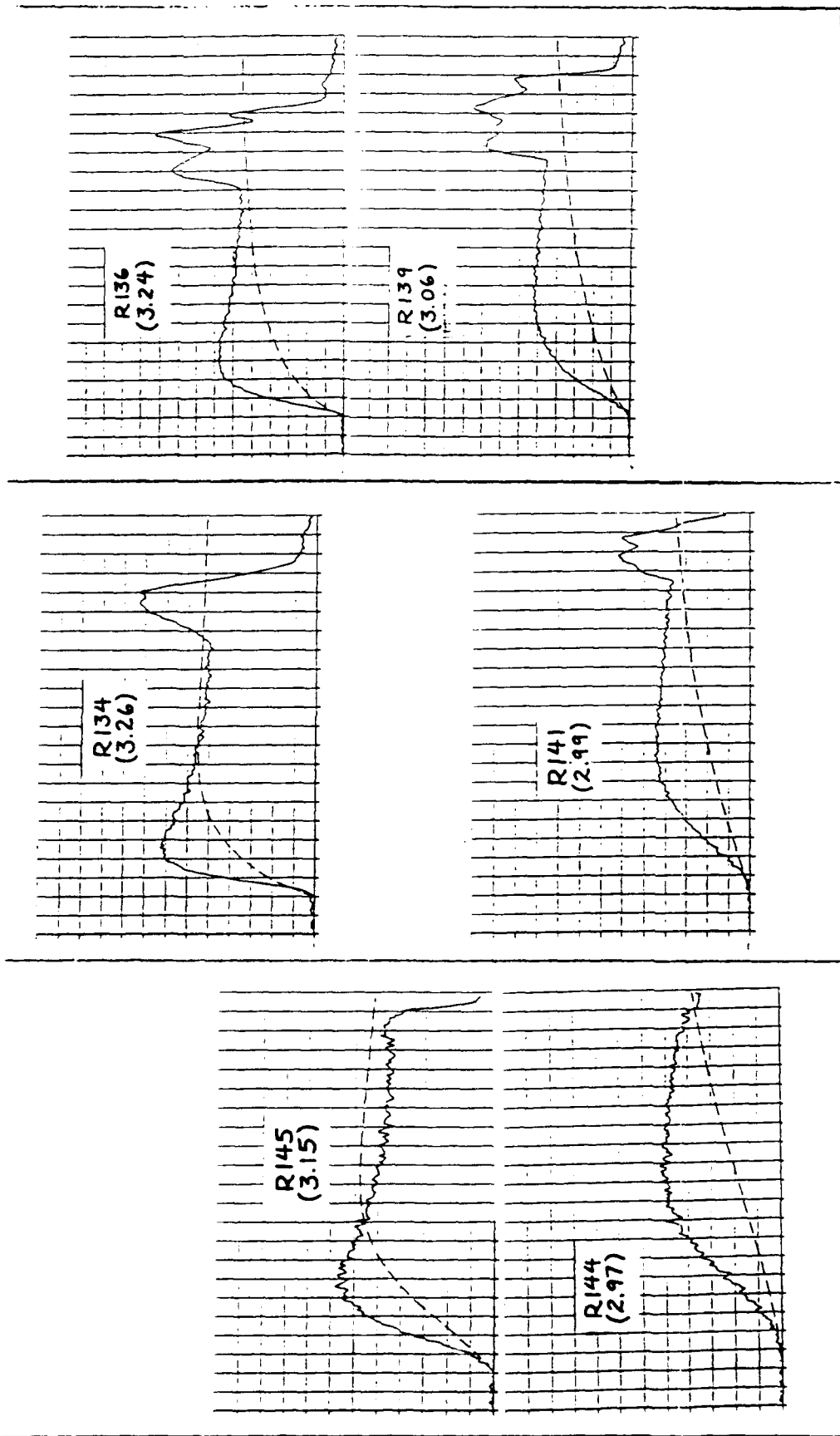


FIGURE 7. MATRIX OF MEASURED AND CALCULATED 5.3μm RADIANCE PROFILES, FOR DIRECT INTERCOMPARISONS OF PROFILE TRENDS WITH CHANGES IN SHOCK VELOCITY AND O<sub>2</sub>/N<sub>2</sub> MIXTURE RATIOS. IN EACH COLUMN, FOR THE NOTED MIXTURE, THE RECORDS ARE SPACED ACCORDING TO THE VELOCITIES NOTED IN PARENTHESES, IN MM/US. ALL TESTS WERE RUN AT AN INITIAL PRESSURE OF 2.25 TORR; GAINS IN EACH COLUMN WERE HELD CONSTANT. RUN NUMBERS (DESIGNATED R) PROVIDE REFERENCES TO THE FULL-SCALE DATA RECORDS IN APPENDIX C, WHERE INTENSITIES IN WATTS/CM<sup>2</sup>-SR ARE PLOTTED AGAINST LAB TIME IN US. THE DASHED PROFILE IN EACH PLOT WAS CALCULATED USING CAMAC'S RATES.

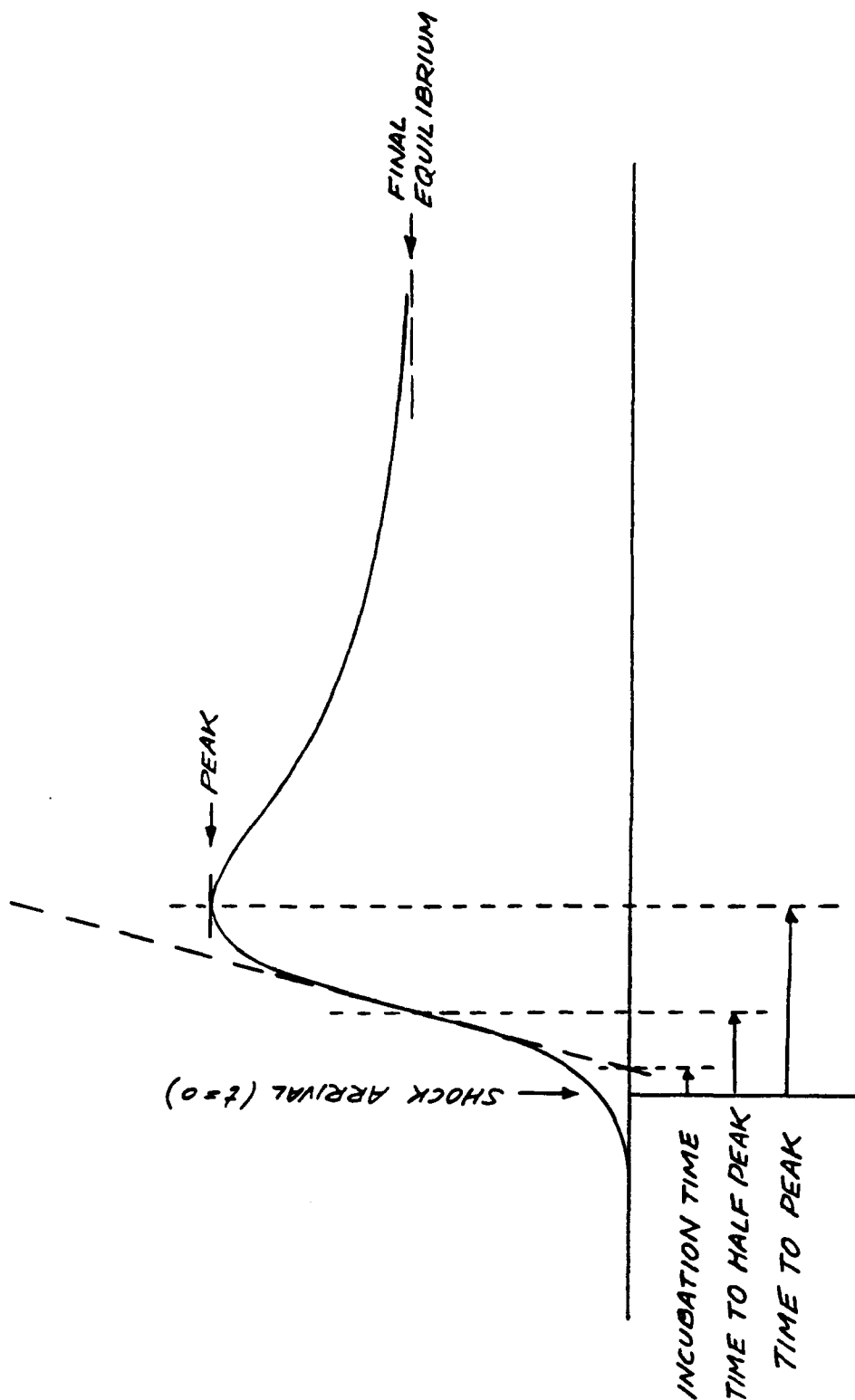


FIGURE 8. THREE TEMPORAL PARAMETERS CHARACTERIZING NON-EQUILIBRIUM INFRARED RADIATION

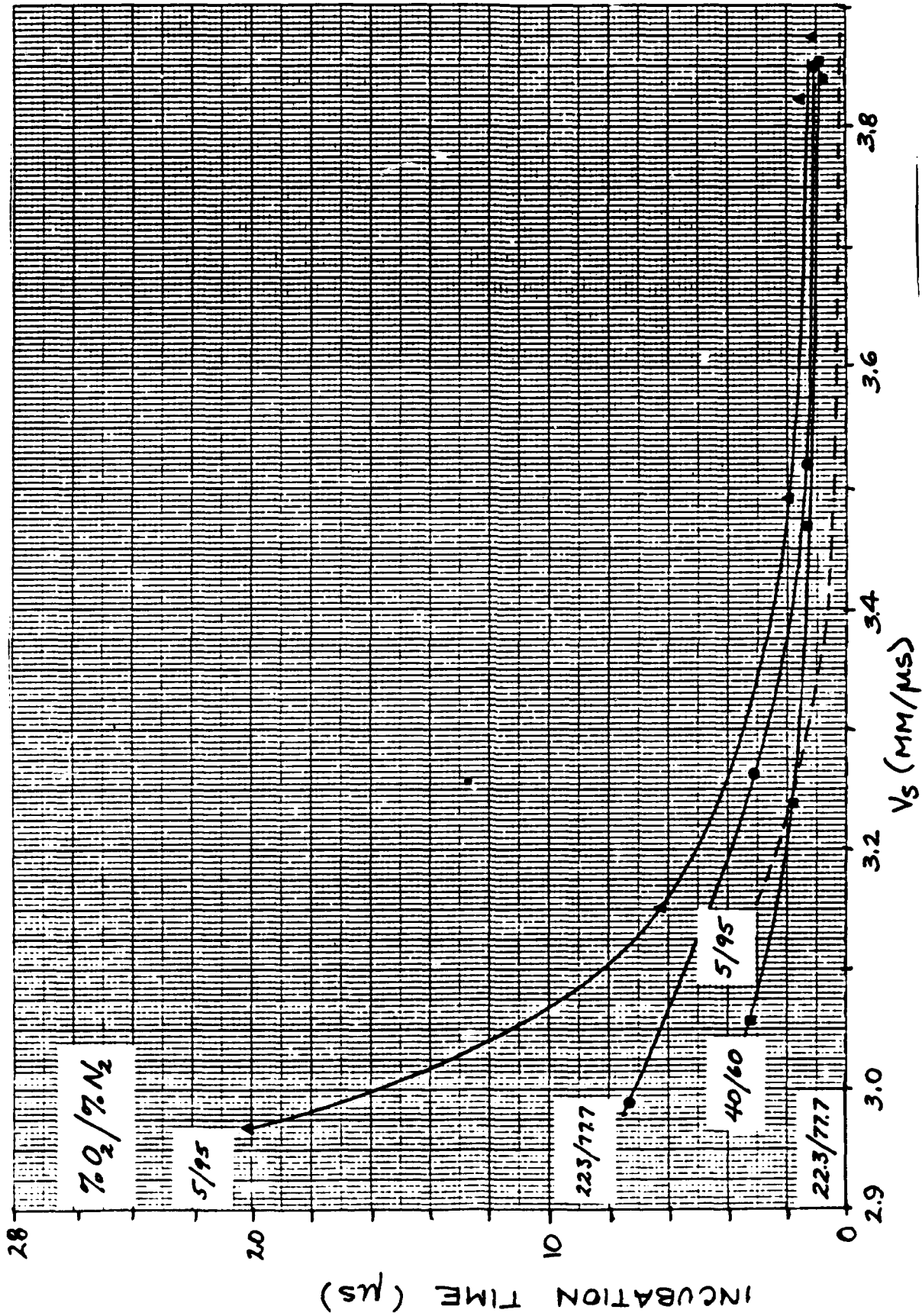


FIGURE. 9 VARIATION OF INCUBATION TIME WITH SHOCK VELOCITY FOR THREE O<sub>2</sub>/N<sub>2</sub> MIXTURES.  $P_1 = 2.25$  TORR.  
 - FROM 5.3 μm EXPERIMENTAL PROFILES ---FROM CALCULATED PROFILES (CAMAC RATES)

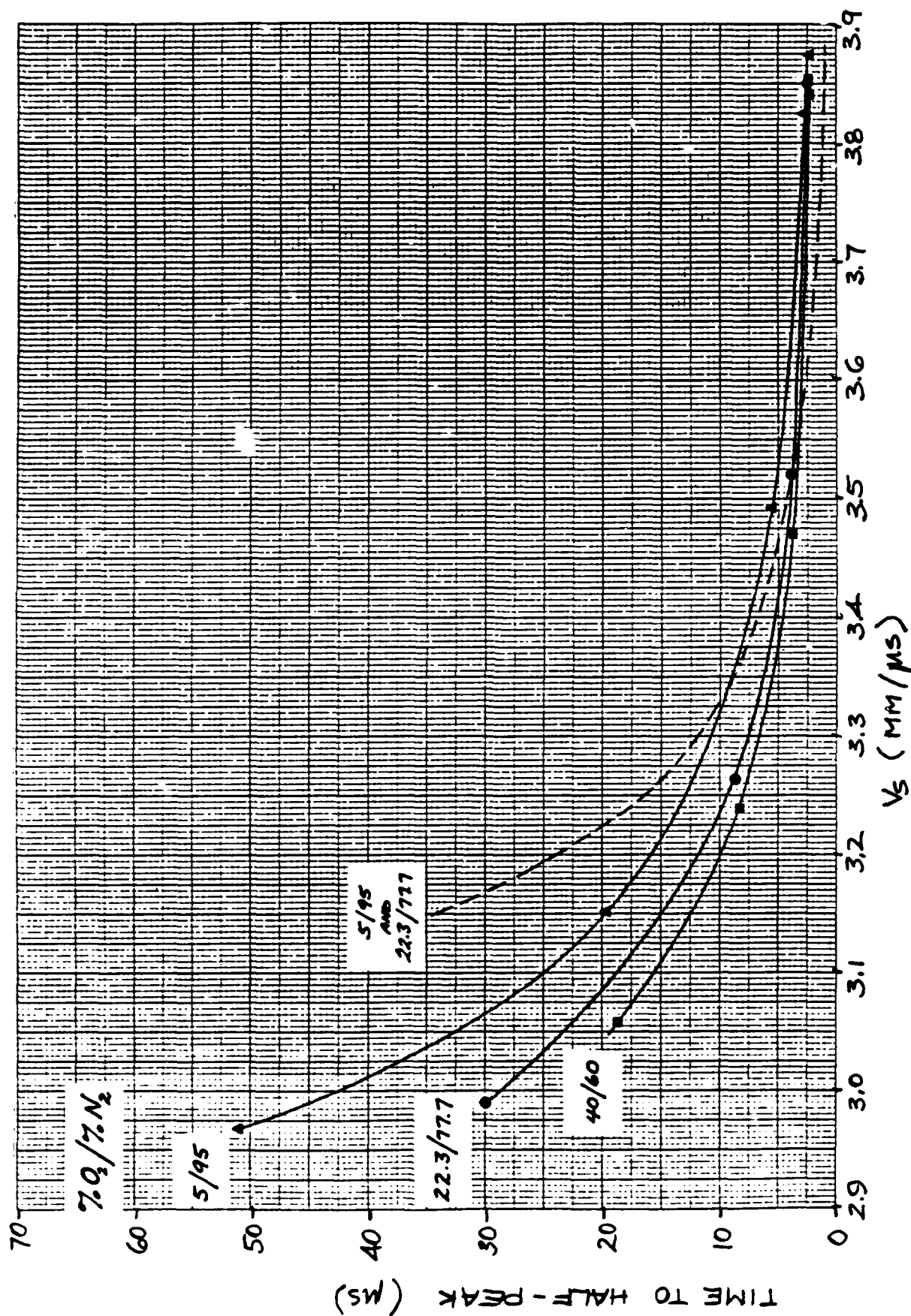


FIGURE 10. VARIATION OF TIME-TO-HALF-PEAK WITH SHOCK VELOCITY FOR THREE O<sub>2</sub>/N<sub>2</sub> MIXTURES. P<sub>1</sub> = 2.25 TORR.  
 ---FROM 5.3 μM EXPERIMENTAL PROFILES ---FROM CALCULATED PROFILES (CAMAC RATES)



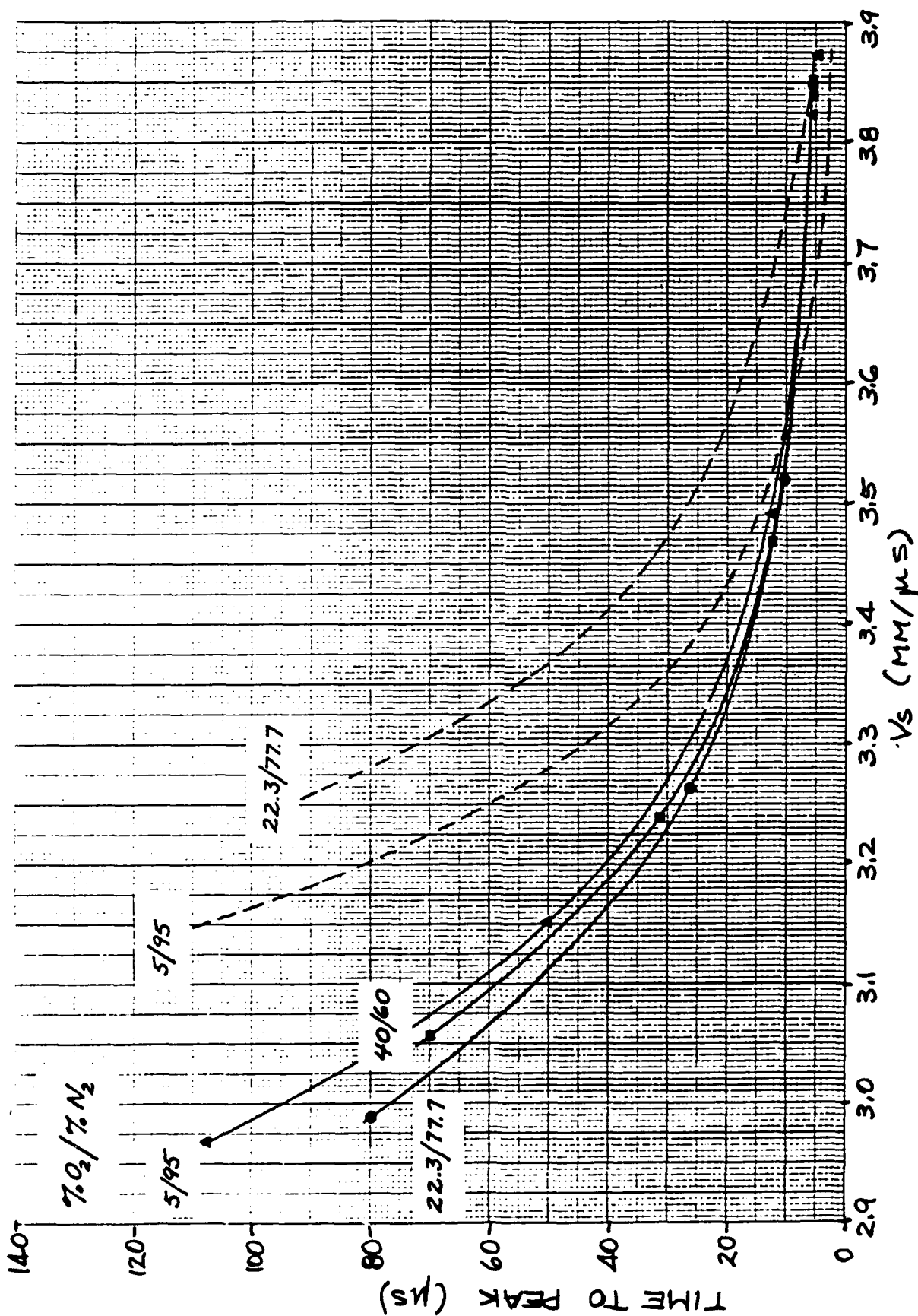


FIGURE 11. VARIATION OF TIME-TO-PEAK WITH SHOCK VELOCITY FOR THREE O<sub>2</sub>/N<sub>2</sub> MIXTURES. P<sub>1</sub> = 2.25 TORR.  
 -FROM 5.3 μM EXPERIMENTAL PROFILES --- FROM CALCULATED PROFILES (CAMAC RATES)

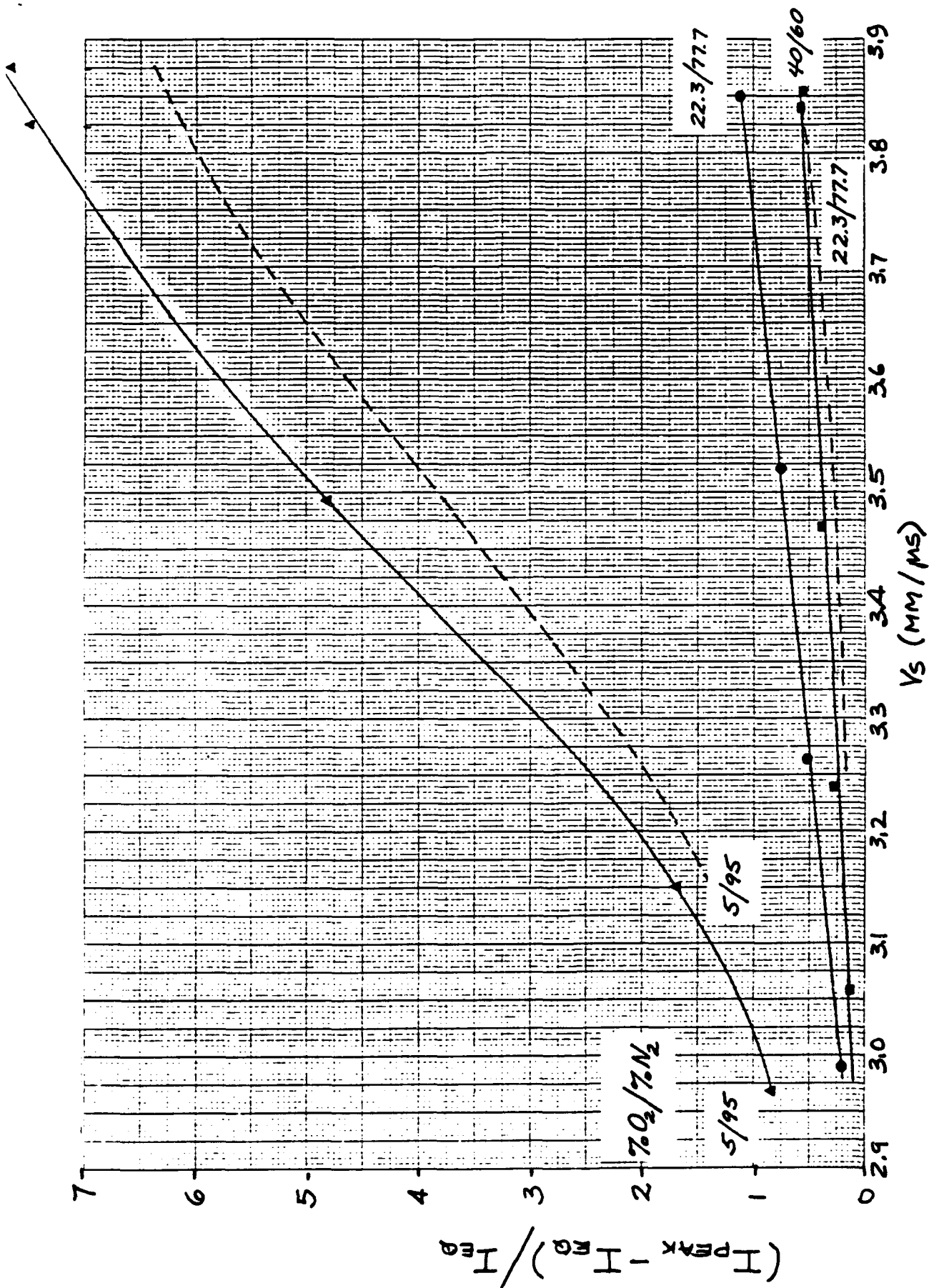
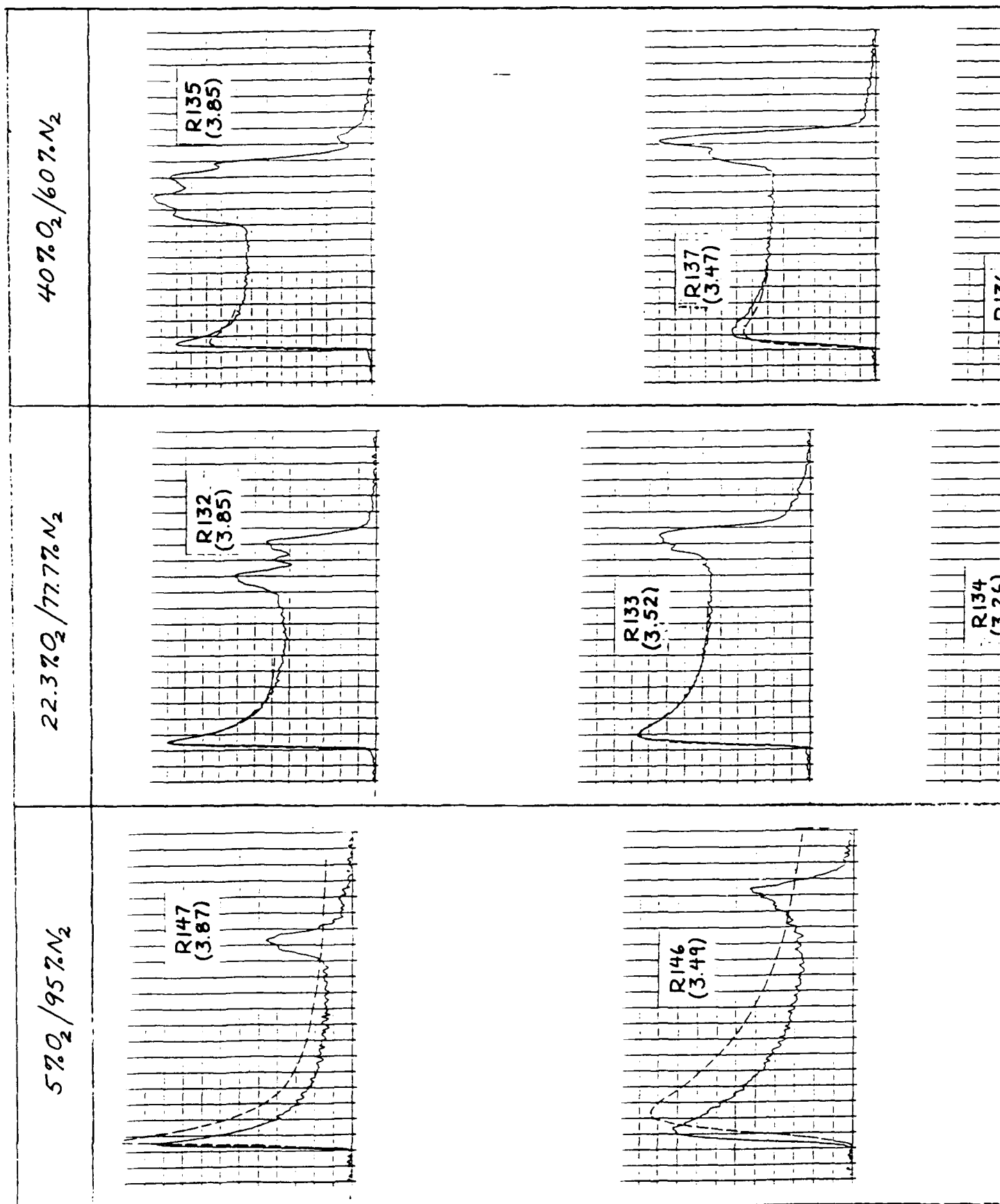


FIGURE 12. VARIATION OF PEAK INTENSITY RELATIVE TO EQUILIBRIUM INTENSITY FOR THREE  $O_2/N_2$  MIXTURES.  $P_1 = 2.25$  TORR. - FROM 5.3  $\mu$ M EXPERIMENTAL PROFILES ---FROM CALCULATED PROFILES (CAMAC RATES)



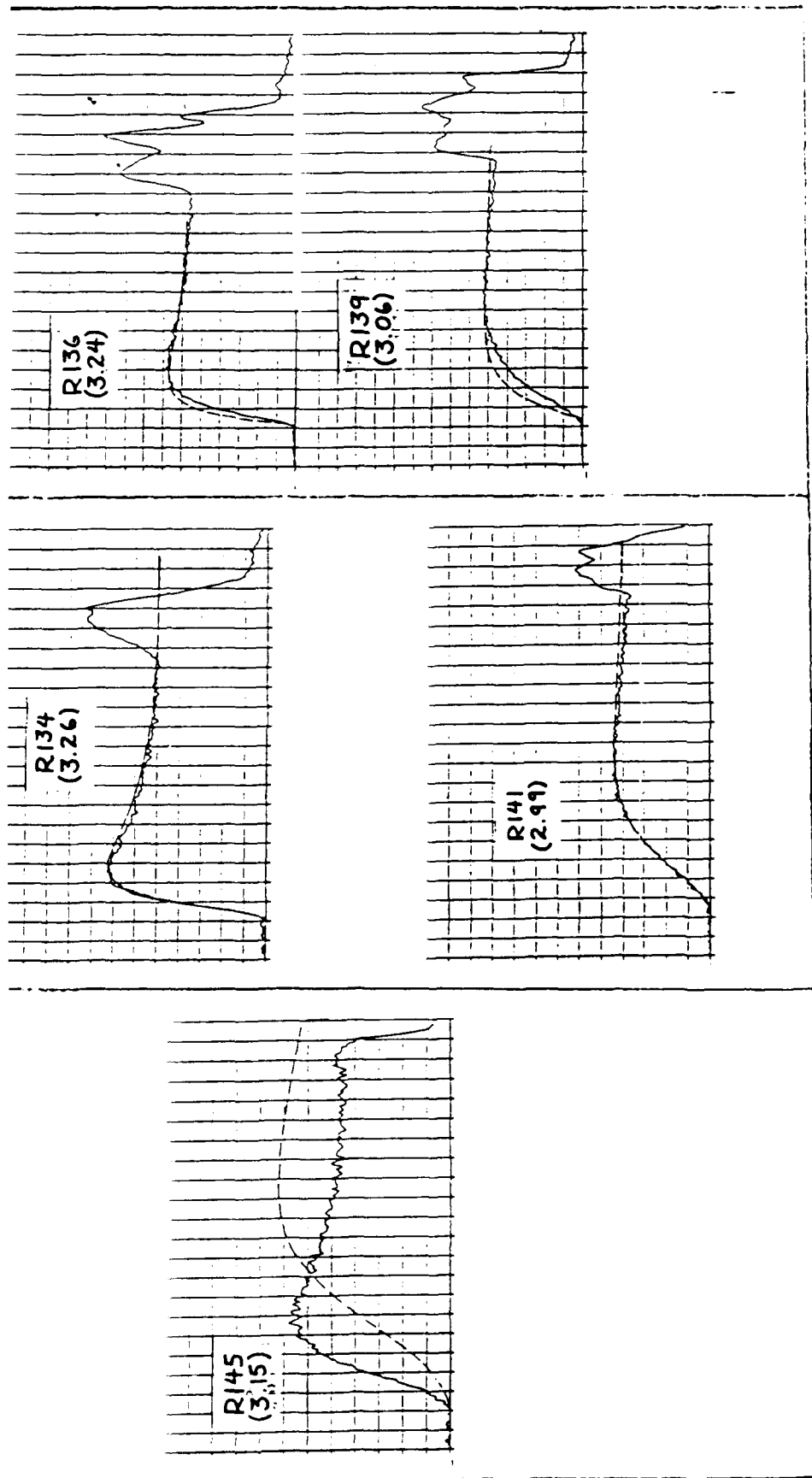
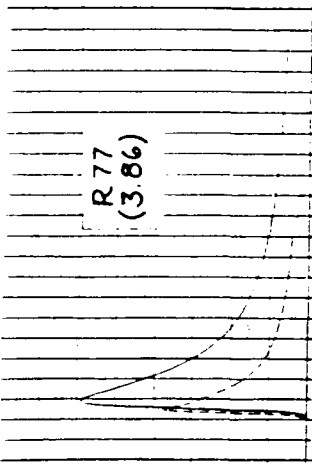
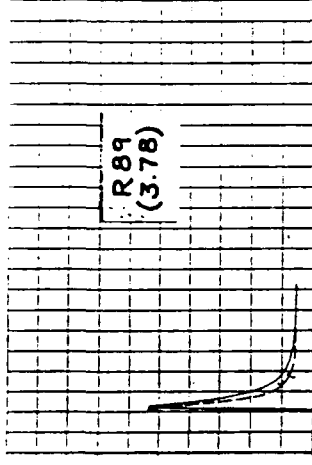
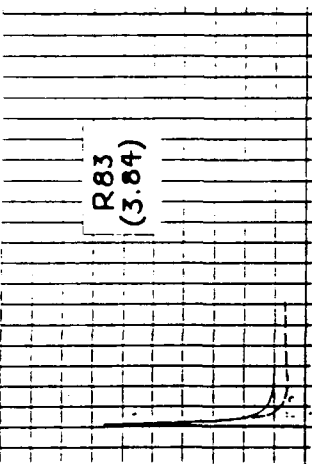
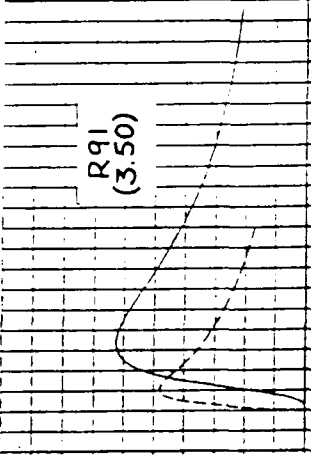
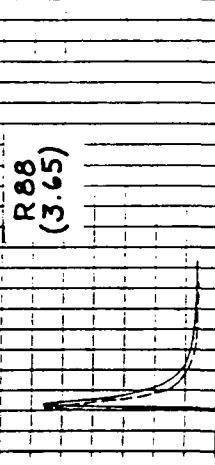
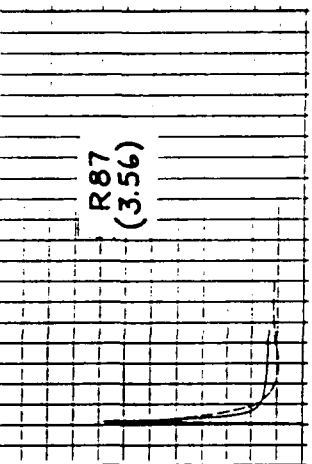
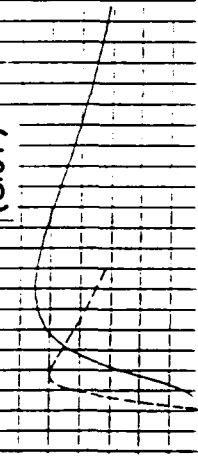
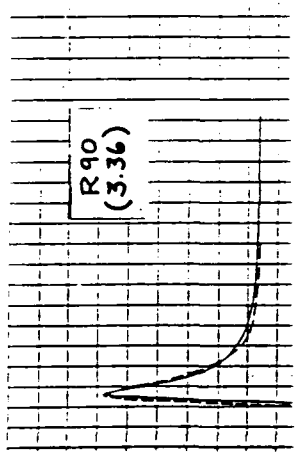



FIGURE 13. MATRIX OF MEASURED 5.3 $\mu$ m RADIANCE PROFILES. THE 'BEST FIT' CALCULATED CURVES (DASHED LINES) ARE ALSO SHOWN, BUT THE RATES USED ARE INCONSISTENT WITH OTHER INFORMATION AND ARE NOT PRESENTED. THE CALCULATED CURVES WERE USED IN ANALYSIS OF THE OBSERVED ULTRAVIOLET RADIATION. SEE TEXT FOR DETAILS. THE PRESENTATION FORMAT IS DESCRIBED IN FIGURE 7.

5% O <sub>2</sub> / 95% N <sub>2</sub>	22.3% O <sub>2</sub> / 77.7% N <sub>2</sub>	40% O <sub>2</sub> / 60% N <sub>2</sub>
 <p>R77 (3.86)</p>	 <p>R89 (3.78)</p>	 <p>R83 (3.84)</p>
 <p>R91 (3.50)</p>	 <p>R88 (3.65)</p>	 <p>R87 (3.56)</p>
 <p>R78 (3.37)</p>	 <p>R90 (3.36)</p>	

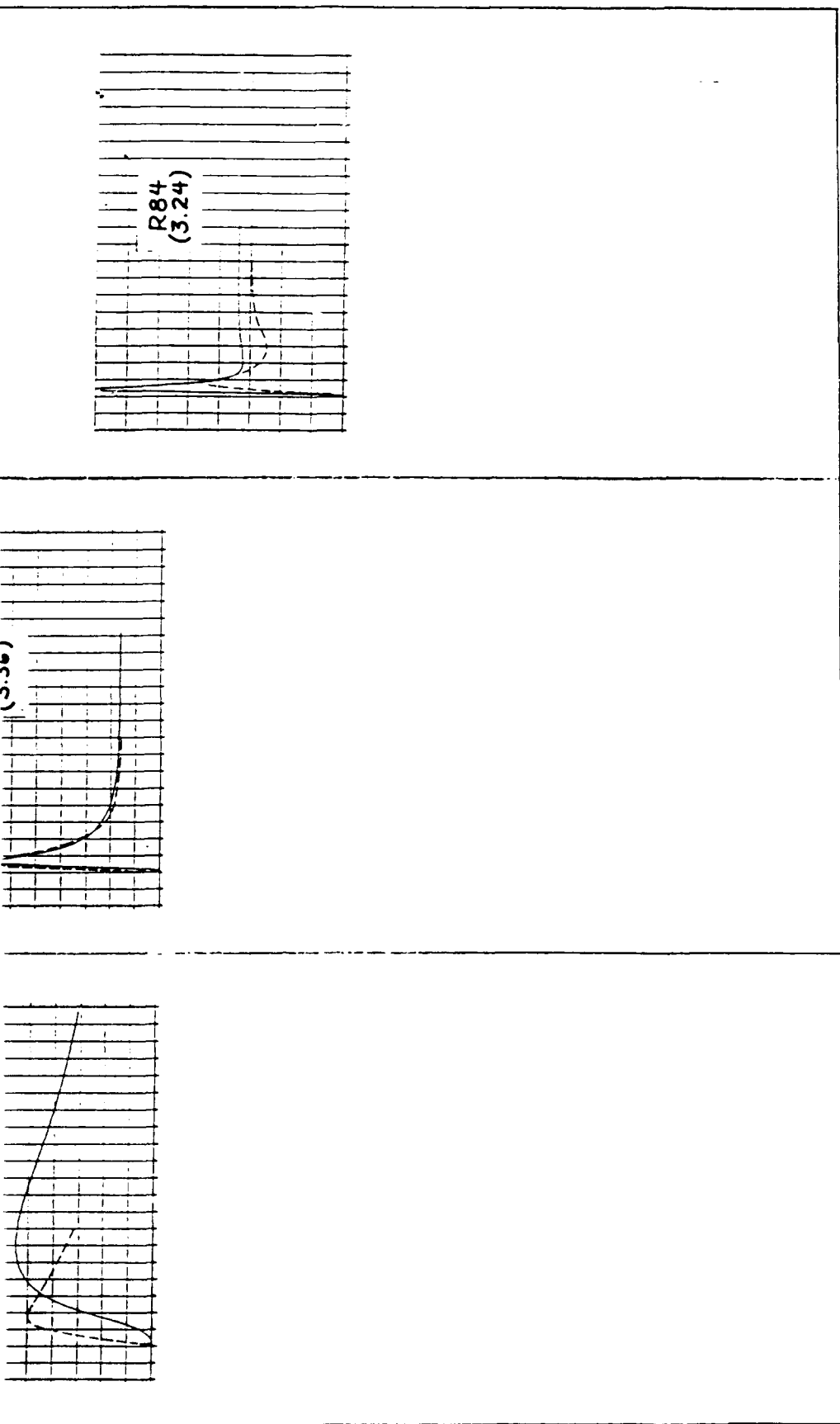


FIGURE 14. MATRIX OF MEASURED AND CALCULATED 230NM RADIANCE PROFILES. THE CALCULATED PROFILES (DASHED LINES) USE THE ELECTRONIC EXCITATION RATES GIVEN IN TABLE 5 AND THE CALCULATED GROUND STATE PROFILES SHOWN IN FIGURE 13. FULL-SCALE DATA RECORDS ARE GIVEN IN APPENDIX E.



APPENDIX A

**AIAA-89-1918**

**Nonequilibrium UV Radiation and Kinetics  
Behind Shock Waves in Air**

W.H. Wurster, C.E. Treanor and M.J. Williams  
Calspan-UB Research Center,  
Buffalo, NY

**AIAA 20th Fluid Dynamics, Plasma Dynamics  
and Lasers Conference**

Buffalo, New York / June 12-14, 1989

# NONEQUILIBRIUM UV RADIATION AND KINETICS BEHIND SHOCK WAVES IN AIR\*

W.H. Wurster\*, C.E. Treanor\*\*, and M.J. Williams\*\*\*  
Calspan-UB Research Center  
Buffalo, New York

## Abstract

An experimental study is described whose objectives include the quantitative measurement of the ultraviolet radiation behind strong shock waves in air, the identification of the radiating species and the determination of the mechanisms and rates that govern the emission. A shock tube was used to generate 3-4 km/s shock waves through air and  $O_2$ - $N_2$  mixtures at initial pressures between 0.36-2.25 torr. The temporal gas-radiance profiles recorded radiometrically exhibited strong non-equilibrium overshoots, followed by decay to steady-state equilibrium. The dependence of the peak overshoot values on wave speed and pressure was measured and shown to scale with density. Emission spectra of the gas both in the overshoot region and the equilibrium region showed the NO gamma band system between 210 and 340 nm to be the dominant radiation source. The role of  $O_2$  Schumann-Runge radiation in this region was also studied; in pure  $O_2$  no overshoot was recorded. Profiles of the measured air radiation have been compared with computed profiles based on translational and vibrational temperatures, and are shown to be bracketed by these. Infrared vibronic emission profiles were also measured and shown to be a description of the NO concentration growth. Further kinetic studies are presently ongoing.

## 1. Introduction

The motivation for this research centers upon the capability to predict the ultraviolet radiation from the bow shock of an ascending flight vehicle at velocities between 3-4 km/s at altitudes between 40-60 km. It is well known that the strongly heated air behind the bow shock of a body moving at hypersonic velocity can give rise to high radiative heating rates and to significant radiative signatures. These effects are particularly important to various aspects of reentry aerodynamics, and much of present understanding is a result of intense theoretical and experimental efforts in this area that were undertaken during the late 50's and early 60's. The significance of each effect varies with altitude, velocity and body configuration, and the capability to predict these effects by computational modeling has been an ongoing challenge, both in terms of the physical-chemical model and in the availability of data for input parameters and for comparison with predictions. The major objective of this study was to provide experimental data that directly supports predictive computational modeling efforts relating to non-equilibrium, bow-shock radiation.

The non-equilibrium aspect of the radiative signature arises from the fact that at higher altitudes the decreased density and collision frequency of molecules behind the shock front slows both the chemical reactions that establish species concentrations and those

that govern equipartition among internal energy states: electronic, vibrational and rotational. Thus, under some conditions there exist strong gradients behind the shock front, consisting of species concentrations and excited state populations far from equilibrium with the local (and changing) translational temperature. To describe this non-equilibrium and to predict its dependence on velocity and altitude requires that the relevant kinetic rates and mechanisms be known. It is to those that relate to ultraviolet and visible radiation that this investigation is primarily directed.

In the more recent past, consideration of vehicles such as the aeroassisted and aerobraked Orbital Transfer Vehicles led to computer code developments that address flow field predictions at higher altitudes and velocities (10 km/s)<sup>1-3</sup>. Their application to the lower velocities and altitudes of interest to the present problem is not clear, owing to the widely different kinetic chemistry involved. The need for an experimental data base over the relevant velocity-altitude range constitutes the major objective of these studies.

The most noteworthy and interesting difference between early shock tube studies and those reported herein lies in the newer instrumentation available today. Most especially useful were a multi-channel, high-speed digital data recording system, and an optical multichannel analyzer. This electronic spectrometer permitted short, precisely synchronized exposures to be made with good wavelength resolution.

The shock tube and the instrumentation is briefly described below. Typical data and their calibration are presented, together with a subsequent discussion of results.

## 2. Experimental

### Shock Tube

The shock tube employed in this research was used in a number of radiation and chemical kinetic studies over several decades.<sup>4-7</sup>

A schematic diagram of the overall experiment is shown in Figure 1. The steel driven section is 30 feet long, 3-inch inside diameter. The driver section is 5 feet long, and was originally designed for operation at 15,000 psi using pure hydrogen as the driver gas. To date on this program a maximum of 4,000 psi was used; most tests only required 1,000 psi of  $H_2$ , achieved by means of press-scribed, 0.035-inch-thick steel diaphragms. The routine double-diaphragm technique<sup>1</sup> provided excellent run-to-run reproducibility in wave speed ( $\sim 1\%$ ) and radiation records.

- \* Supported by SDIO-IST and managed by the Army Research Office
- \* Staff Scientist, AIAA Senior Member
- \*\* Director, CUBRC and AIAA Fellow
- \*\*\* Research Scientist



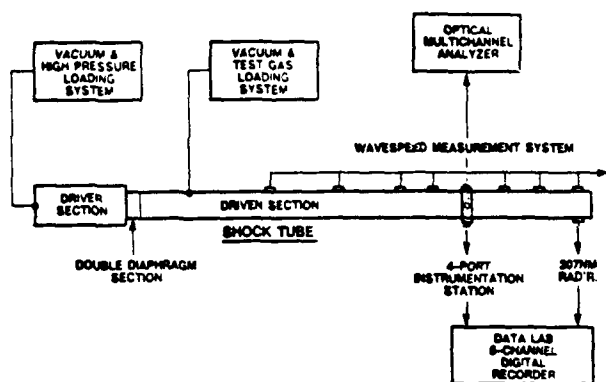


Fig. 1 Principal elements of the experiment.

Vacuum levels achieved using diffusion pumps with cryogenically cooled traps were routinely in the  $10^{-5}$  torr range with negligible leak/outgassing rates over the 15 minute pre-test gas loading interval. Initial test gas pressures were measured to better than 1% with an MKS Baratron unit. Scientific grade (99.999%)  $O_2$  and  $N_2$  were used throughout, with  $H_2O$  and  $CO_2$  at less than 1 ppm. After each test the tube was scrubbed with alcohol.

Thin-film heat transfer gauges were used to record shock arrival at seven sections along the tube. These signals were differentiated and combined for digital recording. This record then provided a common time line for all subsequent measurements, as discussed in the following section.

#### Instrumentation

An instrumentation station with four ports was located about six feet from the end of the shock tube. Figure 2 illustrates the four measurements that were made at that station for the test results reported in this paper. The primary quantitative measurements were made using a radiometer comprising a UV-quartz window, a 1P28 photomultiplier tube, an interference filter (260 nm, 10 nm FWHM, 15% transmission) and two slits to define the optical beam to 3 mm maximum width. These optical parameters were selected after a number of exploratory tests were made to establish spectral purity, and to assess signal strengths and spatial and temporal radiance gradients. This radiometer was calibrated by using an Optronics standard irradiance deuterium arc lamp, NBS traceable. In the calibration setup, a rotating mirror of known reflectance provided a dynamic lamp scan using the same time constant and slit-PMT cathode configuration as in the experiment. Calibrations slightly overlapping the range of signal levels of the experiment were made, but were limited by low lamp signals through the narrow bandpass filter. Linearity of output over the entire range was confirmed by using the detector unfiltered in an inverse-square/distance set of measurements.

An optical multichannel analyzer (EG & G/PARC OMA 3) was also deployed as shown. Its main function was to provide emission spectra throughout the UV and visible wavelength range, primarily to assess the spectrochemical purity in the shock tube test gas, and to verify the origin of the radiation recorded by the radiometers. This instrument proved to be highly effective; its operational feature of precise electronic shuttering

permitted spectra of both equilibrium and nonequilibrium air radiation to be obtained. This instrument was not calibrated absolutely, although the overall responsivity as a function of wavelength was measured and taken into account for each grating.

A HgCdTe detector-filter radiometer was also deployed to measure the NO fundamental vibronic band at 5  $\mu m$ , to obtain data relevant to the NO vibrational kinetics. The infrared signal-to-noise ratios were low, but adequate radiance profiles were obtained and will be discussed later.

An uncalibrated, wider bandpass, 1 mm-wide-beam radiometer at 250 nm provided redundant, primarily housekeeping, data.

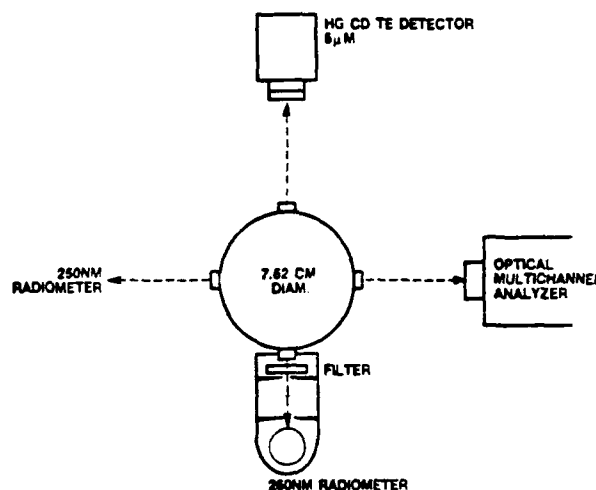


Fig. 2 Instrumentation at the measurement station.

Finally, it should be noted that another radiometer was deployed at a more downstream station in the shock tube. Its filter at 307 nm was selected to monitor the  $(0, 0)$  transition of the OH (A-X) band system. Its purpose was to monitor shock tube performance by recording the passage of the reacting  $H_2$ -driver/air driven gas interface. It thereby confirms the length (or duration) of the shock-processed test gas "slug", which ranged from 40-100 microseconds.

The OMA was a completely self-contained system; a computer was used for synchronization, exposure control timing, data recording and processing. All radiometer signals and the wavespeed data were fed to a datalab, 8-channel digital recorder with a 2 MHz sampling rate. This arrangement permitted all shock tube test data to be correlated to within 0.5 microsecond resolution; they included the radiometer outputs at two gain settings, the wavespeed time-of-arrival pulses, and a signal from the OMA that permitted the exact exposure time-interval of the spectrometer to be recorded.

#### 3. Typical Data

This section will illustrate the nature of the various data derived from the experiment, the techniques used for data reduction and calibration, and how the records have been interpreted.

The wave speed data format comprises a series of spikes that corresponds to shock arrival along about half the shock tube length. The intervals between spikes could be measured to 0.5 microseconds, from which a plot like Figure 3 was generated for each run. A second-order curve was then fitted to the data, and its slope at the measurement station was taken as the shock wave velocity for the test. The inputs for all shocked-gas property calculations were the initial test-gas pressure, the shock velocity and the ambient temperature.

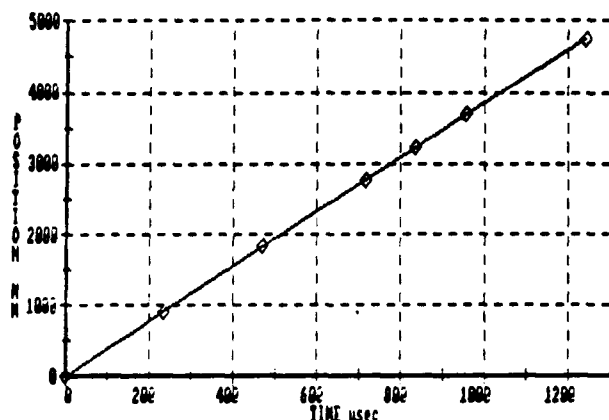


Fig. 3 Reduced wave speed data. Measurement station at 2843 mm.

In Figure 4 are shown very careful tracings of the raw-data radiance profiles obtained with the 260 nm radiometer for two tests in air at the cited conditions. For all conditions of interest, the overall profiles were similar, namely, a strong, rapidly rising overshoot region, followed by a decay to a steady-state equilibrium. The features of interest are the time-to-peak, peak signal levels, the decay rate, and the signal levels at equilibrium.

As will be shown below, this overshoot is dominated by 200-320 nm emission from the gamma band system of NO. The NO begins to form at the onset of O<sub>2</sub> dissociation behind the shock front. Rapid NO electronic excitation takes place, owing to the high translational temperature immediately behind the shock front. This temperature decays rapidly, as it is primarily dominated by the O<sub>2</sub> dissociation rate. Thus, the electronic excited state population is determined by a number of competing and coupled kinetic processes, whose result is the measured observables in Figure 4. The chemical kinetic mechanisms and rates involved constitute a major objective of this research.

One approach to this objective is to measure the overshoot profiles over a broad range of N<sub>2</sub>/O<sub>2</sub> mixture ratios, pressures and temperatures. One example is presented in Figure 5, in which pure O<sub>2</sub> was used as the test gas. In this case the radiation was shown to arise from the Schumann-Runge band system of O<sub>2</sub>. The striking difference in this profile is the lack of any overshoot. This feature of O<sub>2</sub> is well understood<sup>8</sup>. It results from a dominating radiationless depopulation path of the excited state to atoms; and the atom density increases monotonically, without an overshoot. This feature is significant in the kinetics of the overshoot. If the same O<sub>2</sub> kinetics prevail in air, then the role of O<sub>2</sub> in the overshoot will be limited by its value in the equilibrium region of the profile of Figure 4.

Typical 5  $\mu$ m infrared profiles are shown in Figure 6. Three profiles were superimposed; all are at initial air pressures of 2.25 torr, with shock velocities at 3.22, 3.50 and 3.83 mm/ $\mu$ s. Despite the much lower SNR, the comparisons show a definite trend of overshoot behavior. The interpretation and role of the overshoot is addressed in Section 4.

The OMA has proven to be invaluable to this study by providing emission spectra of the shock-heated gases. Initially, broad wavelength coverage spectra were taken to identify the dominant radiating species/bands, and to assess overall system purity levels.

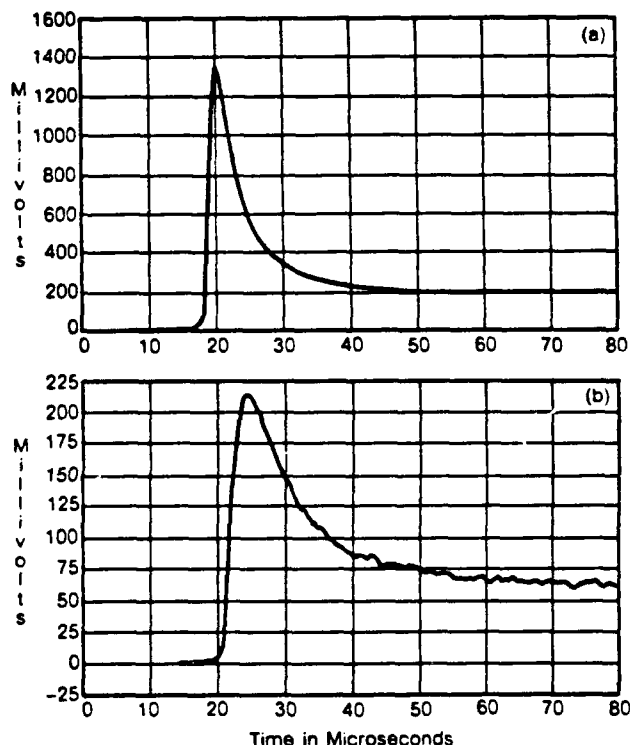


Fig. 4 260 nm radiance profiles in air. (a) Initial pressure: 2.25 torr, shock velocity: 3.81 mm/ $\mu$ s, (b) 2.25 torr, 3.50 mm/ $\mu$ s.

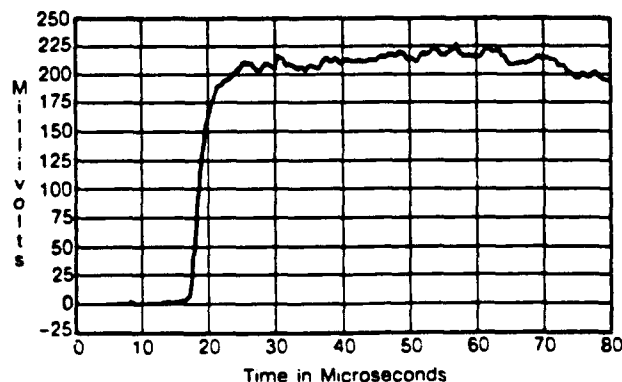


Fig. 5 Typical 260 nm radiance profile in oxygen. Initial pressure: 2 torr, shock velocity: 3.89 mm/ $\mu$ s.

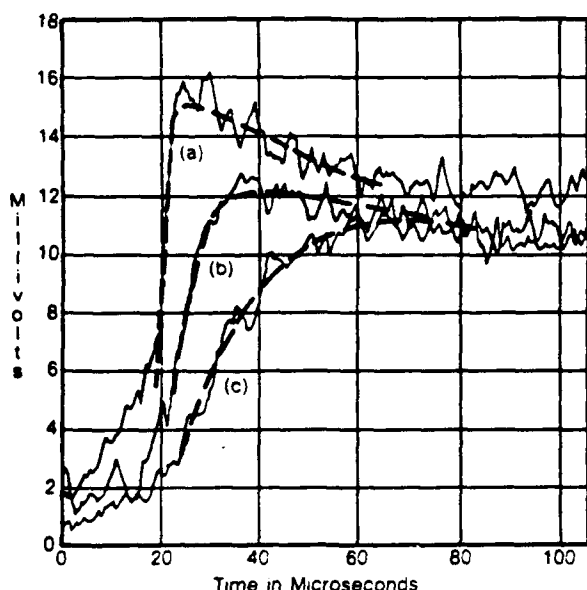


Fig. 6 Selected  $5\mu\text{m}$  radiation profiles illustrating the dependence on shock velocity. Initial air pressures: 2.25 torr; velocities in  $\text{mm}/\mu\text{s}$ : (a) 3.83, (b) 3.50, (c) 3.22.

Primary concern of spectral priority is the verification that the quantitative signals measured by the radiometers are indeed from the species of interest. A typical low-resolution spectrum of shock-heated air is shown in Figure 7. In this case the spectrum was integrated over 30  $\mu\text{s}$  during the equilibrium portion of a profile such as in Figure 4(a), between 50–80  $\mu\text{s}$ . For the profile plots, time  $t = 0$  is measured from a time-of-arrival gauge located 73 mm ahead of the 4-port instrumentation section centerline.

The recorded spectrum clearly shows the band structure of the NO gamma band system in both the first and second order of the grating. No hydrocarbon impurity bands are in evidence. To date, only the ubiquitous Na D line and the 306.4 nm band of the OH (0, 0) A-X have been seen. The origin of the OH has not been pursued; it is of variable signal strength, and felt to arise from  $\text{H}_2\text{O}$  on the walls of the tube. We note that with hydrogen driven gas, combustion at the interface occurs in every test. Fortunately, unambiguous, quantitative radiometer measurements at wavelengths below 280 nm can be made despite the trace OH presence. To date, its role in kinetics or energetics has been ignored.

The presence of  $\text{O}_2$  radiation in the spectrum of Figure 7 is clearly overwhelmed by the NO system. A spectrum of shock-heated  $\text{O}_2$  at higher resolution is shown in Figure 8. As can be seen, the spectrum below 300 nm is fairly featureless, being made up of many overlapping bands. Identification of several most obvious bands is given at longer wavelengths. The spectra of Figures 7 and 8 can be compared with the computed spectra of Figures 12 and 13.

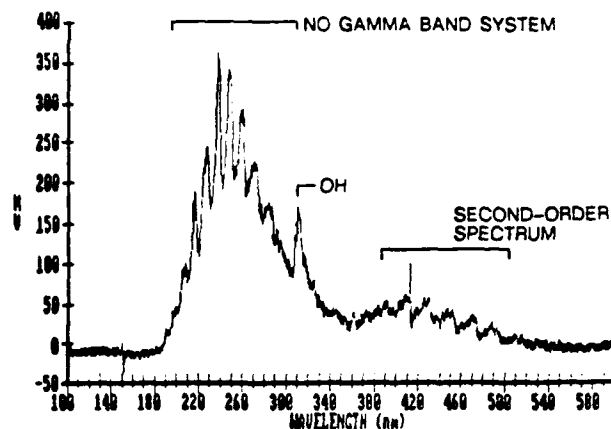


Fig. 7 Typical low-resolution spectrum of shock-heated air in equilibrium at  $3800^\circ\text{K}$ .

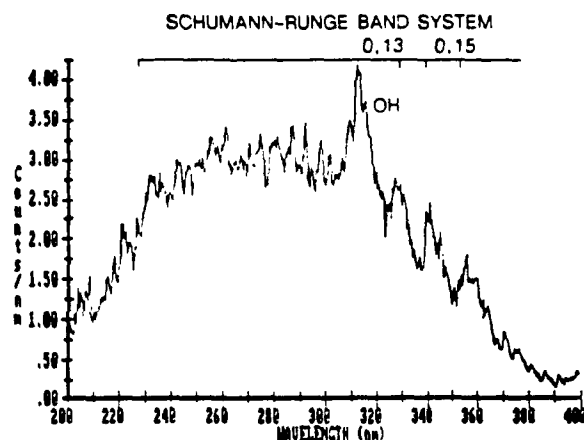


Fig. 8 High resolution spectrum of oxygen in equilibrium at  $3380^\circ\text{K}$ .

#### 4. Results

##### Nonequilibrium Radiation

##### Velocity-Altitude Scaling

The nonequilibrium radiation from the shock-heated gas was measured for a number of shock velocities at each of three initial shock-tube pressure. The initial air pressures of 2.25, 0.66 and 0.36 torr were chosen to correspond to flight altitudes of 40, 50, and 55 km. Lower pressures were avoided on the usual grounds of difficulties with boundary layers, shock curvature, etc.

When the correspondence between the nonequilibrium zone behind the shock wave in the tube and that behind a blunt-body bow shock is examined,<sup>9,10</sup> it can be seen that the peak overshoot value is the most critical factor in determining the radiation from the gas cap. The region of the decay to equilibrium and the equilibrium radiance are compressed, lie close to the body, and are contained in the boundary layer.

The results of some 20 runs are plotted in Figure 9, in which the peak overshoot radiance values were analyzed by the densities at the altitudes shown. The direct scaling with density is readily apparent, as is the factor of 100 in intensity over the velocity range shown. To obtain the absolute radiance units, the signals from the radiometer were directly ratioed to those from the known D<sub>2</sub> standard lamp, with account taken of the shock tube diameter and the optical throughput (area x steradian) of the radiometer. It should be mentioned that the measurements shown are in-band, corresponding to the 260 nm filter. In order to extrapolate these data to other wavelength intervals, the relevant spectra of NO and O<sub>2</sub> at the conditions of interest would need to be considered. For this purpose the spectra derived with the ONA were particularly significant.

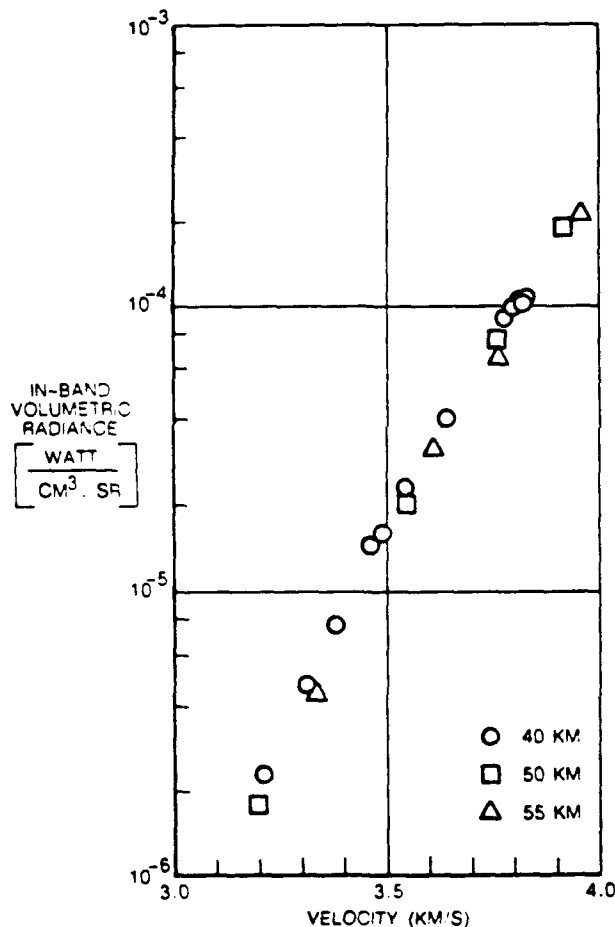


Fig. 9 Velocity and altitude dependence of the peak overshoot value of the in-band volumetric air radiance. Data normalized by density ratios.

#### Electronic State Kinetics

The ultimate goal of the kinetics studies, both theoretical and experimental, is to determine the mechanisms and rates for the population of the excited NO(A) state. Except for the case of NO(A) formation directly from N and O atoms, the most likely other mechanisms involve collisions with the NO molecules being formed behind the shockfront. The computational approach taken to data is to use a kinetic code to

calculate the formation of the ground state chemical species first. This implies that excited electronic state kinetics can be decoupled. This convenience then permits separate interactions on these mechanisms and rates, without recalculation of all species concentrations.

The first step has been achieved by making use of an updated version of Calspan's Kinetic Normal Shock (KNS) code,<sup>11</sup> redesigned to run on an IBM PC AT. It computes the thermal and chemical relaxation of mixtures of reacting gases behind normal shock waves. The menu-driven program enables the user to produce a convenient listing of selected parameters versus particle time and distance on a file for printing and generate plot files which may be viewed on the screen and/or routed to a printer.

Table 1 presents a listing of the 11 reactions and the rates used for the computations for air.

Table 1  
REACTION RATE COEFFICIENTS

NO	Reaction	Rate Coefficient	Units
1	$O_2 + O \xrightleftharpoons{k_f} 2O + O$	$k_f = 2.1 \times 10^{-11} (T)^{-1.5} \exp(-\frac{5930}{T})$	cm <sup>3</sup> /mole-sec
2	$O_2 + O_2 \xrightleftharpoons{k_f} 2O + O_2$	$k_f = 3.6 \times 10^{-11} (T)^{-1.5} \exp(-\frac{5930}{T})$	cm <sup>3</sup> /mole-sec
3	$O_2 + M \xrightleftharpoons{k_f} 2O + M$	$k_f = 1.19 \times 10^{-11} (T)^{-1.5} \exp(-\frac{5930}{T})$	cm <sup>3</sup> /mole-sec
4	$N_2 + N \xrightleftharpoons{k_f} 2N + N$	$k_f = 7.5 \times 10^{-11} (T)^{-1.5}$	cm <sup>3</sup> /mole-sec
5	$N_2 + N_2 \xrightleftharpoons{k_f} 2N + N_2$	$k_f = 1.5 \times 10^{-11} (T)^{-1.5}$	cm <sup>3</sup> /mole-sec
6	$N_2 + M \xrightleftharpoons{k_f} 2N + M$	$k_f = 5 \times 10^{-12} (T)^{-1.5}$	cm <sup>3</sup> /mole-sec
7	$NO + M \xrightleftharpoons{k_f} N + O + M$	$k_f = 5.18 \times 10^{-11} (T)^{-1.5} \exp(-\frac{7841}{T})$	cm <sup>3</sup> /mole-sec
8	$N + O_2 \xrightleftharpoons{k_f} NO + O$	$k_f = 1 \times 10^{-12} (T)^{0.5} \exp(-\frac{312}{T})$	cm <sup>3</sup> /mole-sec
9	$O + N_2 \xrightleftharpoons{k_f} NO + N$	$k_f = 5 \times 10^{-14} \exp(-\frac{32}{T})$	cm <sup>3</sup> /mole-sec
10	$N + O \xrightleftharpoons{k_f} NO + \text{e}$	$k_f = 5.4 \times 10^{-11} (T)^{-1.5}$	cm <sup>3</sup> /mole-sec
11	$N_2 + O_2 \xrightleftharpoons{k_f} 2NO$	$k_f = 9.1 \times 10^{-14} (T)^{-2.5} \exp(-\frac{8520}{T})$	cm <sup>3</sup> /mole-sec

An example of some results obtained with these reaction rates is shown in Figure 10. Separately shown are the translational and N<sub>2</sub> vibrational temperatures, and the NO and O<sub>2</sub> concentrations behind the shock front. In Figure 11 the computed excited (A) state population of NO is plotted, assuming local equilibrium with each of the temperatures. For clarity in comparing the temporal features of the overshoots, the data were normalized to unity peak values. Also shown is the normalized radiometer record for the same conditions. It can be seen that the excitation rate is characterized by a temperature intermediate to those shown.

Further efforts are presently underway to obtain similar data over a broad range of O<sub>2</sub>/N<sub>2</sub> mixture ratios, and to use this extended data base in formulating the operant mechanisms and rates that determine the radiative overshoot profiles.

#### Infrared Vibrational Kinetics

The infrared radiation of NO in air has been measured for a series of shock speeds and for an initial shock-tube pressure of 2.25 torr. The emission results are shown in Figure 6 for three experiments spanning this range. The spatial resolution of the optical system is about 5 mm, or on the scale shown in Figure 6, about 1.4 usec. Vibrational relaxation times for NO (in Argon) range from 30 to 40 usec<sup>12,13</sup> (particle time) under these conditions of temperature and pressure, and are probably considerably shorter in air (they are 50 times shorter in pure NO<sup>12,13</sup>). The laboratory time (the parameter used in Figure 6) is shorter than the particle time by a factor

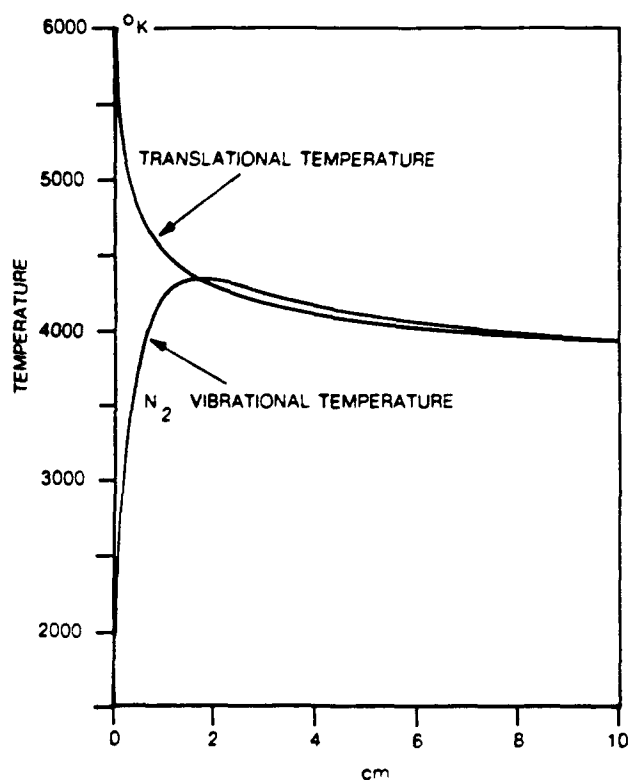


Fig. 10 Direct output plots of the computed temperature and species concentration gradients behind the shock front. Velocity: 3.84 Km/s; initial air pressure: 2.25 torr.

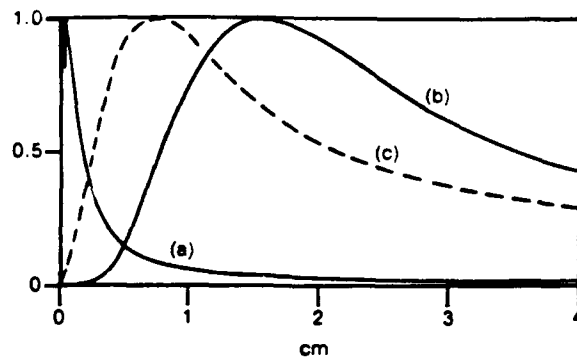


Fig. 11 Normalized NO (A) state population profiles in local equilibrium at (a) translational temperature (b)  $N_2$  vibrational temperature (c) 260 nm radiometer measured profile. Same test conditions as for Fig. 10.

equal to the density ratio across the shock, which is between 6 and 10 for these experiments. Thus, the vibrational relaxation time of NO is of the order of several microseconds in laboratory time. The observed intensity is then proportional to the amount of NO present and to a weak function of the vibrational temperature of the NO. For practical purposes the position of the intensity maximum would be expected to occur close to the maximum value of the NO concentration. The measured times to maximum are in fact longer than those calculated with the standard 11-reaction model given in Table 1. The calculated NO maxima occur at 1.9  $\mu$ sec, 7.8  $\mu$ sec and 36.5  $\mu$ sec for the experiments shown in Figure 6, compared with experimental values of about 8  $\mu$ sec, 22  $\mu$ sec and 48  $\mu$ sec. One explanation would be a slower-than-expected relaxation of NO vibration. The slow decay of NO concentration at times after the maximum is reached would account for the final decay of the radiation.

#### Equilibrium Radiation

##### NO and $O_2$ f Values

The time-dependent measurements of the radiation at 260 nm, as shown in Figure 4, can be used to obtain an equilibrium radiation value at long times, and these can be compared with previous equilibrium experiments by evaluation of the optical f values of the radiating systems. The experimental data were reduced by using a numerical calculation which approximates the spectral distribution by replacing the actual vibrational-rotational structure with a simple smoothed Q-branch structure (see Figures 12 and 13)<sup>14</sup>, and performing a numerical integral of the intensity multiplied by the filter function. If the calculation is performed for  $O_2$  and NO, using f values of unity and number densities of unity for each species, reference values for the in-band radiation,  $I_{O_2}^0$  and  $I_{NO}^0$ , are obtained. The in-band radiation to be expected from air would then be

$$I_{air} = n_{O_2} f_{O_2} I_{O_2}^0 + n_{NO} f_{NO} I_{NO}^0$$

$$\text{or} \quad \frac{I_{air}}{n_{O_2} I_{O_2}^0} = f_{O_2} + f_{NO} \cdot \left( \frac{n_{NO}}{n_{O_2}} \cdot \frac{I_{NO}^0}{I_{O_2}^0} \right)$$

Since  $I_{NO}^0$  and  $I_{O_2}^0$  are known from the calculation, and  $n_{NO}$  and  $n_{O_2}$  are known from the equilibrium shock calculation, the experimental value of  $I_{air}$  divided by  $n_{O_2} I_{O_2}^0$  can be plotted vs  $n_{NO} I_{NO}^0 / n_{O_2} I_{O_2}^0$ . The intercept and slope of the straight line yield the f-values

of  $O_2$  and  $NO$ . The values obtained from eleven experiments in  $O_2$  and air are  $f_{O_2} = 0.052$  and  $f_{NO} = 0.0091$  at a wavelength of 260 nm, as shown in Figure 14. The value for  $O_2$  is somewhat lower than that suggested by Keck et al.<sup>15</sup> (0.075) or by Krindach et al.<sup>16</sup> (0.09) for this wavelength. The  $NO$  value is consistent with the values given by Schadee<sup>17</sup>.

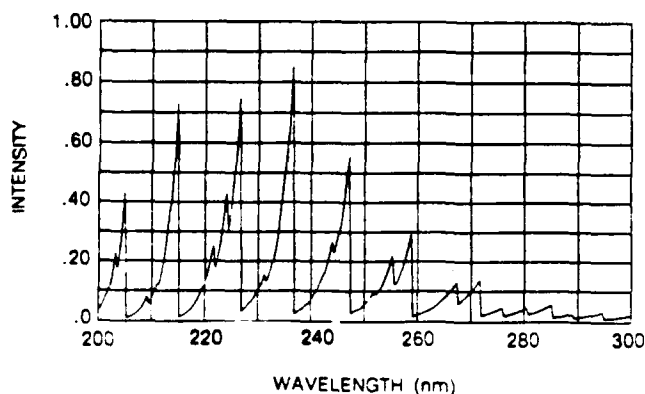


Fig. 12 Nitric oxide gamma band system (4000K)

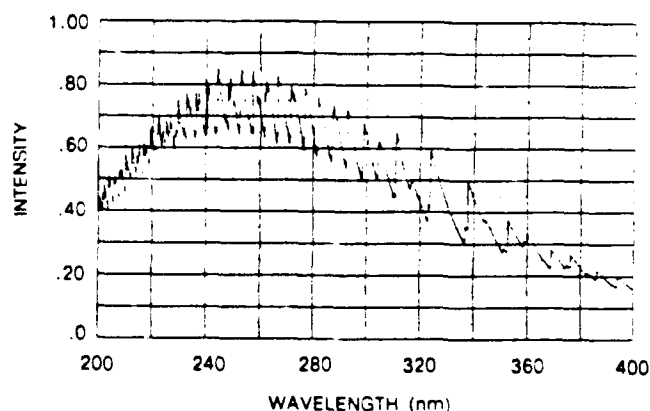


Fig. 13 Oxygen Schumann-Runge band system (3383K)

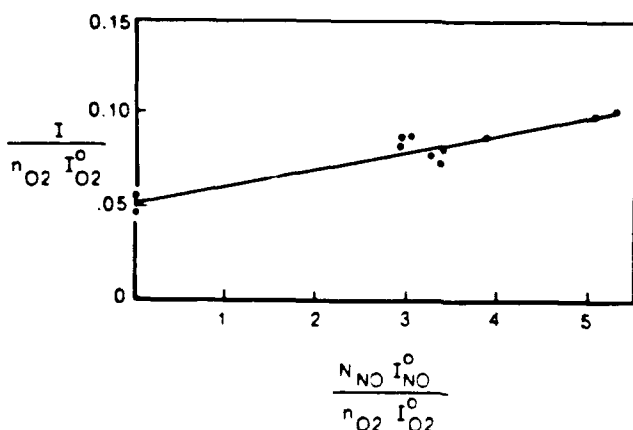


Fig. 14 Intensity measurements in oxygen and in air.

## References

1. Park, C., Calculation of Nonequilibrium Radiation in the Flight Regimes of Aeronautical Orbital Transfer Vehicles, Paper 84-0306 at AIAA 22nd Aerospace Sciences Mtg., Reno, Jan. 1984.
2. Park, C., Problems of Rate Chemistry in the Flight Regimes of Aeroassisted Orbital Transfer Vehicles, Paper 84-1730 at AIAA 19th Thermophysics Conference, Snowmass Colo., June 1984.
3. Candler, G. and MacCormack, R., The Computations of Hypersonic Ionized Flows in Chemical and Thermal Nonequilibrium Paper 88-0511 at AIAA Aerospace Sciences Mtg., Reno, Jan. 1988.
4. Wurster, W.H., Measured Transition Probability for the First-Positive Band System of Nitrogen, J. Chem. Phys. **36**, April 1962.
5. Marrone, P.V. and Wurster, W.H., Measurement of Atomic N and C Using Shock Tube VUV Spectrometry, JQSRT **11** 327 1971.
6. Rothe, D.E., Radiative Ion-Electron Recombination J. Quant. Spectros. JQSRT **9**, 49, 1969.
7. Boyer, D.W., Rate Coefficient Determinations of Important Reactions Involving  $HBO_2$  and  $OBf$ , AFRPL TR-83-045, March 1984.
8. Herzberg, G., Spectra of Diatomic Molecules, D. Van Nostrand Co., Princeton, N.J., 1955.
9. Gibson, W.E. and Marrone, P.V., "A Correspondence Between Normal Shock and Blunt-Body Flows" CAL QM-1626-A-7, June 1962.
10. Park, C., Assessment of a Two Temperature Kinetic Model for Ionizing Air, AIAA Paper 87-1574, Hawaii, 1987.
11. Marrone, P.V., et al., Inviscid, Nonequilibrium Flow Behind Bow and Normal Shock Waves, Cornell Aeronautical Laboratory Report No. QM-1626-A-12 (I-III) May 1963, October 1966.
12. Wray, Kurt L. A Shock Tube Study of the Vibrational Relaxation of Nitric Oxide, J. Chem Phys **36** 2597 (1962).
13. Kamimoto, Goro and Matsui, Hiroyuki, Vibration Relaxation of Nitric Oxide in Argon, J. Chem Phys **53** 3987 (1970).
14. Treanor, C.E. and Williams, M.J. A Method for Calculating Diatomic Spectra Using a Digital Computer CAL Report QM1626-A-5, 1962.
15. Keck, J.C., Allen, R.A. and Taylor, R.L. "Electronic Transition Moments for Air Molecules", JQSRT **3**, 335 (1963).
16. Krindach, N.I., Sobolev, N.N., and Tunitskii, L.N. Determination of the Electronic Transition Moments for the Schumann-Runge Bands of  $O_2$ , Opt. Spectrosc. (Eng. trans.) **15**, 326 (1963).
17. Schadee, Aert. The Relation Between the Electronic Oscillator Strength and the Wavelength for Diatomic Molecules, JQSRT **7** 169 (1967).

## REPORT DOCUMENTATION PAGE

1a. REPORT SECURITY CLASSIFICATION Unclassified		1b. RESTRICTIVE MARKINGS	
2a. SECURITY CLASSIFICATION AUTHORITY		3. DISTRIBUTION/AVAILABILITY OF REPORT Approved for public release; distribution unlimited.	
2b. DECLASSIFICATION/DOWNGRADING SCHEDULE			
4. PERFORMING ORGANIZATION REPORT NUMBER(S)		5. MONITORING ORGANIZATION REPORT NUMBER(S)	
6a. NAME OF PERFORMING ORGANIZATION CALSPAN-UB Research Center	6b. OFFICE SYMBOL (if applicable)	7a. NAME OF MONITORING ORGANIZATION U. S. Army Research Office	
6c. ADDRESS (City, State, and ZIP Code) Box 400 Buffalo, N.Y. 14225		7b. ADDRESS (City, State, and ZIP Code) P. O. Box 12211 Research Triangle Park, NC 27709-2211	
8a. NAME OF FUNDING/SPONSORING ORGANIZATION U. S. Army Research Office	8b. OFFICE SYMBOL (if applicable)	9. PROCUREMENT INSTRUMENT IDENTIFICATION NUMBER	
8c. ADDRESS (City, State, and ZIP Code) P. O. Box 12211 Research Triangle Park, NC 27709-2211		10. SOURCE OF FUNDING NUMBERS PROGRAM ELEMENT NO. PROJECT NO. TASK NO. WORK UNIT ACCESSION NO.	
11. TITLE (Include Security Classification) Nonequilibrium UV Radiation and Kinetics behind shock waves in air			
12. PERSONAL AUTHOR(S) W.H. Wurster, C.E. Treanor and M.J. Williams			
13a. TYPE OF REPORT Reprint	13b. TIME COVERED FROM TO	14. DATE OF REPORT (Year, Month, Day)	15. PAGE COUNT
16. SUPPLEMENTARY NOTATION The view, opinions and/or findings contained in this report are those of the author(s) and should not be construed as an official Department of the Army position, policy, or decision, unless so designated by other documentation.			
17. COSATI CODES FIELD GROUP SUB-GROUP		18. SUBJECT TERMS (Continue on reverse if necessary and identify by block number) Radiation Shock-Heated Air Ultraviolet Nonequilibrium Air	
19. ABSTRACT (Continue on reverse if necessary and identify by block number) An experimental study is described whose objectives include the quantitative measurement of the ultraviolet radiation behind strong shock waves in air, the identification of the radiating species and the determination of the mechanisms and rates that govern the emission. A shock tube was used to generate 3-4km/s shock waves through air and O <sub>2</sub> -N <sub>2</sub> mixtures at initial pressures between 0.36-2.25 torr. The temporal gas-radiance profiles recorded radiometrically exhibited strong non-equilibrium overshoots, followed by decay to steady-state equilibrium. The dependence of the peak overshoot values on wave speed and pressure was measured and shown to scale with density. Emission spectra of the gas both in the overshoot region and the equilibrium region showed the NO gamma band system between 210 and 340 nm to be the dominant radiation source. The role of O <sub>2</sub> Schumann-Runge radiation in this region was also studied; in pure O <sub>2</sub> no overshoot was recorded. Profiles of the measured air radiation have been compared with computed profiles based on translational and vibrational temperatures, and are shown to be bracketted by these. Infrared vibronic emission profiles were also measured and shown to be a description of the NO concentration growth. (Over)			
20. DISTRIBUTION/AVAILABILITY OF ABSTRACT <input type="checkbox"/> UNCLASSIFIED/UNLIMITED <input type="checkbox"/> SAME AS RPT. <input type="checkbox"/> DTIC USERS		21. ABSTRACT SECURITY CLASSIFICATION Unclassified	
22a. NAME OF RESPONSIBLE INDIVIDUAL		22b. TELEPHONE (Include Area Code)	22c. OFFICE SYMBOL

UNCLASSIFIED

SECURITY CLASSIFICATION OF THIS PAGE

19. (cont.) Further kinetic studies are presently ongoing.

UNCLASSIFIED

SECURITY CLASSIFICATION OF THIS PAGE





**AIAA-90-1666**

**Kinetics of UV Production Behind Shock  
Waves in Air**

W. H. Wurster, C. E. Treanor and M. J. Williams  
Calspan-UB Research Center,  
Buffalo, NY

**AIAA 21st Fluid Dynamics, Plasma Dynamics  
and Lasers Conference**

June 18-20, 1990 / Seattle, WA

# KINETICS OF UV PRODUCTION BEHIND SHOCK WAVES IN AIR\*

W.H. Wurster\*, C.E. Treanor\*\*, and M.J. Williams\*\*\*  
Calspan-UB Research Center  
Buffalo, New York

## Abstract

In a series of shock-tube experiments, the time-dependent ultraviolet radiation behind the shock wave has been measured for various  $O_2/N_2$  mixtures and for a range of shock velocities from 3.24 to 3.86 mm/ $\mu$ sec. From the equilibrium portion of the experiments, the values of the squared transition moment for the  $O_2$  Schumann-Runge and the NO Gamma band systems were measured at 230 nm to be  $|R_e|_{SR}^2 = 1.5$  a.u. and  $|R_e|_{\gamma}^2 = 0.21$  a.u. For the nonequilibrium region directly behind the shock, calibrated time histories of NO Gamma radiation are presented. The kinetic mechanisms governing this nonequilibrium radiation have been investigated, but values for specific rate constants have not yet been determined. Concurrent infrared measurements which viewed the NO IR system at  $1850\text{ cm}^{-1}$  show agreement with calculated NO equilibrium values, but did not have the time resolution to follow the details of the nonequilibrium emission. Plans for improved instrumentation and further measurements are described.

## 1. Introduction

This paper describes the latest results of an ongoing research program whose motivation centers upon the capability to predict the ultraviolet radiation from the bow shock of a vehicle ascending between 40-60 km at velocities between 3-4 km/s. The objectives of the program include providing quantitative measurements in support of a sounding rocket flight experiment, the identification of the radiating species, and the dependence of the radiation on altitude and velocity. In addition, basic data are being acquired in support of modelling this nonequilibrium radiation.

The non-equilibrium aspect of the radiative signature arises from the fact that at higher altitudes the decreased density and collision frequency of molecules behind the shock front slows both the chemical reactions that establish species concentrations and those that govern equipartition among internal energy states: electronic, vibrational and rotational. Thus, under some conditions there exist

strong gradients behind the shock front, consisting of species concentrations and excited state populations far from equilibrium with the local (and changing) translational temperature. To describe this nonequilibrium and to predict its dependence on velocity and altitude requires that the relevant kinetic rates and mechanisms be known. It is to those that relate to ultraviolet and visible radiation that this investigation is primarily directed.

A description of the shock tube experiment and early results have been presented in Reference 1. They will be very briefly discussed below, for overall completeness. New instrumentation and an extension of the range of measurements are next described. They provide an extensive data base whose analysis is underway, with the goal of providing a model to describe the electronic state kinetics that govern the nonequilibrium ultraviolet radiation from shock-heated air. The results to date of these ongoing analyses are discussed, and present plans to complete the program are outlined.

## 2. Review of Previous Work

It is especially convenient that the flight conditions of interest, namely, shock velocities of 3-4 km/s at altitudes above 40 km (2.25 torr) can be exactly duplicated in a shock tube. Thus, the measurement of the radiation profile as the shock-heated air passes a given station can be readily and simultaneously achieved for a number of wavelengths and with different instruments. Further, it can be shown that a profile measured in the shock tube can be transformed to that behind the bow shock wave. The use of this "correspondence" then permits the direct use of the shock data to predict the radiation emanating from the bow shock.

Figure 1 depicts the major elements of the shock tube and instrumentation used in the experiments, and which are described in detail in Reference 1.

Basically, the radiation from the incident-shock-heated gas is viewed through four windows at the same station in the shock tube. Radiometers in the UV and IR provide temporally resolved profiles,

\* Supported by SDIO-IST and managed by the Army Research Office  
\* Staff Scientist, AIAA Senior Member  
\*\* CUBRC Consultant and AIAA Fellow  
\*\*\* Research Scientist

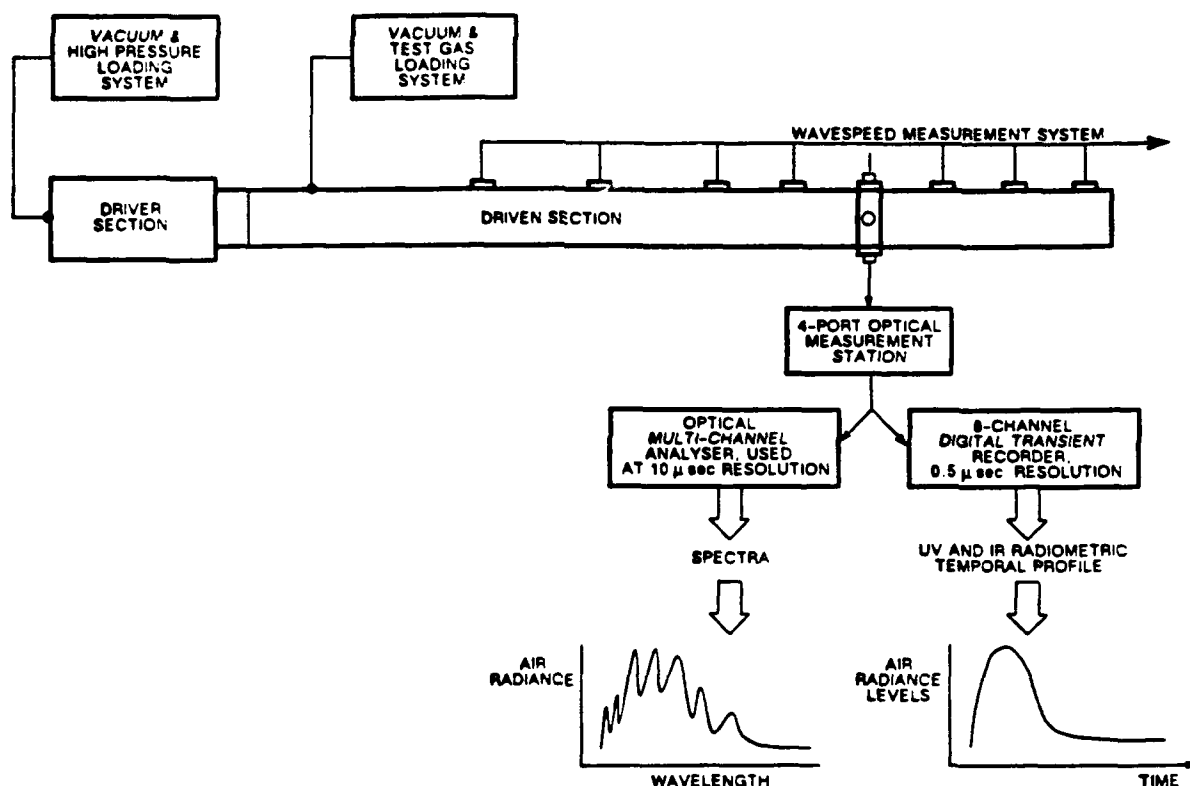


Fig. 1 Principal elements of the shock tube radiation experiment.

while the electronic spectrometer provides UV-visible spectra recorded over selected time intervals. Wave speed and radiometric data are simultaneously recorded and synchronized via a digital transient recorder.

Examples of typical radiation profiles obtained with a radiometer at 260 nm are presented in Figures 2(a) and 2(b), for the test conditions shown. For all conditions of interest, the overall profiles were similar, namely, a strong, rapidly rising overshoot region, followed by a decay to a steady-state equilibrium. The features of interest are the time-to-peak, peak signal levels, the decay rate, and the signal levels at equilibrium.

As will be shown below, this overshoot is dominated by 200–320 nm emission from the Gamma band system of NO. The NO begins to form at the onset of O<sub>2</sub> dissociation behind the shock front. Rapid NO electronic excitation takes place, owing to the high translational temperature immediately behind the shock front. This temperature decays rapidly, as it is primarily dominated by the O<sub>2</sub> dissociation rate. Thus, the electronic excited state population is determined by a number of competing and coupled kinetic processes, resulting in the meas-

ured observables in Figure 2. The chemical kinetic mechanisms and rates involved constitute a major objective of this research.

In contrast, tests in pure oxygen result in profiles such as that of Figure 2(c). This lack of overshoot is significant to these kinetic studies and will be addressed in detail in a later section.

As shown in Figure 1, an optical multichannel analyzer (OMA) was also deployed at a window at the same shock tube stations. This instrument could be gated to obtain spectra over selected time intervals behind the incident shock wave. Typical spectra are shown in Figure 3 where the results of a pure oxygen test are superimposed on that of air. The band structure of the NO Gamma system is clearly identified, and can be seen to override a base of O<sub>2</sub> Schumann-Runge bands.

By conducting a series of tests in air under various initial shock-tube pressures and shock velocities, the in-band, volumetric radiance of the peak radiation was quantitatively measured and the results reported in Reference 1. The peak intensity was found to scale directly with altitude and was shown to have a very strong velocity dependence.

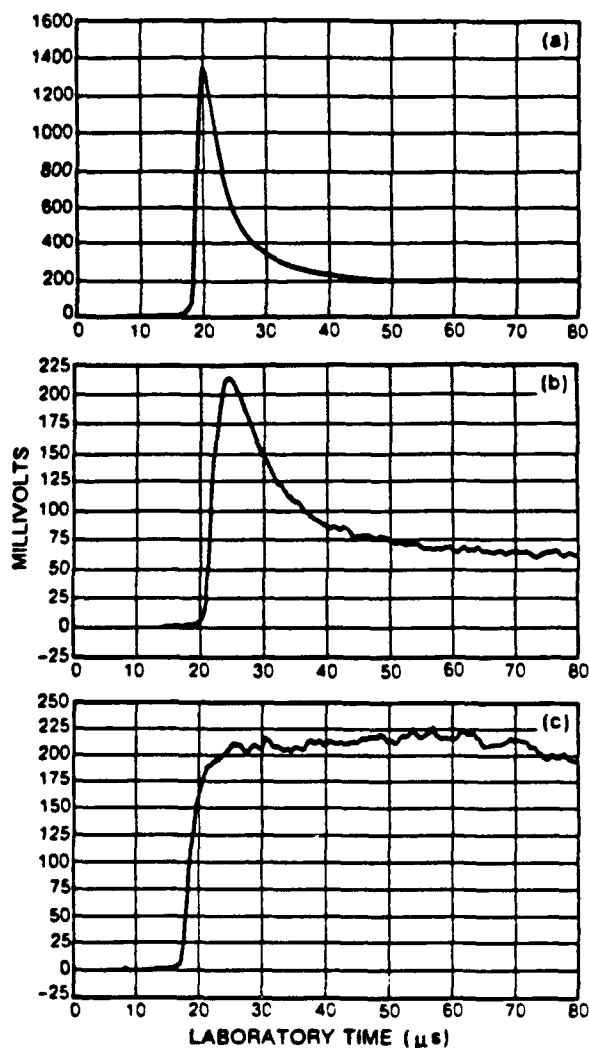


Fig. 2 Typical 260 nm radiance profiles.  
 (a) air, initial pressure: 2.25 torr,  
 shock velocity: 3.81 mm/ $\mu$ s;  
 (b) air, initial pressure: 2.25 torr,  
 shock velocity: 3.50 mm/ $\mu$ s;  
 (c) oxygen, initial pressure: 2 torr,  
 shock velocity: 3.89 mm/ $\mu$ s.

### 3. Present Experiments

The earlier measurements described above served to establish the identification of the species and bands contributing to the non-equilibrium ultraviolet radiation from shock-heated air, and to measure quantitatively the dependence of this radiation on altitude and shock velocity.<sup>1</sup> The goals of the recent studies primarily address the kinetic mechanisms and rates that populate the relevant electronic states and subsequently govern the radiation profile. These studies involved (a) the implementation of another ultraviolet radiometer with higher spatial resolution and with enhanced sensitivity, (b) a series of

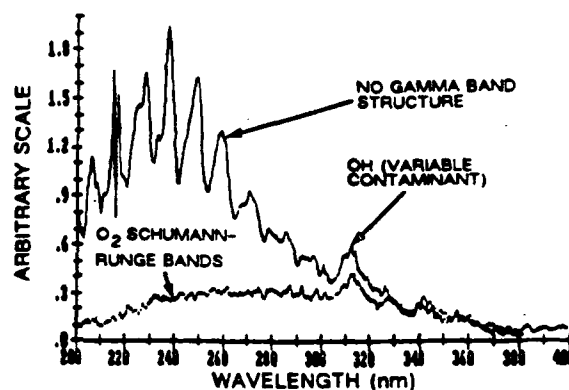


Fig. 3 Superimposed spectra of shock-heated air (upper trace) and pure oxygen. See Ref. 1 for details.

measurements in which the post-shock densities of NO and O<sub>2</sub> (and the concomitant temperature gradients) were varied over a broad range for an extended kinetic data set, (c) a final analysis of the equilibrium NO and O<sub>2</sub> radiation characteristics, and (d) the development of a computational electronic state excitation model, which, in conjunction with the kinetic data set, aims to provide a predictive capability for the non-equilibrium UV radiation. These program elements will be addressed in the balance of the paper.

#### The 230 nm Radiometer

As mentioned above, the design of this instrument sought to achieve higher spatial resolution of the field-of-view (FOV) across the shock tube, as well as enhanced sensitivity. The design components are illustrated in Figure 4. The uniform FOV across the tube is achieved by having the aperture stop and the image of the field stop equal, at 1 x 8 mm. At this 1 mm beam width, the 0.5 microsecond digital sampling time sets the overall ideal resolution of 2mm (at 4 mm/ $\mu$ s). Recent analyses have indicated that the overall resolution may be as low as 3-4 mm, which would be inadequate for high velocity, high-gradient shock radiation profiles and it is planned to establish this FOV in separate measurements.

Another effect is noted, whereby light from the advancing shock, when close to, but still outside, the FOV, can scatter (and produce signal) from any scratch or imperfection in the quartz window or lens, or from the razor-blade slit edges. This effect is manifested in the small pre-shock "foot" seen in most records.

Enhanced sensitivity was attained by having a larger optical throughput (cm<sup>2</sup>-sr) than before, and in using a wider UV filter to capture more of the

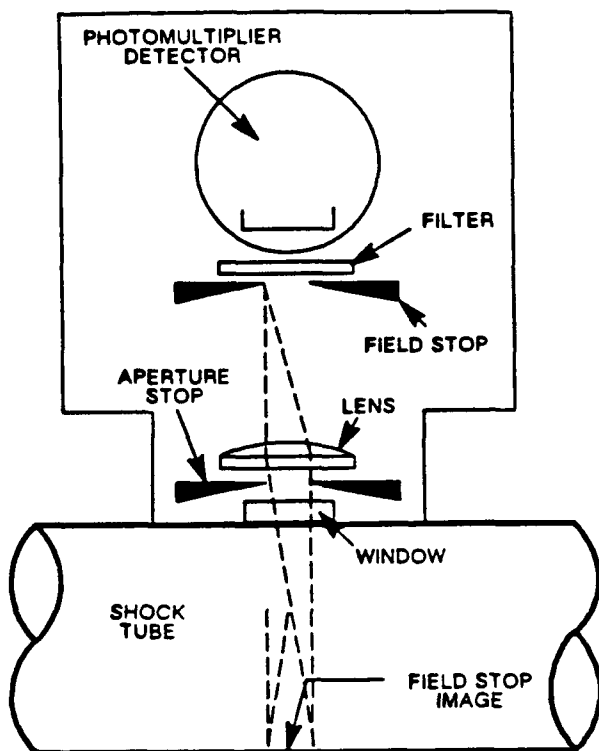


Fig. 4 Elements of the 230 nm radiometer.

stronger NO Gamma bands. Figure 5 presents the relative filter functions of the 230 nm and the older 260 nm radiometer. Comparison with the spectra of Figure 3 illustrates the molecular bands subtended by each of the filters.

Absolute calibration was achieved in the same manner described in Reference 1, in which an NBS-traceable, standard deuterium irradiance source is

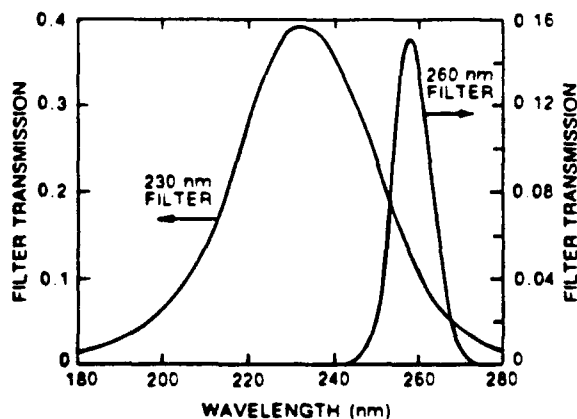


Fig. 5 Filter transmission functions.

deployed. System linearity is confirmed by inverse-square-distance measurements. The maximum possible error in the calibration is 15%, although self-consistency tests with the data and ancillary measurements indicate that a probable error near 10% is more appropriate.

#### The Kinetics Data Set

Directly behind the incident shock wave the translational temperature can attain values near 6000 K which immediately fall as the  $O_2$  dissociates. NO begins to form as soon as O atoms become available, and the excited NO (A) state becomes populated as it seeks to equilibrate with the decreasing temperature. To aid in elucidating these coupled phenomena, a set of shock tube conditions was selected which sought to separate and emphasize these effects. The shock tube is ideally suited to such studies, inasmuch as the capability for processing precisely controlled mixtures can be exploited. In this case, a number of  $N_2-O_2$  mixtures were used, with initial pressures of 5.0, 2.25 and 1.0 torr, and with shock velocities between 3 and 4 mm/ $\mu$ s. The largest excursion in the post-shock NO/ $O_2$  ratio was sought, to provide the broadest-range kinetic data set.

A set of such radiation profiles measured with the 230 nm radiometer is shown in Figure 6, for the test conditions cited thereon. The broad variation of the radiation profiles attests to the parametric changes among the various tests and to the usefulness of the data set for studies of excited state kinetic populations.

Also shown in the figures are the profiles that result when the calculated  $O_2$  Schumann-Runge contribution has been subtracted, as described later. Predicting these resultant NO Gamma band profiles is the challenge for any scheme that addresses the kinetics of the NO(A) state.

#### Test Time

The test time expected in the shock tube can be calculated from Mirels' laminar theory, which applies to all the results reported herein. For the time-histories shown in Figure 6, where the initial shock-tube pressure for all cases was 2.25 torr, the calculated test time decreases from 145  $\mu$ sec for a shock velocity of 3.24 mm/ $\mu$ sec to 105  $\mu$ sec at 3.86 mm/ $\mu$ sec. The observed test times, as determined from the termination of the radiation plateau in Figure 6, are somewhat greater than half this value, which is consistent with usual shock-tube experience. The sensitivity of the UV radiation is such that

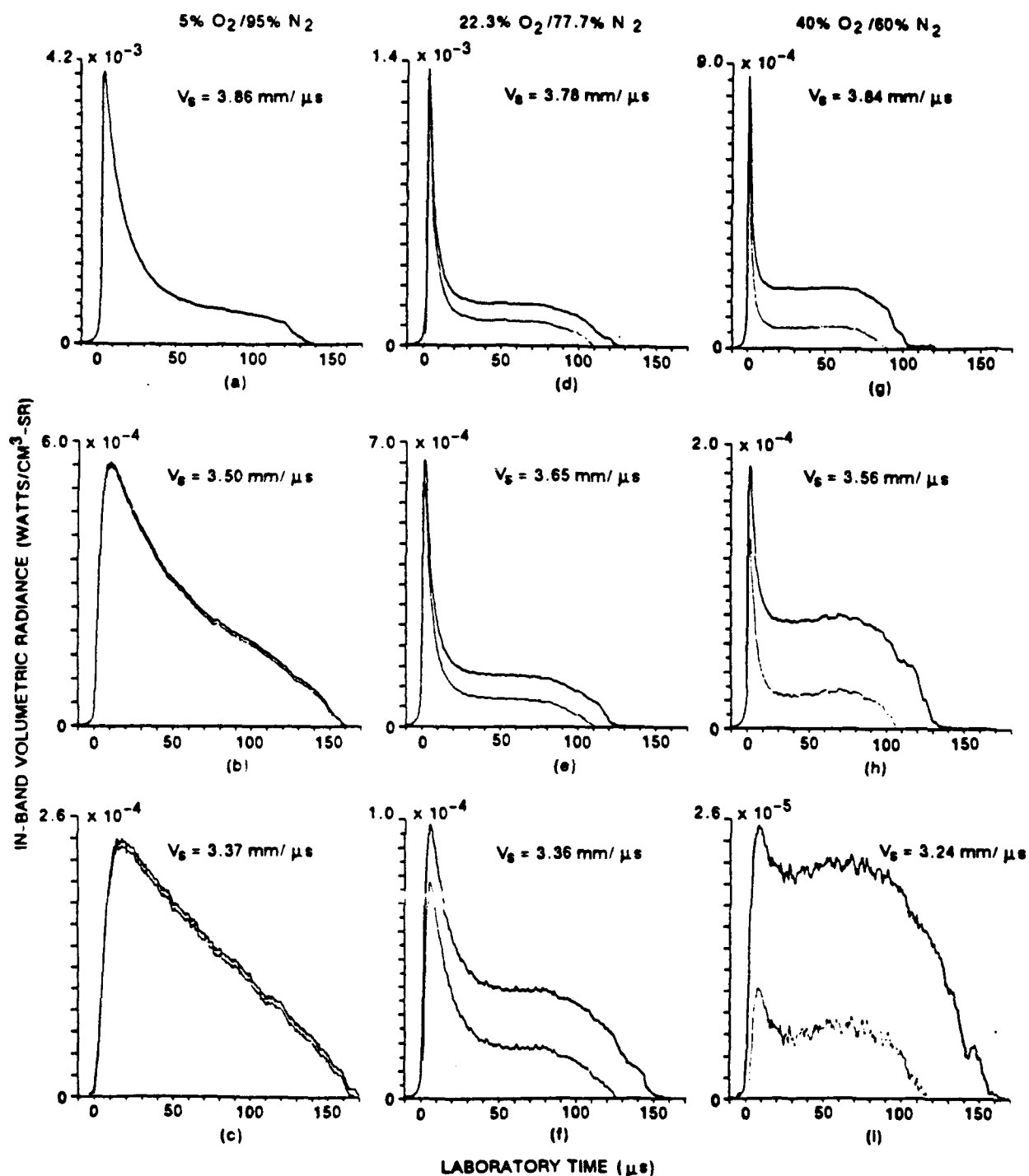


Fig. 6 Measured 230 nm radiation profiles for three  $O_2/N_2$  mixtures and various shock velocities. Initial shock tube pressure: 2.25 torr.

Upper curve: Observed radiance (NO +  $O_2$  S-R)

Lower curve: NO contribution obtained by subtracting calculated  $O_2$  S-R contribution

a drop in temperature of 100 K decreases the radiation by a factor of 2.

#### 4. Analysis of the Results

##### Equilibrium Ultraviolet Radiation

To calculate the contribution at wave number  $\omega$  of the equilibrium spectral radiation from a given  $(v', v'')$  band, a simple smoothed Q-branch structure was used<sup>2</sup>

$$I_{v'v''}(\omega) = 3.20 \times 10^{-30} |R_e|^2 q_{v'v''} n_u \frac{e^{-E_{v'}/kT}}{(Q_{v'})_u} \omega^4 C e^{-C|\omega-\omega_0|} \frac{\text{watts}}{\text{cm}^3 \text{ sr cm}^{-1}} \quad (1)$$

where

$$\begin{aligned} |R_e|^2 &= \text{squared transition moment (atomic units)} \\ q_{v'v''} &= \text{Franck-Condon factor} \\ n_u &= \text{number density in the excited electronic state (molecules/cm}^3\text{)} \\ E_{v'} &= \text{energy of vibrational state } v' \\ (Q_{v'})_u &= \text{vibrational partition function of upper electronic state} \\ C &= \frac{B_e''}{B_e' - B_e''} \cdot \frac{1}{kT} \quad (\text{cm}) \\ \omega_0 &= \text{bandhead wavenumber (cm}^{-1}\text{)} \end{aligned}$$

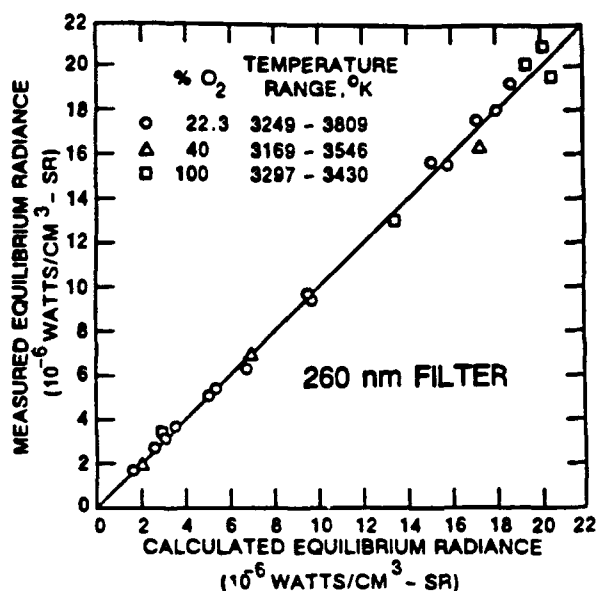
and  $B'$  and  $B''$  are the rotational spectroscopic constants for the upper and lower electronic states. The dependence of  $B$  on  $v$  was not included in the calculation.

The total spectral radiance  $I(\omega)$  was obtained by summing these expressions over all  $v', v''$ , yielding spectra for the NO gamma and  $O_2$  Schumann-Runge systems as shown in Reference 1. The radiation that should be measured by the calibrated detector was calculated as

$$S = \int_0^\infty [I_{NO\gamma}(\omega) + I_{O_2\text{ S-R}}(\omega)] F(\omega) D(\omega) d\omega \quad (2)$$

where  $F(\omega)$  is the filter transmission function and  $D(\omega)$  is the detector response function.

Among the many experimental radiance profiles obtained from shocks of varying velocity into pure oxygen and three mixtures of  $O_2$  and  $N_2$ , there were a number that attained equilibrium within the available test time. For each such case Figure 7 shows the equilibrium value of the experimental radiance integral  $S$  for the 260 nm filter, plotted against the calculated value. Squared transition mo-



$$O_2\text{ S-R: } |R_e|^2 = 1.4 \text{ a.u.} \quad NO\gamma: |R_e|^2 = 0.18 \text{ a.u.}$$

Fig. 7 Measured and calculated values of the 260 nm equilibrium radiance from three  $O_2/N_2$  mixtures.

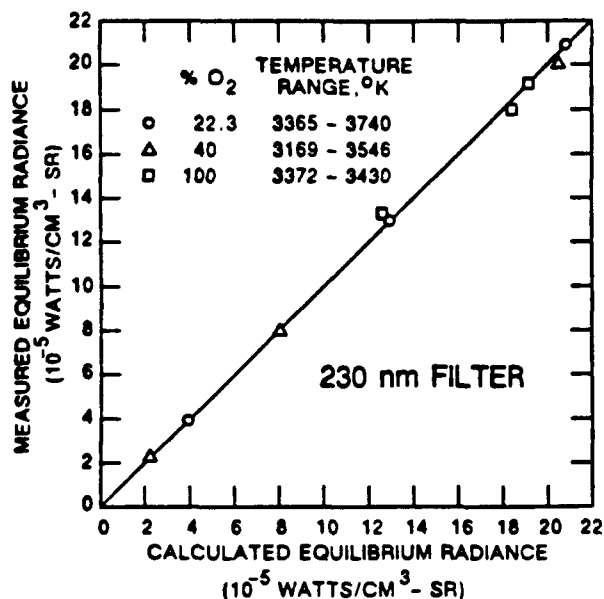
ments  $|R_e|^2$  were chosen for the NO Gamma and  $O_2$  S-R to supply the best agreement, and are shown in the figures. These values are about 35% higher than those reported in preliminary results<sup>1</sup>, and are consistent with accepted values for the two systems. The data include results for the four different  $O_2/N_2$  mixtures, and a range of shock speeds from 3.21 mm/ $\mu$ sec to 4.30 mm/ $\mu$ sec.

Figure 8 is a similar plot for the 230 nm filter data (available only for the more recent experiments). For this filter, the use of a slightly different set of  $|R_e|^2$  values (as shown in the figure) appeared to improve the fit.

The estimated precision in the shock-velocity measurements is  $\pm 0.2\%$ , which corresponds to a temperature accuracy of about  $\pm 0.2\%$ . This can result in a variation in the calculated radiance of about  $\pm 5\%$ . The ability to read the experimental values of the radiance results in an uncertainty of about  $\pm 3\%$ . The probable error in the calibration constant is  $\pm 10\%$ .

##### Non-Equilibrium Ultraviolet Radiation

A time-dependent record of the 230 nm and 260 nm radiation behind the shock wave was obtained for four  $N_2/O_2$  mixtures ( $\% O_2 = 100, 40, 22.3, 5$ ) and for a range of velocities from 3.24 to 3.86 mm/ $\mu$ sec. The temporal resolution of the records is estimated to be between 0.5 to 1.0  $\mu$ sec.



$$O_2 S-R: |R_0|^2 = 1.5 \text{ a.u.} \quad NO \gamma: |R_0|^2 = 0.21 \text{ a.u.}$$

Fig. 8 Measured and calculated values of the 230 nm equilibrium radiance from three O<sub>2</sub>/N<sub>2</sub> mixtures.

To analyze the nonequilibrium radiation, it is necessary to separate the amounts arising from the O<sub>2</sub> S-R and the NO Gamma. The time-dependent experimental values of S for the pure oxygen experiments do not show a radiation overshoot (Figure 2), but rise quickly to steady-state value. This feature was observed in work at Avco<sup>3</sup> in the late 1950's, and attributed to the rapid predissociation of the oxygen excited B state. Thus the B state remains in local thermodynamic equilibrium with the oxygen atom population, so that the number of O<sub>2</sub> molecules/cm<sup>3</sup> in the B state is given by

$$n_{O_2(B)} = \left( \frac{1}{K} \right) \left( \frac{n_{O_2(B)}}{n_{O_2}} \right)_{LTE} n_O^2 = \frac{n_O^2}{K} \left\{ 1.765 e^{-71,019/T} \left( \frac{1-e^{-2239/T}}{1-e^{-990/T}} \right) \left( 1.465 - 1.4 \times 10^{-4} T \right) \right\} \quad (3)$$

where K is the equilibrium constant for the reaction and the last factor in the equation is an approximate representation (appropriate over the range 3000 to 7000 K) of the required correction<sup>4</sup> to the rigid-rotator simple-harmonic-oscillator model. The O<sub>2</sub> radiation is taken to be proportional to  $n_{O_2(B)}$ , as determined from the equilibrium measurements.

We have assumed that the O<sub>2</sub> S-R system follows the same behavior in the radiation from N<sub>2</sub>/O<sub>2</sub> mixtures, with the O<sub>2</sub>(B) state staying in local equilibrium with the oxygen atom concentration at the translational temperature. The oxygen atom concentration behind the shock was calculated from a normal-shock nonequilibrium code<sup>5,1</sup>, and this population was used to determine the B state participation in the observed radiation. This amount of radiation was subtracted from the total observed, and the remainder was attributed to the NO Gamma system.

In the results shown in Figure 6, the total radiation and the portion attributed to NO Gamma are shown. These graphs of the NO radiation provide a record of the population of the NO(A) state as a function of time.

The NO(A) state could be produced either directly or by transfer from the metastable N<sub>2</sub>(A) state. Several reports<sup>6,7</sup> have speculated on the possible candidate reactions for both NO(A) and N<sub>2</sub>(A) production. The reactions that are considered likely for direct production of the NO(A) state are the electron collisional excitation of NO(X) and the recombination of N and O into the NO(A) state. The electron density in the present experiments is very low, so that the first reaction cannot be considered as likely. The recombination reaction does not produce an overshoot, and so will not supply the observed profiles. Heavy-body collisional excitation, either of NO(A) directly or of N<sub>2</sub>(A) followed by transfer to NO(A), will give overshoots of the type that have been observed in these experiments. However, no definitive set of rates that will describe the experimental results shown in Figure 6 has yet been determined.

We have begun the design of an LIF technique to monitor the production of the metastable N<sub>2</sub>(A) state. Near-IR absorption into the N<sub>2</sub>(B) state with observation of subsequent First Positive band emission is planned. A direct comparison of the N<sub>2</sub>(A) and NO(A) state profiles will provide a significant, complementary aid in studying these complex excitation kinetics.

#### Equilibrium Infrared Radiation

The infrared radiation from the shock-heated gas was measured using a HgCdTe detector and a narrow-bandpass filter with constant transmission from 1749 cm<sup>-1</sup> to 1954 cm<sup>-1</sup>, allowing good response for the NO fundamental IR band, which is centered at 1850 cm<sup>-1</sup>. The sensitivity of the detector was assumed constant over this spectral range. The measured signals contained an appreciable amount of noise, but for many conditions a plateau



region was reached where a final signal value could be determined. An example is shown in Figure 9.

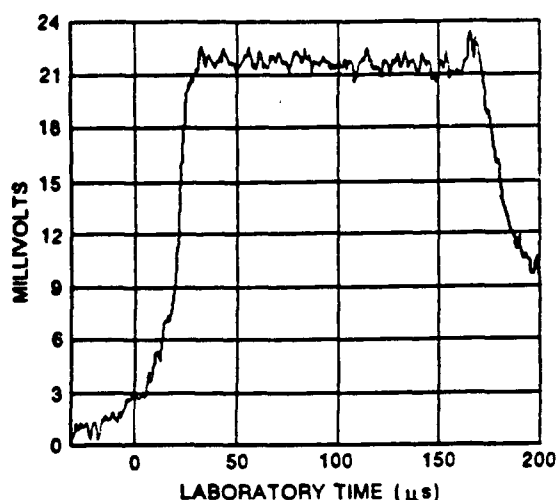


Fig. 9 Measured infrared radiation with equilibrium plateau.  
Initial shock tube pressure: 5.00 torr  
Shock velocity: 3.42 mm/μs.

The strength of the signal to be expected can be obtained by calculating the radiance of a single,  $v', J'; v'', J''$  transition, and summing these values over all the lines within the filter bandpass. The resulting signal strength is less dependent on temperature than is the total band radiance, because at higher temperatures a larger portion of the band is outside the range of the filter. This calculated signal strength can be written as:

$$S_{IR} = A \frac{n_{NO}}{n_L} \int \{ 790 + 0.25 (T-3000) - 2.5 \times 10^{-5} (T-3000)^2 \} \quad (4)$$

over the temperature range 3000 to 5000 K, where

$$\begin{aligned} \int &= \text{pathlength} = 7.62 \text{ cm} \\ n_L &= 2.689 \times 10^{19} \text{ molecules/cm}^3 \end{aligned}$$

and  $n_{NO}$  is the number density of NO molecules.  $A$  is a calibration constant for the system which was not determined. However, the consistency of the data can be shown by matching the calculated results to a single datum point and using this constant for the other points. The resulting plot for all experiments that clearly reached an equilibrium plateau is shown in Figure 10. The variations shown are consistent with the noise level of the infrared signal.

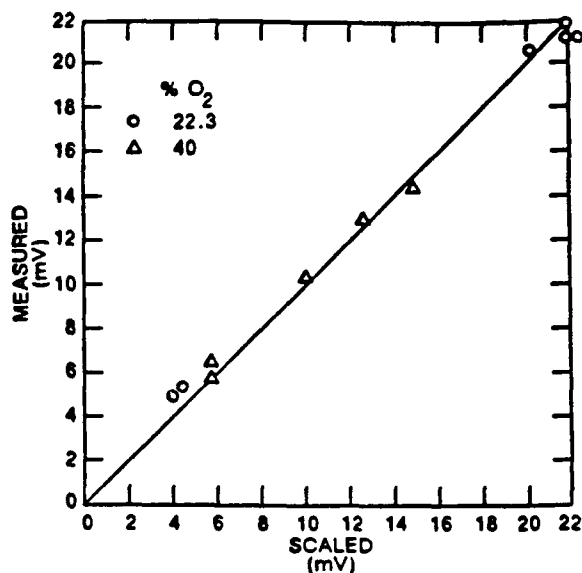


Fig. 10 Measured and calculated values of the equilibrium infrared radiation from two  $O_2/N_2$  mixtures.

#### Non-Equilibrium Infrared Radiation

Three examples of time-dependent infrared signals are shown in Figure 11. These examples are from the runs for which the 230 nm radiation is shown in Figure 6. The expected signal is shown by the smooth curves, which are calculated using equation (4) and values of  $n_{NO}$  and  $T$  determined by the normal-shock calculation<sup>6,1</sup>, scaled to the equilibrium value (Figure 10).

The lack of spatial resolution in the infrared measurements is demonstrated by the inability of the system to follow the calculated radiation overshoot, and by the sizable "foot" generated before arrival of the shock wave at  $t = 0$ . With this poor resolution it would also be expected that internal reflections in the shock tube might contribute to the resolution problem. However, further narrowing of the optical beam led to an unacceptable increase in signal noise.

To address this problem, a new infrared radiometer has been designed and installed in the shock tube. It utilizes an indium antimonide detector, which, despite the response roll-off at 5.5 μm, still provides a factor of 10 gain in overall SNR over that of the HgCdTe detector deployed previously. In addition, the spatial resolution has been enhanced by means of appropriate slits and  $CaF_2$  lenses. An extended range of IR measurements at higher SNR is anticipated for future tests.

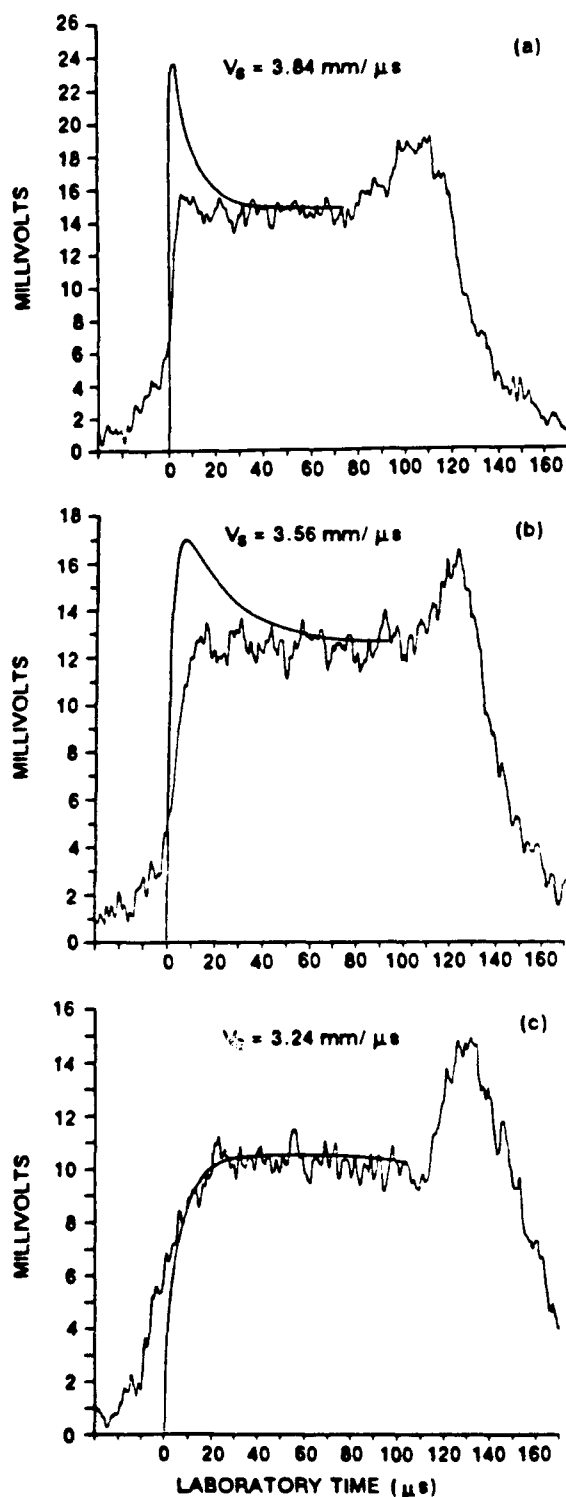


Fig. 11 Measured and calculated non-equilibrium infrared radiation profiles for three shock velocities in 40% O<sub>2</sub>/60% N<sub>2</sub> mixtures. Initial shock tube pressure: 2.25 torr. Test time ends at -70 μs. (See Fig. 6)

## 5. Summary

Calculated predictions of non-equilibrium ultraviolet radiation from the bow shock of hypersonic vehicles depends critically on relevant experimental data, which comprise the major goal of these studies. Earlier work led to the identification of the radiating species and to the velocity and altitude dependence of the UV radiances.

Further experimentation is reported that addresses the kinetics of the relevant electronic states. In particular, an extensive kinetic data set has been obtained, over which the NO and O<sub>2</sub> post-shock densities have been broadly varied. A computational model has been developed, involving the reactions and rates for excited state populations. Iterative comparative efforts are now underway to reconcile the calculated and measured nonequilibrium radiation profiles.

Equilibrated radiance levels for some cases permitted an evaluation of the NO Gamma and O<sub>2</sub> Schumann-Runge transition moments, from which their relative contributions to air radiation were determined. Similarly, equilibrium infrared measurements were used to establish that the NO fundamental band sequence provided a quantitative measure of the NO concentration. Additional and improved diagnostics are planned to record further observables for the study of these kinetic, radiative processes.

## 6. References

1. Wurster, W.H., Treanor, C.E., and Williams, M.J., *Nonequilibrium UV Radiation and Kinetics Behind Shock Waves in Air*. AIAA-89-1918, June 1989.
2. Treanor, C.E. and Williams, M.J., *A Method for Calculating Diatomic Spectra Using a Digital Computer*. CAL Report QM-1626-A-5, 1962.
3. Keck, J., Camm, J., and Kivel, B., *Absolute Emission Intensity of Schumann-Runge Radiation from Shock-Heated Oxygen*. J. Chem Phys. 28, 723 (1958). Kivel, B., *Radiation from Incident and Reflected Shocks in Air*. AMP 39, Avco Research Laboratory, January 1960.
4. Gilmore, F.R., *Basic Energy Levels and Equilibrium Data for Atmospheric Atoms and Molecules*. Rand Corporation Memo RM 5201-ARPA, March 1967.
5. Marrone, P.V. et al., *Inviscid, Nonequilibrium Flow Behind Bow and Normal Shock Waves*. CAL Report No. QM-1626-A-12 (I-III), May 1963, October 1963.

6. Smith, G.P., Crosley, D.R., Eckstrom, D.J., *Mechanisms and Rate Constants for the Chemistry of Radiating, Shock-Heated Air*. SRI International Report MP89-037, February 1989.
7. Brown, R.C., Annen, K.D., and Kolb, C.E., *Analysis of UV Nosecap Radiation*. Aerodyne Research, Inc., Report ARI-RR-771, May 1989.

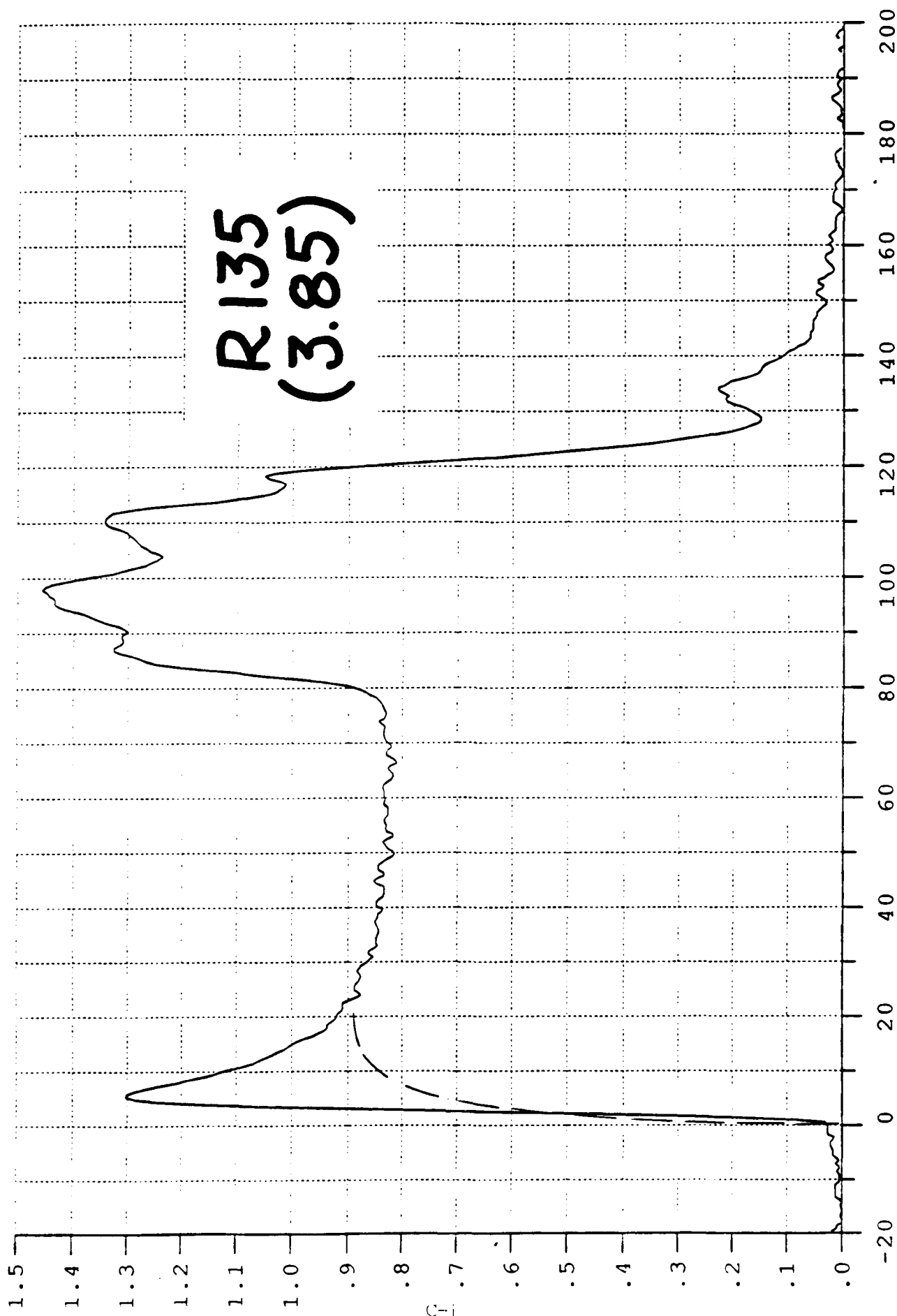
## 7. Acknowledgments

The authors would like to thank Dr. Michael Dunn for detailed discussions of shock-tube test times. Also acknowledged are Messrs. R. Hiemenz, J. Ambrusko and J. Johnson for their assistance in conducting the experiments.

## **APPENDIX C**

### **Full-Scale Records of Data in Figure 7**

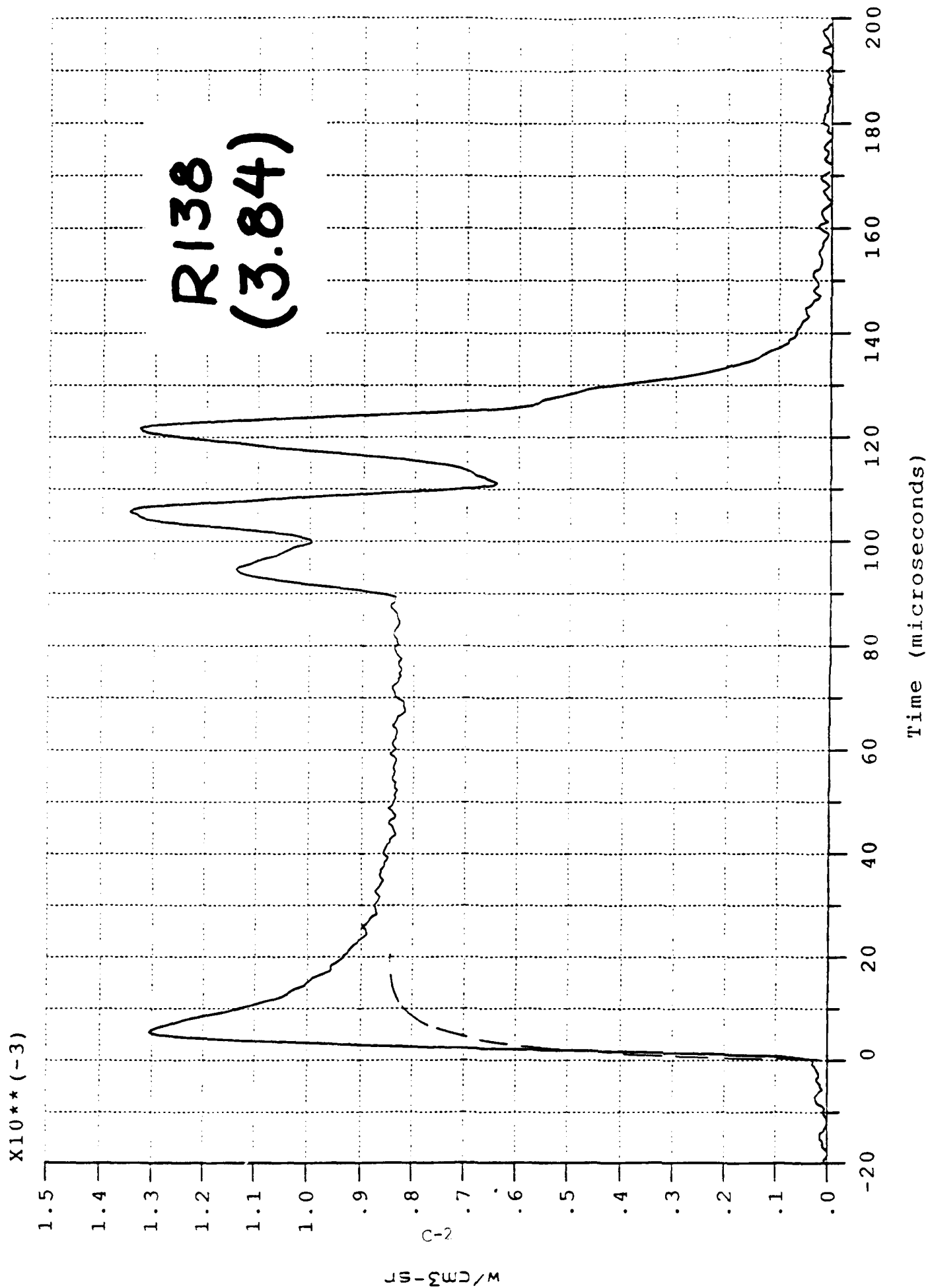
X10\*\*(-3)



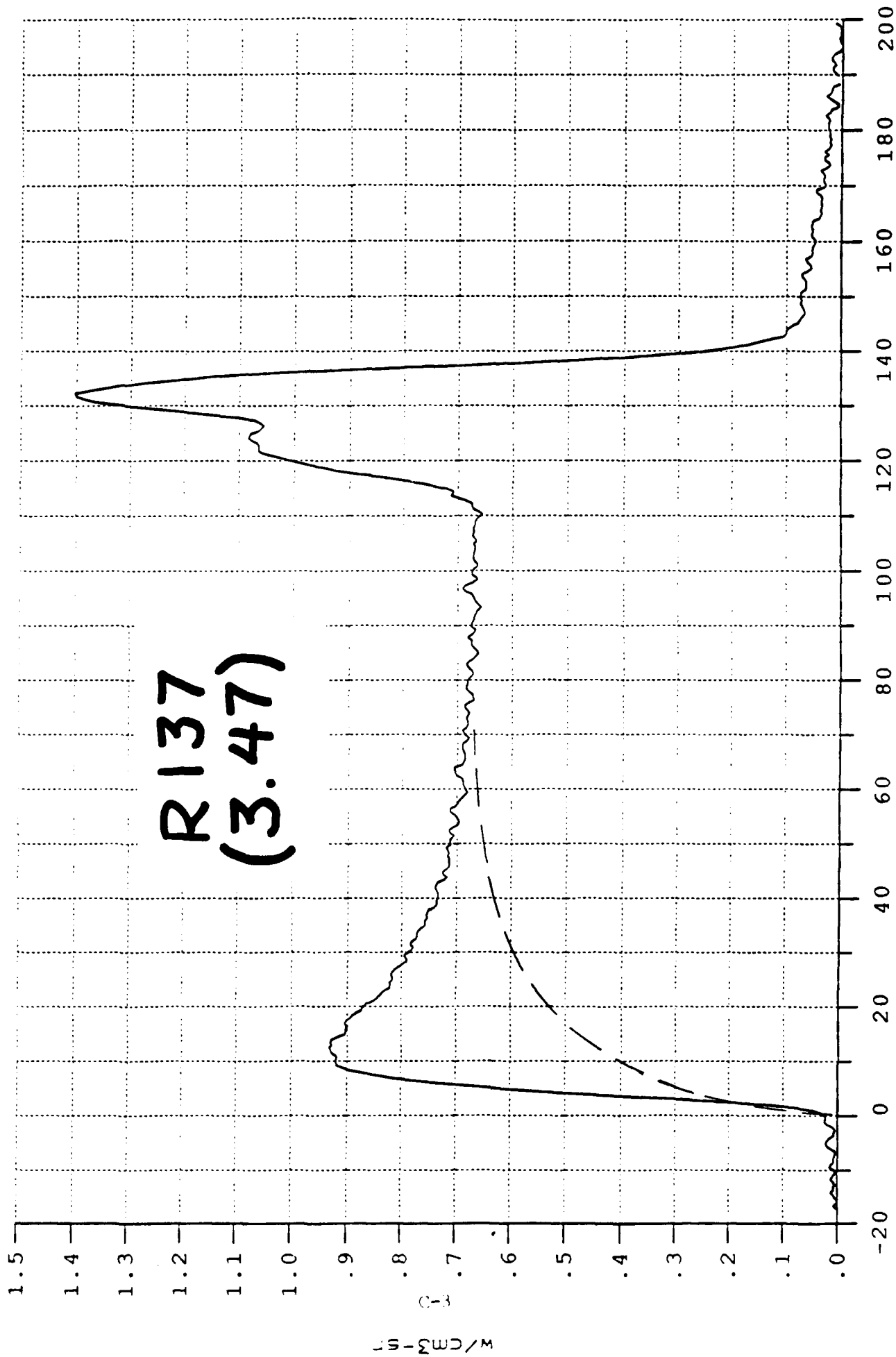
R135  
(3.85)

Time (microseconds)

IS-520/M

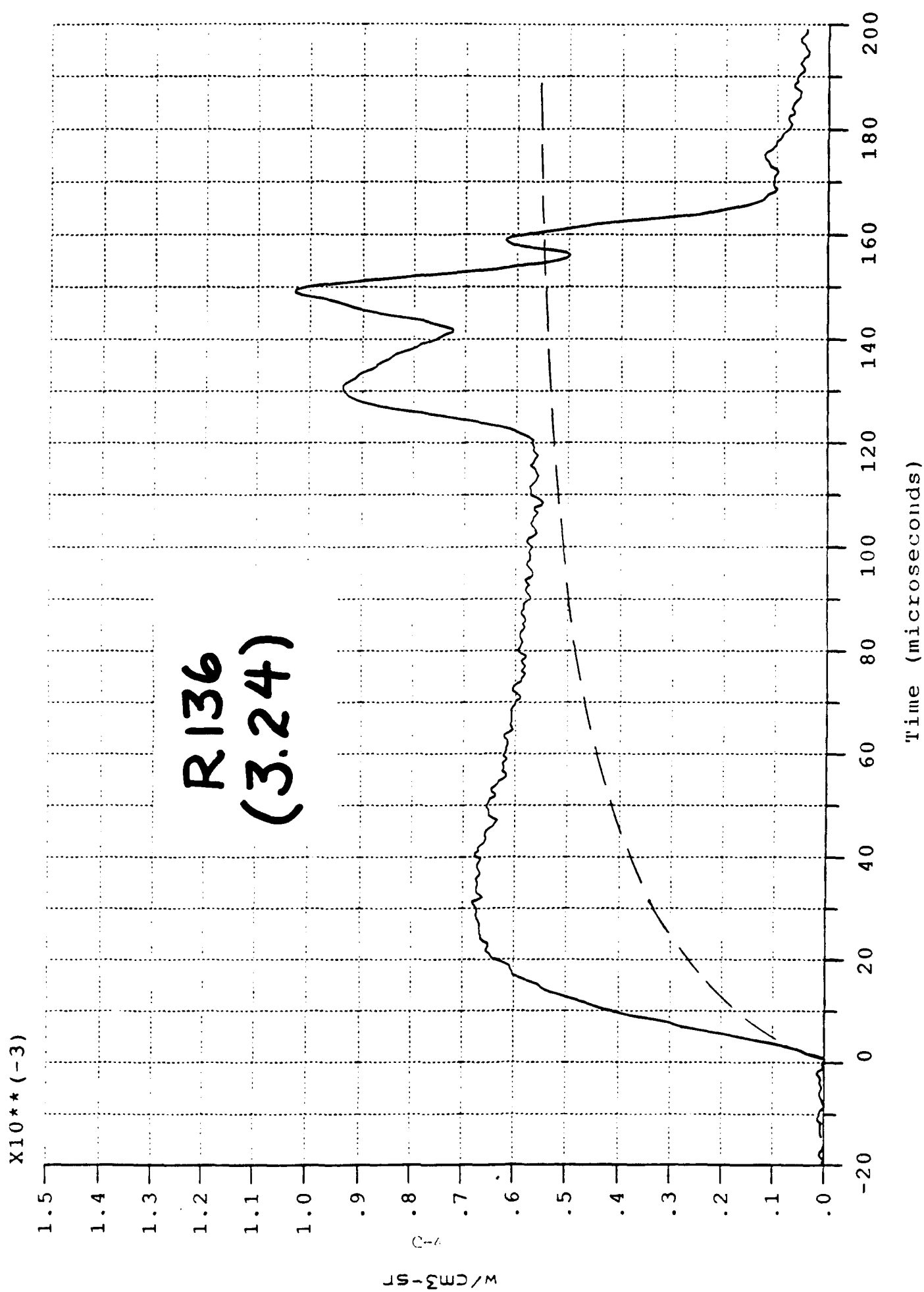


X10\*\*(-3)



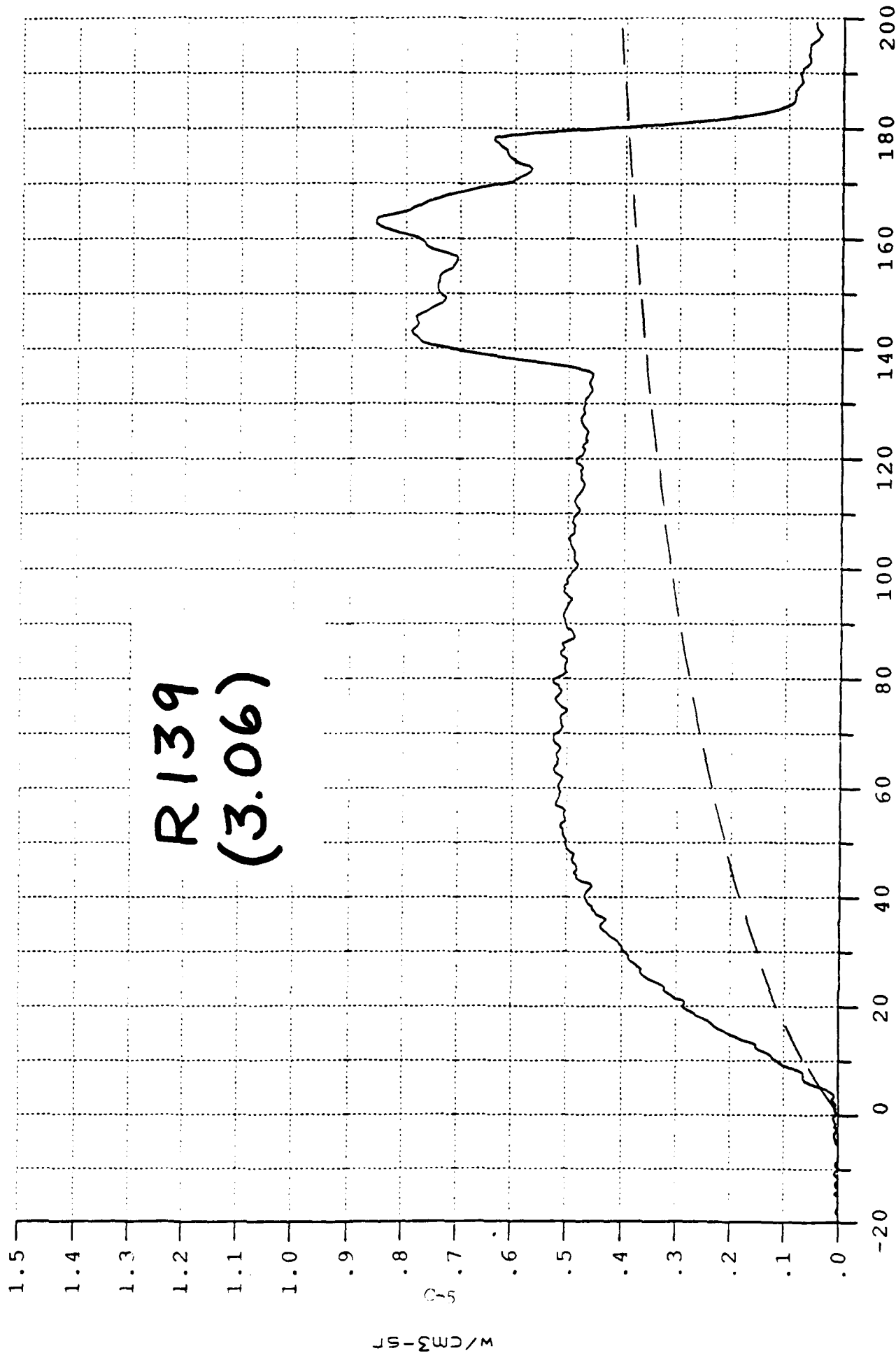
R137  
(3.47)

Time (microseconds)

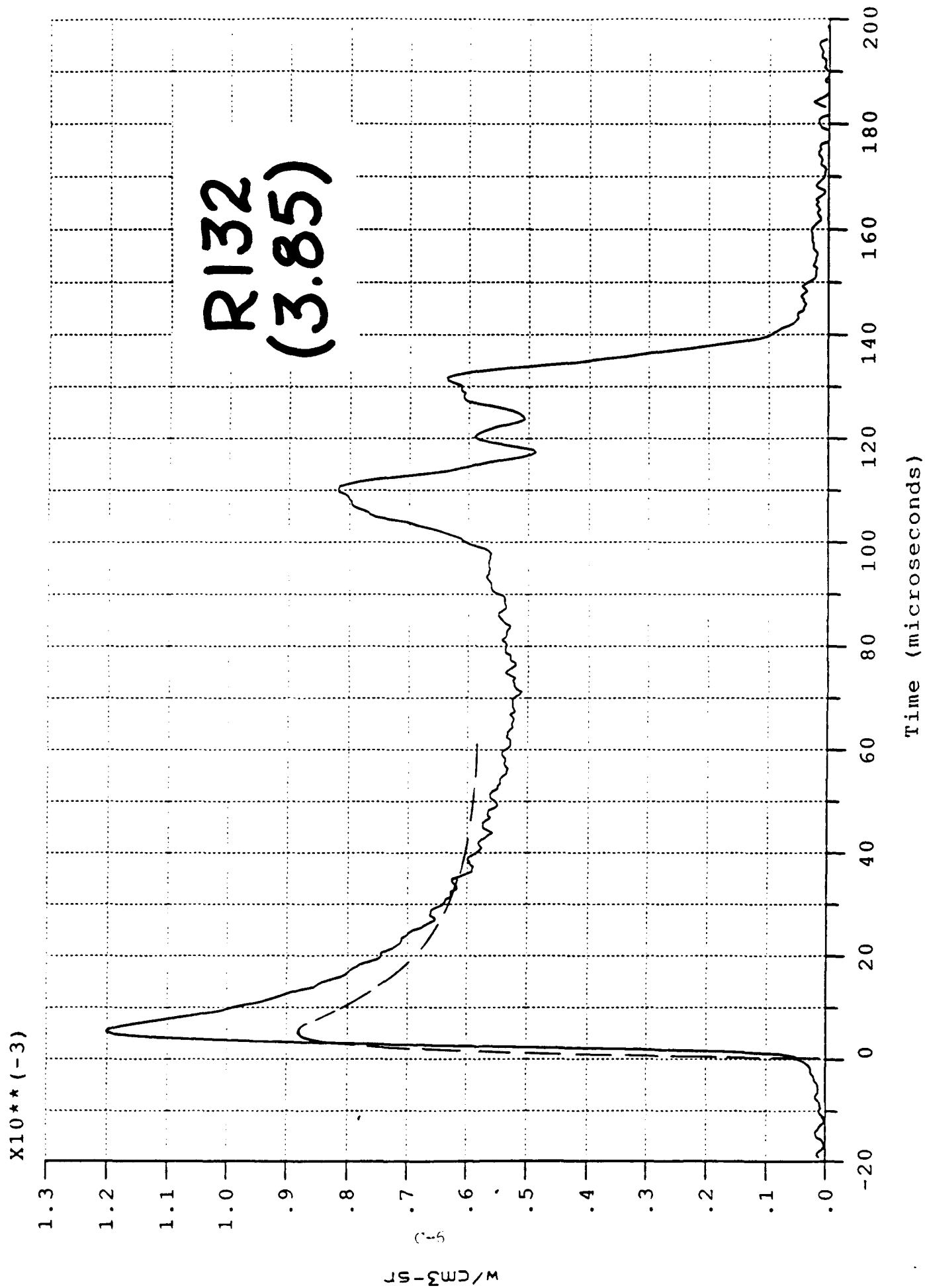




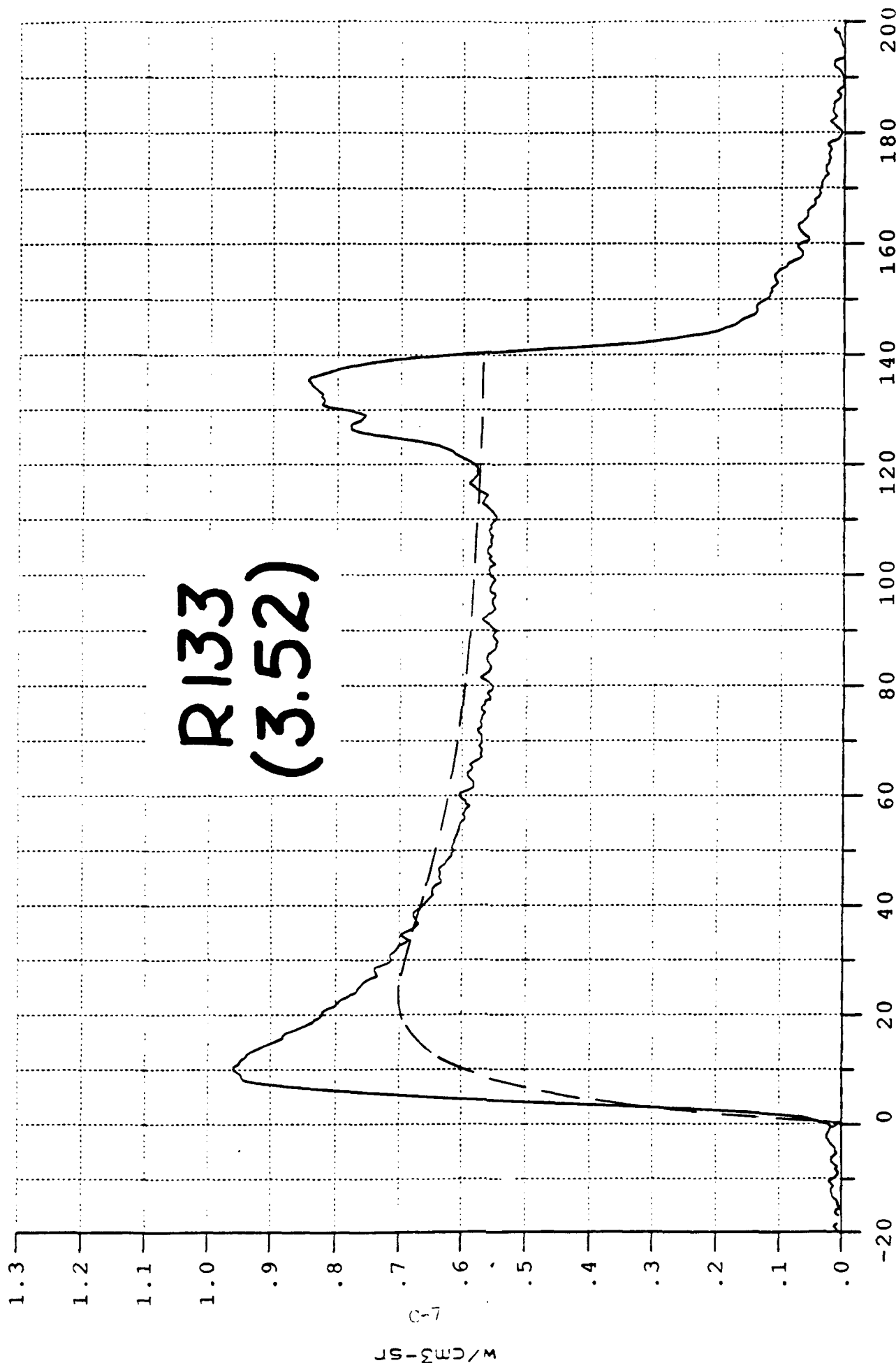
X10\*\*(-3)



R139  
(3.06)

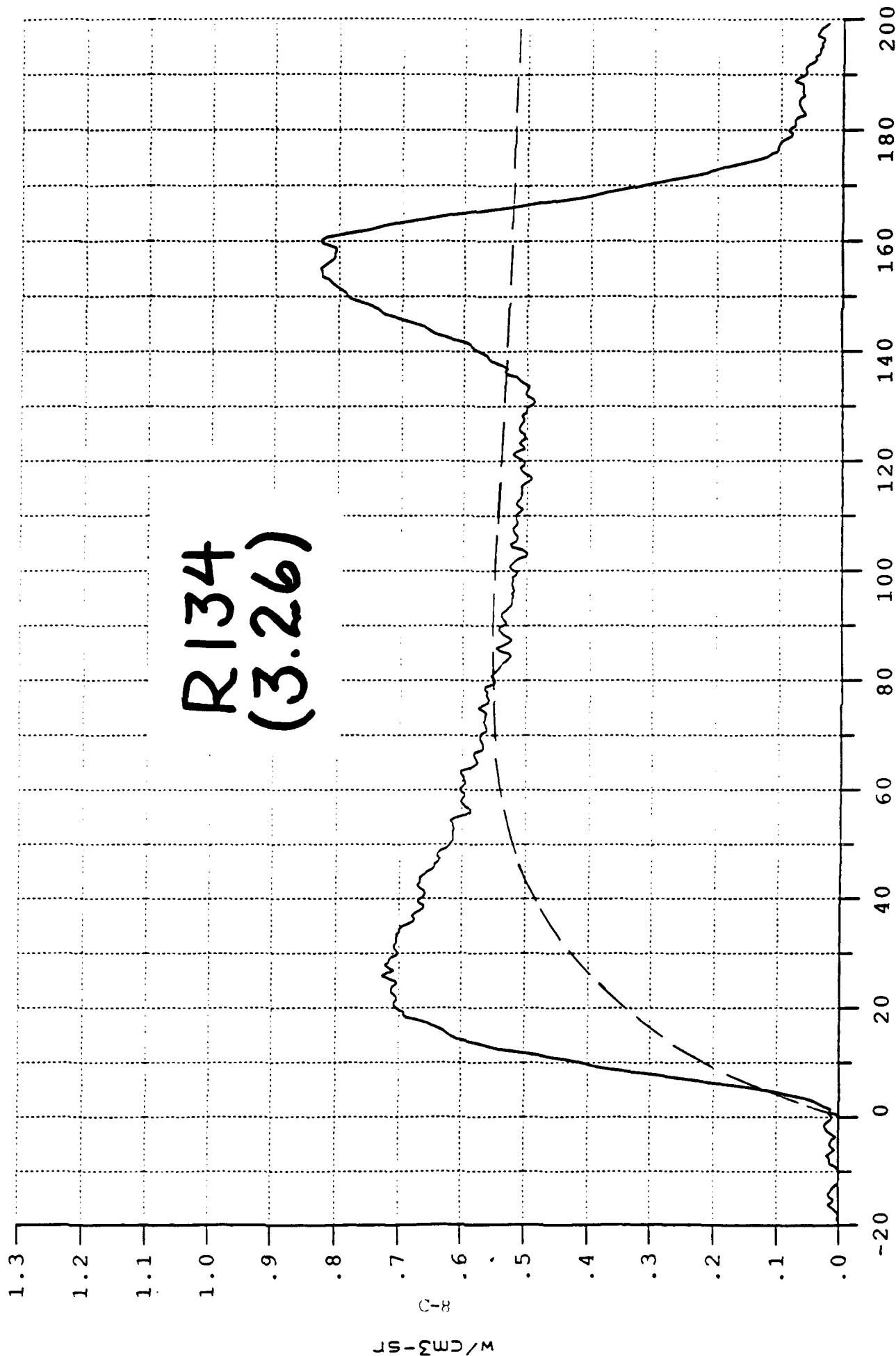


X10\*\*(-3)



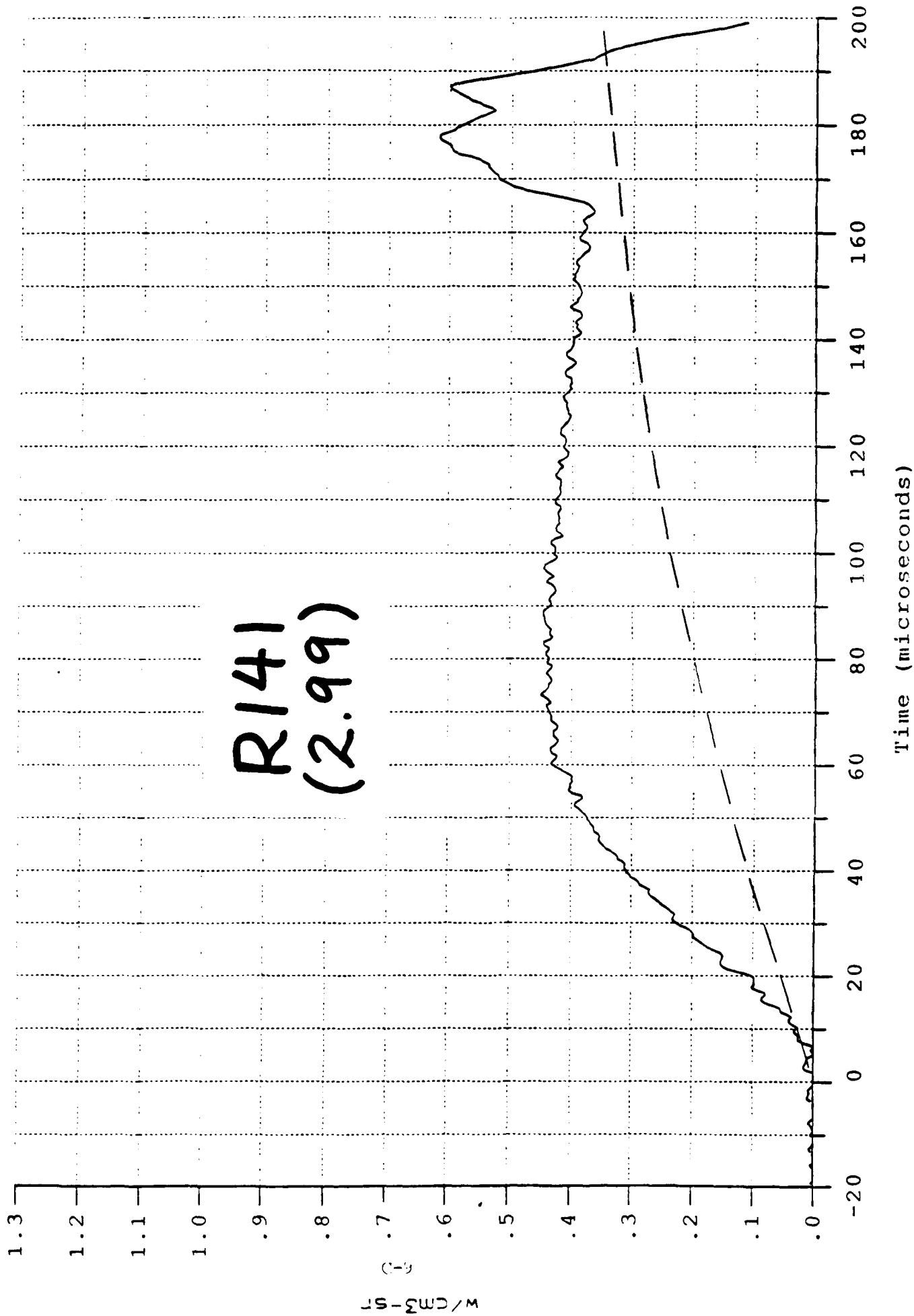
Time (microseconds)

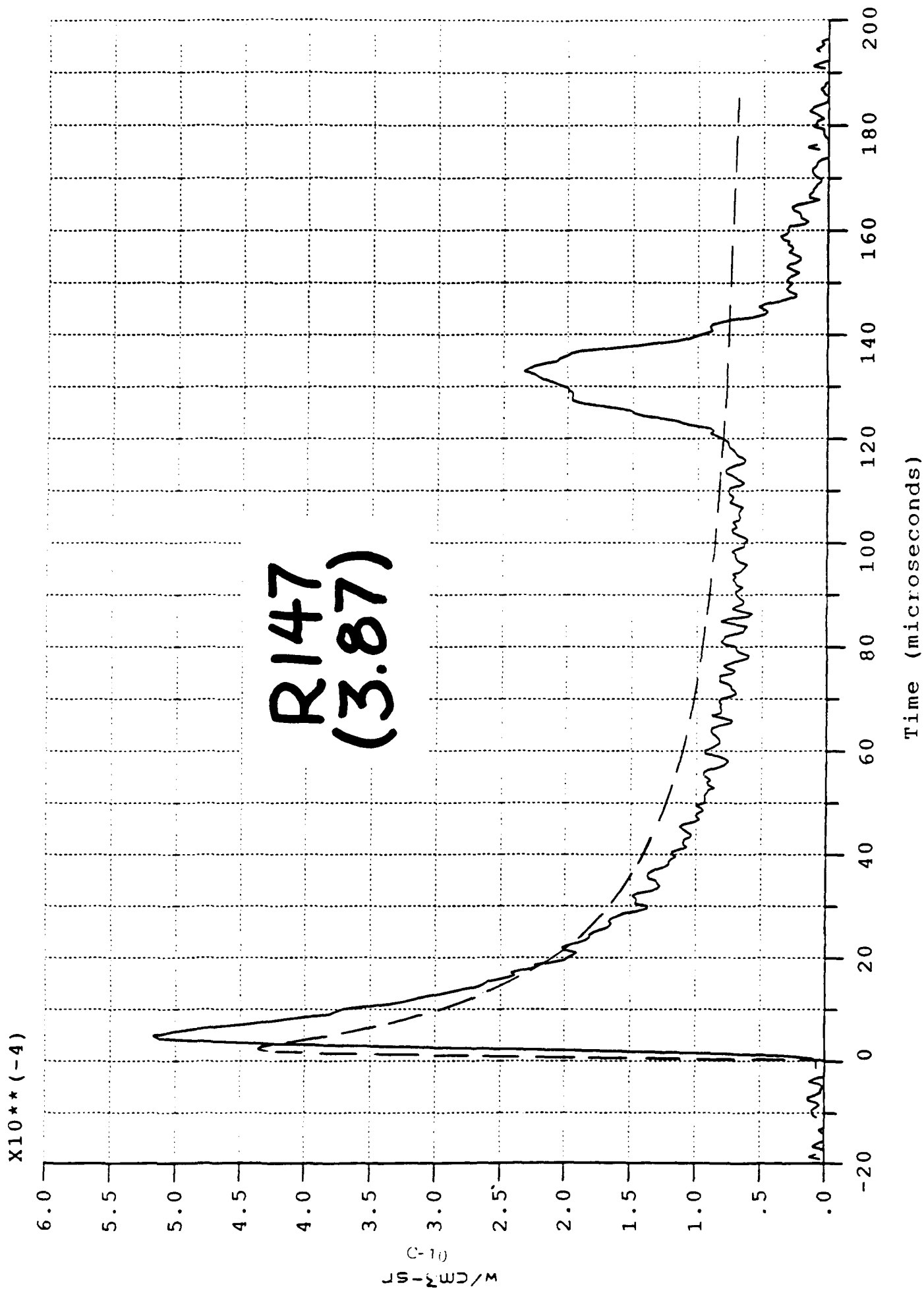
X10\*\*(-3)



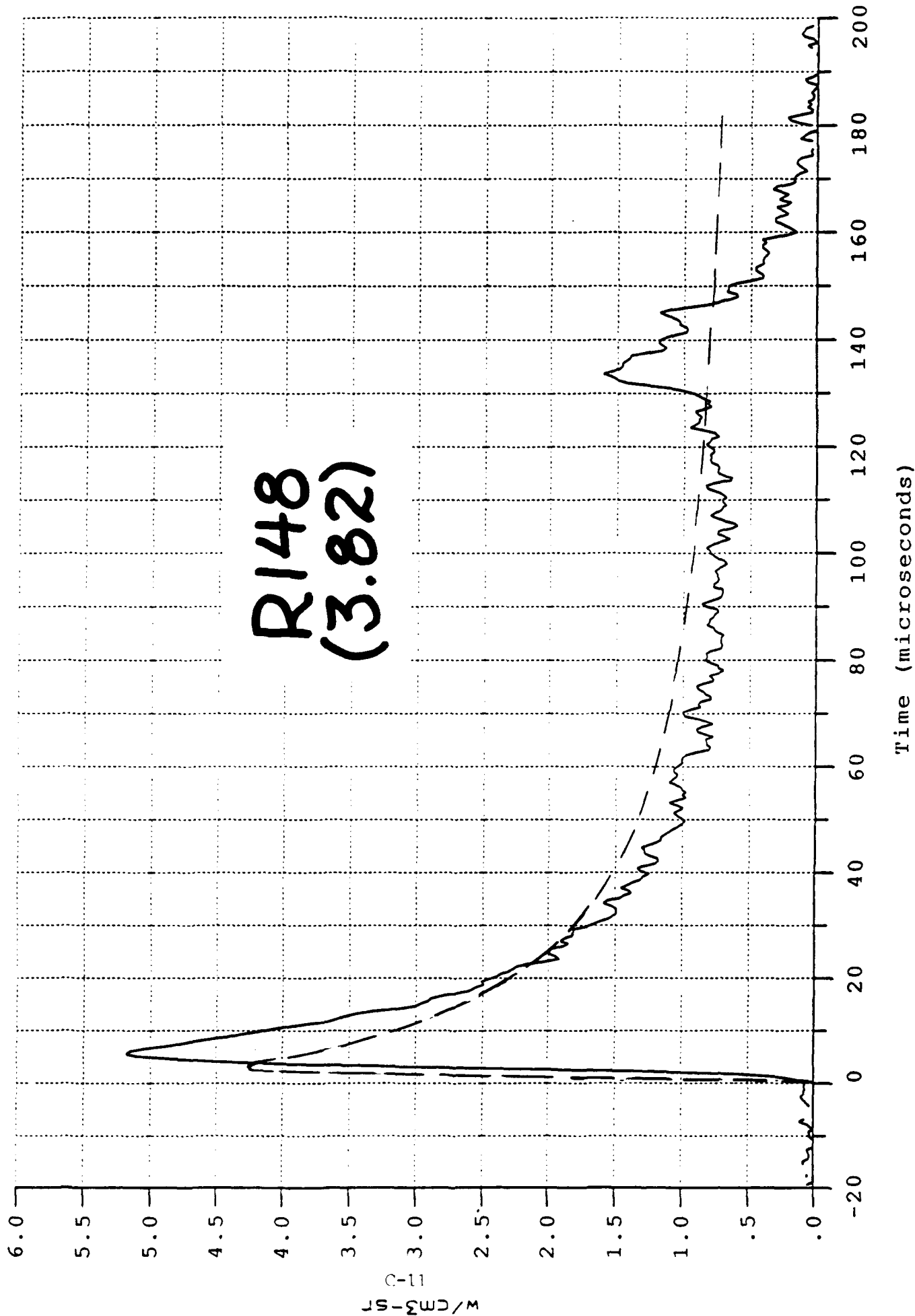
R134  
(3.26)

X10\*\*(-3)

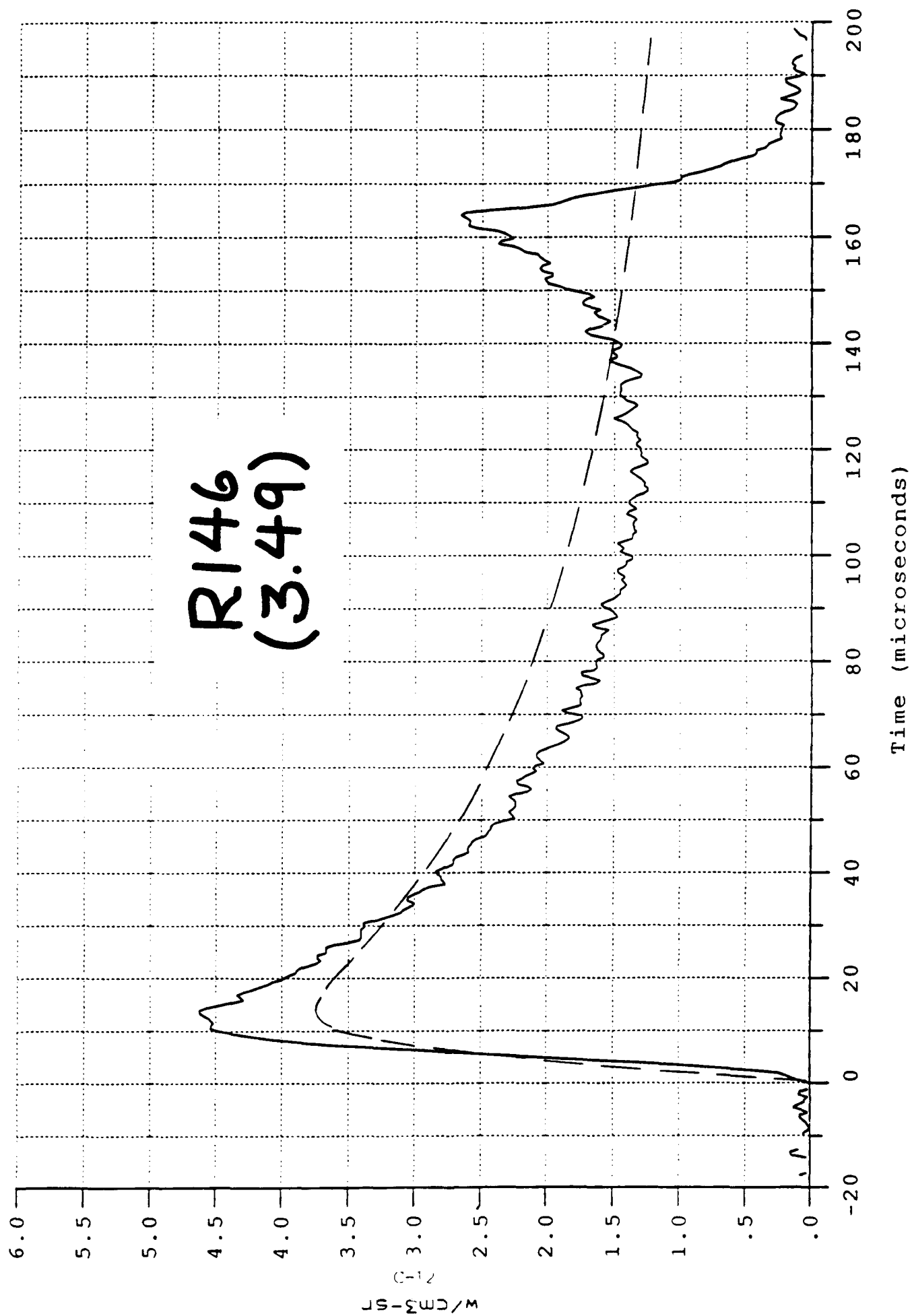




P1 = 2.25  
X10\*\*(-4)

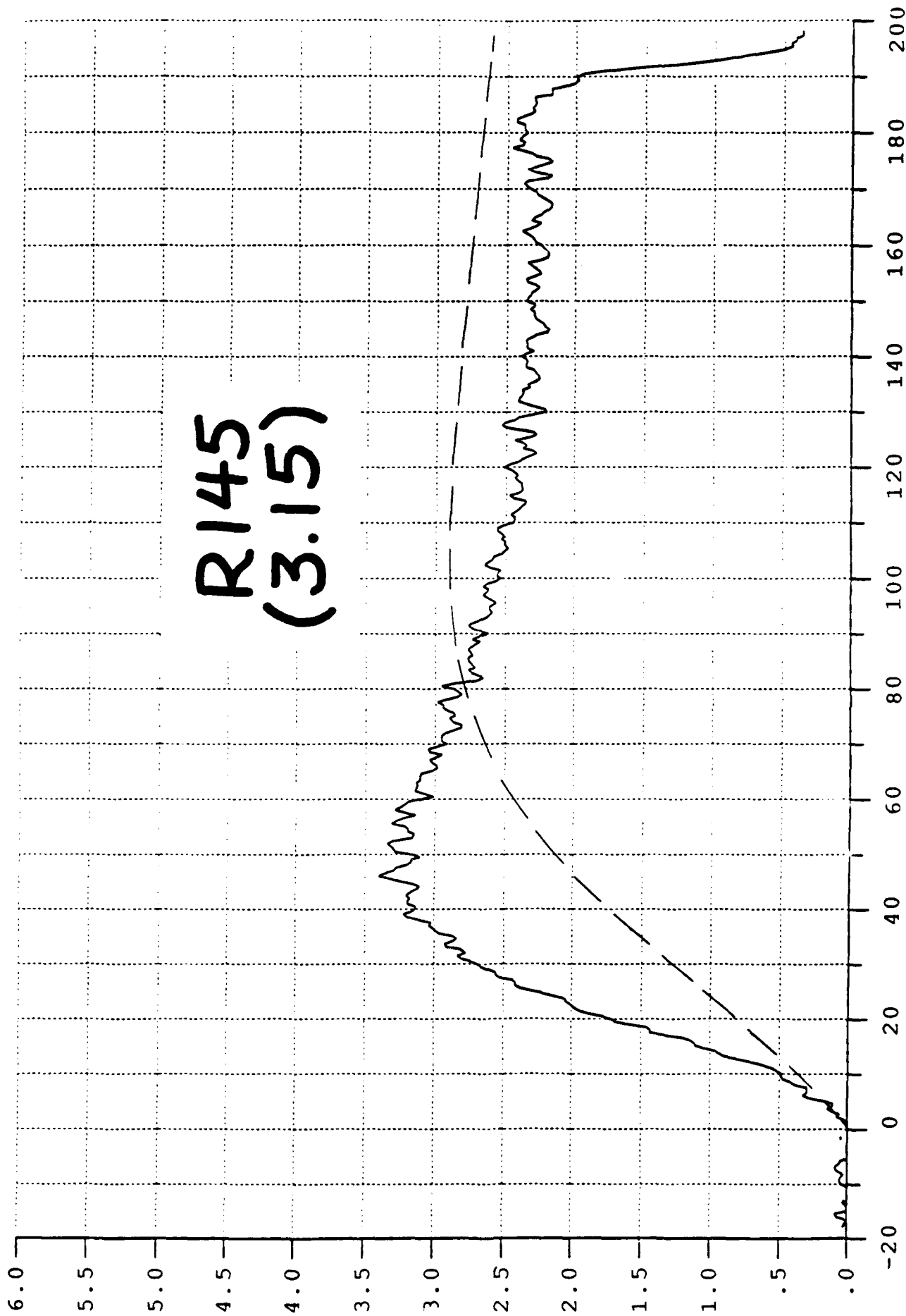


RUN 146  
P1 = 2.25 torr  
X10\*\*(-4)





X10\*\*(-4)

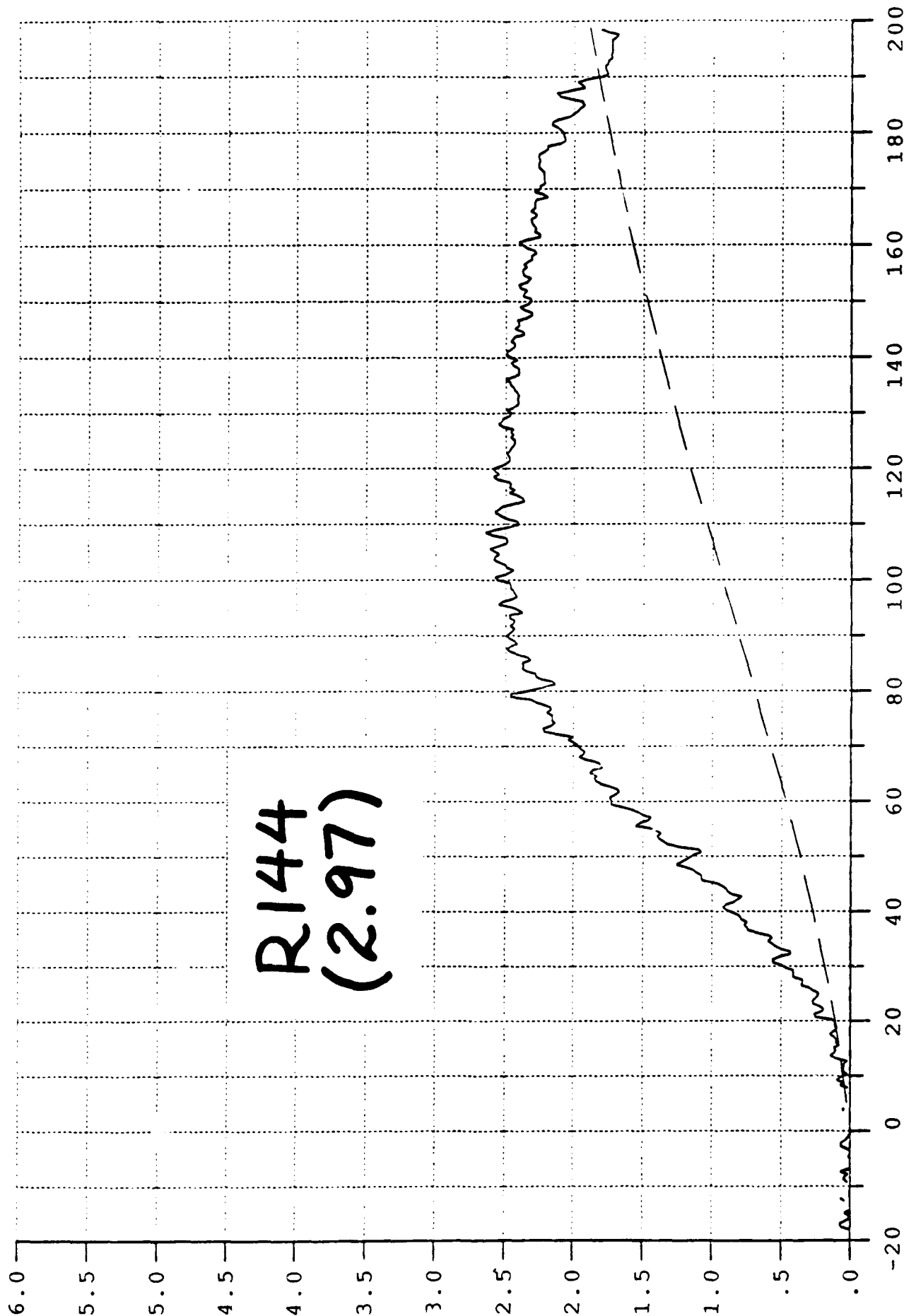


Time (microseconds)

R145  
(3.15)

JS-CM3-SF  
C-13

X10\*\*(-4)



R144  
(2.97)

W/CM3-SI  
(14)

Time (microseconds)

## APPENDIX D

### IR SPECTRAL ANALYSIS

This appendix presents a summary of the equations that were used in the analysis on the equilibrium IR radiation from nitric oxide, and applies them to the results obtained in the current experiments. The equations are discussed in detail in References 7 and 13.

The wave numbers of the rotational-vibrational lines in the P, Q, and R branches are given by

$$D-1) \quad \nu_P = \nu_{v'} - 2(J'+1)B_e - \alpha_e [(J'+1)^2 - 2(J'+1)v' - 1] \quad J=1,2,3, \dots$$

$$D-2) \quad \nu_Q = \nu_{v'} - \alpha_e (J'^2 + J' - 1) \quad J=1,2,3, \dots$$

$$D-3) \quad \nu_R = \nu_{v'} + 2J'B_e - \alpha_e (J'^2 + 2J'v' - 1) \quad J=2,3,4, \dots$$

for a transition from the  $v'J'$  state. The wavenumber  $\nu_{v'}$  is given by

$$D-4) \quad \nu_{v'} = \omega_e - 2v'\omega_e x_e + 3.25 v'^2 \omega_e y_e = [1904.03 - (27.9)v' - (0.0039)v'^2] \text{ cm}^{-1}$$

The constants for the NO molecule are:

$$B_e = 1.7046 \text{ cm}^{-1} \quad \text{and} \quad \alpha_e = 0.0178 \text{ cm}^{-1}$$

The intensities of the lines are given by

$$D-5) \quad I_P = \nu_P^4 \left( \frac{J'^2 + 2J'}{J'+1} \right) \frac{C_{em} V'}{Q_v Q_R} e^{-\frac{[J'^2 + J' - 1][B_e - \alpha_e(v' + \frac{1}{2})]}{kT}} \cdot e^{-\frac{G_{v'}}{kT}}$$

$$D-6) \quad I_Q = \nu_Q^4 \left( \frac{2J'+1}{J'(J'+1)} \right) \frac{C_{em} V'}{Q_v Q_R} e^{-\frac{[J'^2 + J' - 1][B_e - \alpha_e(v' + \frac{1}{2})]}{kT}} \cdot e^{-\frac{G_{v'}}{kT}}$$

$$D-7) \quad I_R = \nu_R^4 \left( \frac{J'^2 - 1}{J'} \right) \frac{C_{em} V'}{Q_v Q_R} e^{-\frac{[J'^2 + J' - 1][B_e - \alpha_e(v' + \frac{1}{2})]}{kT}} \cdot e^{-\frac{G_{v'}}{kT}}$$

WATT/MOLECULE-SR

$$\text{WHERE } G_v = V[\omega_e - (v+1)\omega_e x_e + (v^2 + 1.5v + 0.75)\omega_e y_e] \text{ cm}^{-1}$$

and  $k=0.695 \text{ cm}^{-1}\text{K}^{-1}$ .  $C_{em}$  is the emission constant for the NO band system and a value of  $C_{em}=2.97\pm0.54 \times 10^{-33} \text{ watts cm}^4/\text{molecule} \cdot \text{sr}$  was reported in References 7 and 13.

The partition functions are approximated as

$$\text{D-8) } Q_R = \frac{kT}{B e^{-\alpha} e^{(\nu + 1/2)}}$$

and

$$\text{D-9) } Q_V = \left( 1 - e^{-\frac{\nu_1}{kT}} \right)$$

The total in-band radiation measured is then calculated as

$$\text{D-10) } R = n_{NO} \ell \sum_{\nu, \nu'} [I_P F_{\nu P} + I_Q F_{\nu Q} + I_R F_{\nu R}] \text{ watts/cm}^2 \cdot \text{sr}$$

where  $F_\nu$  is the combined filter-detector response at wavenumber  $\nu$ , as described in Section 3.2,  $n_{NO}$  is the number density of NO molecules ( $\text{molecules/cm}^3$ ) and  $\ell$  is the diameter of the shock tube, 7.62 cm. The values of  $F_\nu$  were taken as constants over specified wavenumber intervals, as given in Table D-1.

Wavenumber Interval ( $\text{cm}^{-1}$ )			Average Response $F_\nu$
1724.1	-----	1773.0	0.00445
1773.0	-----	1793.7	0.0311
1793.7	-----	1816.5	0.11565
1816.5	-----	1839.9	0.2975
1839.9	-----	1863.9	0.515
1863.9	-----	1888.6	0.7105
1888.6	-----	1913.9	0.8175
1913.9	-----	1938.0	0.851
1938.0	-----	1964.6	0.8815
1964.6	-----	1992.0	0.7615
1992.0	-----	2020.2	0.395
2020.2	-----	2049.2	0.0864
2049.2	-----	2079.0	0.0089

TABLE D-1. FILTER-DETECTOR RESPONSE

The values of  $F_V$  are relative numbers, and are the same values used in the calibration of the system. As shown in Figure 4, this calibration yields the relation

$$D-11) S = 1.04 \times 10^{-4} V \quad W/CM^2 \cdot SR$$

where  $S$  is the in-band radiation,  $\int I_{BB} F_V dV$ , and  $V$  is the number of millivolts measured by the detector.

The values obtained for the calculation indicated in Eqn. D-10 are shown in Table D-2, calculated for three temperatures covering the range of interest in the present experiments.

$T (^{\circ}K)$	$R/n_{NO} \ell C_{em}$
3000	$3.507 \times 10^{12}$
4000	$4.755 \times 10^{12}$
5000	$5.758 \times 10^{12}$

TABLE D-2. CALCULATED RADIATION INTEGRALS

These values of  $R/n_{NO} \ell C_{em}$  can be expressed as

$$D-12) \frac{S}{n_{NO} \ell C_{em}} = f(T) = 3.507 \times 10^{12} [1 + 3.21 \times 10^{-4} (T - 3000)]$$

Turning now to the experimental results for the infrared measurements with NO, the value of  $S$  for each experiment is obtained from the number of millivolts measured at equilibrium, by using Equation D-11. Using  $\ell = 7.62$  cm, the value of  $S/\ell [1 + 3.21 \times 10^{-4}(T - 3000)]$  is plotted in Figure D-1 vs.  $n_{NO}$ . According to Equation D-12 this should yield a straight line with slope equal to  $3.506 \times 10^{12} C_{em}$ . From Figure D-1 a value of  $C_{em}$  is obtained as

$$C_{em} = 3.66 \times 10^{-33} \text{ watts cm}^4/\text{molecule} \cdot \text{sr}$$

slightly higher than the value quoted in References 7 and 13.

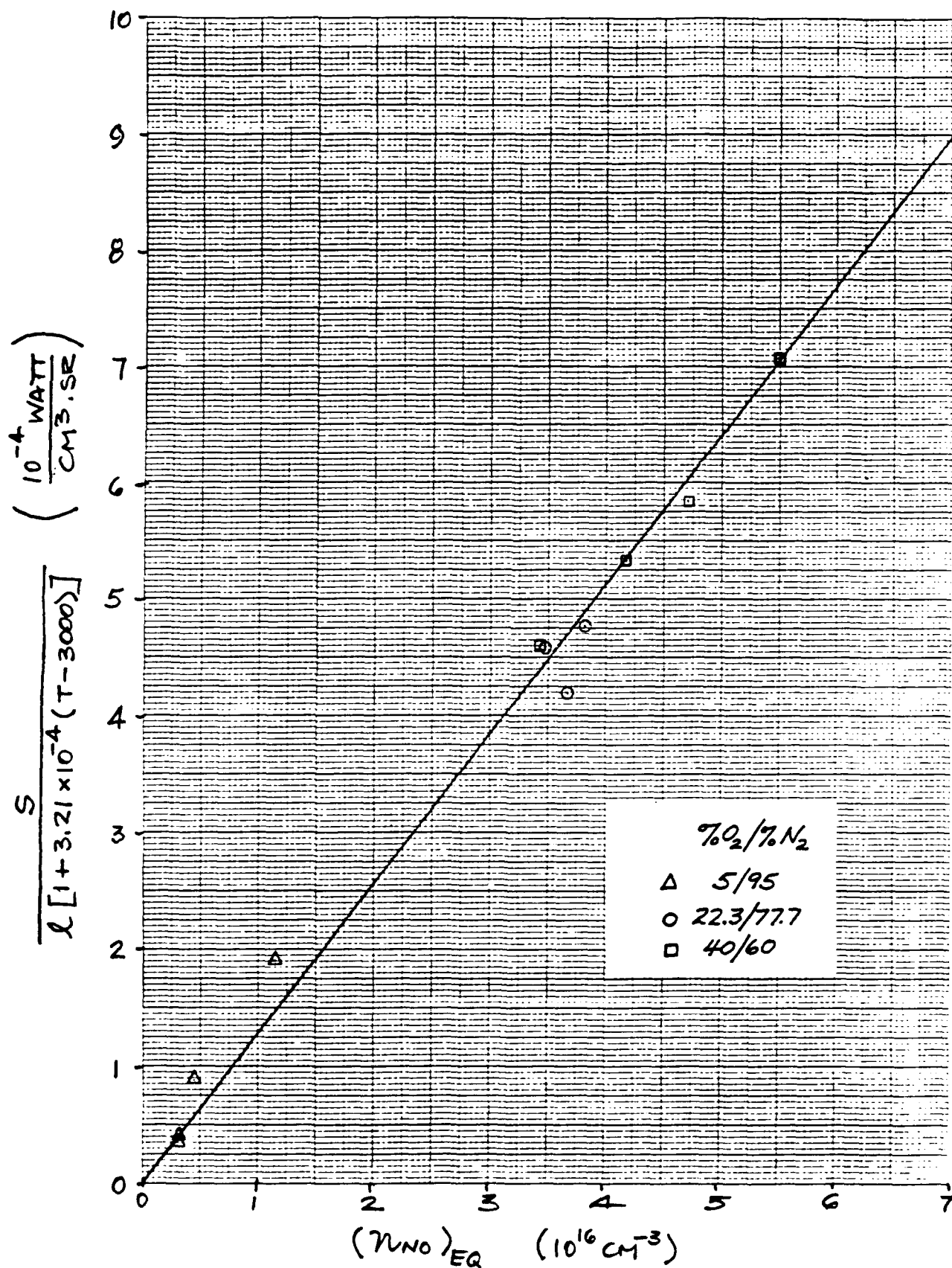


FIGURE D-1. EQUILIBRIUM INFRARED RADIATION INTENSITY DIVIDED BY TEMPERATURE SCALING FACTOR

## **APPENDIX E**

### **Full-Scale Records of Data in Figure 14**

